CHAPTER 1

INTRODUCTION

Hyperon polarization physics studies the formation of spin-polarized hyperons from a spin-unpolarized target and proton beam. The dependence of the magnitude of the polarization of produced hyperons on the kinematic parameters of the reaction provides information on the nature of processes that predominate in the hyperon production. The experimental data on the dependence of the hyperon polarization on the transverse momentum P_t and the ratio of the hyperon momentum to the incident proton momentum X_f can be used as an effective test for existing theoretical models describing production of hyperons in inclusive nucleon-nucleon collisions. The existing experimental data for Σ^+ and $\overline{\Sigma}^-$ hyperons [1, 2] covers P_t range $1.02 - 1.57$ GeV/c and X_f range of $0.445 - 0.491$. There is no data for higher values of P_t and X_f. On the other hand, recently developed theoretical models, some of which will be described below, make certain predictions about the behavior of the hyperon production polarization at higher P_t and X_f values. Since almost all new models adequately explain the behavior of the data at low P_t values, it is very important to measure the polarization of Σ^+ and other hyperons at higher P_t in order to test the validity of those new theories. Another aspect of the hyperon polarization physics is the dependence of the magnitude of the polarization on the atomic number of the material used as a primary target in the hyperon production. The effect of the target material was first observed for Λ^0 hyperons produced on different targets [3, 4]. In that study the Λ^0 polarization measured using combined lead/copper data was found to be about 2/3 of the polarization magnitude corresponding to the beryllium data. At the present time there is no satisfactory theoretical explanation

for this effect.

Measuring hyperon polarization at high values of P_t and X_f requires a high energy proton beam that can only be produced by few accelerators in the world. With its 800 GeV/c high intensity proton beam, the Fermi National Accelerator Laboratory's Tevatron is an ideal facility for the hyperon physics experiments. The hyperon polarization measurement described in this thesis was performed using the SELEX (E781) spectrometer operating at Fermilab's Proton Center experimental area.[1] The primary goal of the SELEX experiment was to accumulate a large sample of decays of charmed particles produced by a high energy and high intensity secondary hyperon beam on a secondary (charm) target.[2] To achieve its goals, the SELEX employs state of the art experimental techniques including a high speed data acquisition system (DAQ), online "software" filtering of accumulated data, and high-resolution silicon detectors. To produce the high intensity charged hyperon beam the SELEX experiment uses a hyperon production channel and a beam steering system capable of directing 800 GeV/c protons at positive and negative targeting angles of up to 4 mrad at the production target. The system is capable of producing positively charged hyperons of up to 572 GeV/c. This corresponds to P_t values of up to nearly 2.3 GeV/c. The existing data [1, 2] does not cover this P_t range. For this reason, the SELEX apparatus also has a unique potential to study charged hyperon production polarization especially at large $P_t \approx 1.5 - 2.3$ GeV/c values.

The SELEX experiment started its data taking in September of 1996 and continued it until September of 1997. The main mode of operation of the SELEX spectrometer (for charm studies) was with a negative secondary hyperon beam and

[1] The list of the members of the SELEX collaboration is shown in Figure 1.

[2] For more information on the SELEX experiment see the SELEX web page at <http://fn781a.fnal.gov>.

zero primary proton beam targeting angle. Σ^+ hyperon polarization measurement, on the other hand, requires a positive secondary beam and a set of measurements at two complementary non-zero targeting angles. Switching between these two operating modes required considerable retuning. The data on which the measurement described in this thesis is based was taken in a series of short runs (less then 8 hours long) in May and July of 1997. The data analysis continued until February of 1999. At the data analysis stage, the polarization of the hyperons was measured by studying parity non-conserving decays of the polarized hyperons in two high-resolution spectrometers of the SELEX apparatus (the Beam Spectrometer of the SELEX apparatus, here called Hyperon Spectrometer, was used to reconstruct the track of the Σ^+ hyperon, and the M2 Spectrometer, here called Baryon Spectrometer, was used to reconstruct the track of the Σ^+ charged decay product). The data analysis resulted in the world's first measurement of the polarization of Σ^+ hyperons at $P_t > 1.8$ GeV/c. In addition to this result, the first study of the dependence of Σ^+ polarization on the production target material was conducted.

The presentation of the material in this thesis is organized as follows. Chapter 2 provides a very brief introduction into the hyperon polarization theory and gives review of some recent literature on the subject. Chapter 3 describes how the measurement of the hyperon polarization can be done experimentally. Chapter 4 describes the experimental apparatus used in the present measurement. Chapter 5 provides insight into the data analysis algorithm. Chapter 6 considers important questions relating to the value of the systematic error in the measured polarization. Chapter 7 shows how the primary beam targeting angles were verified. And, finally, Chapter 8 describes the physics implications of the results of the present measurement.

G. P. Thomas
Ball State University, Muncie, IN 47306, U.S.A.

E. Gülmez
Bogazici University, Bebek 80815 Istanbul, Turkey

R. Edelstein, E. Gottschalk[1], S. Y. Jun, A. Kushnirenko, D. Mao[2], P. Mathew[3], M. Mattson, M. Procario, J. Russ, J. You
Carnegie-Mellon University, Pittsburgh, PA 15213, U.S.A.

A. M. F. Endler
Centro Brasiliero de Pesquisas Físicas, Rio de Janeiro, Brazil

P. S. Cooper, J. Engelfried[4], J. Kilmer, S. Kwan, J. Lach, G. Oleynik[5], E. Ramberg, D. Skow, L. Stutte
Fermilab, Batavia, IL 60510, U.S.A.

Y. M. Goncharenko, O. A. Grachov[6], V. P. Kubarovsky, A. I. Kulyavtsev[7], V. F. Kurshetsov, A. A. Kozhevnikov, L. G. Landsberg, V. V. Molchanov, V. A. Mukhin, S. B. Nurushev, A. N. Vasiliev, D. V. Vavilov, V. A. Victorov
Institute for High Energy Physics, Protvino, Russia

Li Yunshan, Li Zhigang, Mao Chensheng, Zhao Wenheng, He Kangling, Zheng Shuchen, Mao Zhenlin
Institute of High Energy Physics, Beijing, P.R. China

M. Y. Balatz, G. V. Davidenko, A. G. Dolgolenko, G. B. Dzyubenko, A. V. Evdokimov, A. D. Kamenskii, M. A. Kubantsev, I. Larin, V. Matveev, A. P. Nilov, V. A. Prutskoi, V. K. Semyatchkin, A. I. Sitnikov, V. S. Verebryusov, V. E. Vishnyakov
Institute of Theoretical and Experimental Physics, Moscow, Russia

U. Dersch, I. Eschrich[8], K. Königsmann[9], I. Konorov[10], H. Krüger, S. Masciocchi[11], B. Povh, J. Simon, K. Vorwalter[12]
Max-Planck-Institut für Kernphysik, 69117 Heidelberg, Germany

I. S. Filimonov, E. M. Leikin, A. V. Nemitkin, V. I. Rud
Moscow State University, Moscow, Russia

V. A. Andreev, A. G. Atamantchouk, N. F. Bondar, V. L. Golovtsov, V. T. Kim, L. M. Kochenda, A. G. Krivshich, N. P. Kuropatkin, V. P. Maleev, P. V. Neoustroev, S. Patrichev, B. V. Razmyslovich, V. Stepanov, M. Svoiski, N. K. Terentyev[13], L. N. Uvarov, A. A. Vorobyov
Petersburg Nuclear Physics Institute, St. Petersburg, Russia

S. Gerzon, I. Giller, M. A. Moinester, A. Ocherashvili, V. Steiner
Tel Aviv University, 69978 Ramat Aviv, Israel

A. Morelos
Universidad Autonoma de San Luis Potosí, San Luis Potosí, Mexico

M. Luksys
Universidade Federal da Paraíba, Paraíba, Brazil

S. L. McKenna, V. J. Smith[14]
University of Bristol, Bristol BS8 1TL, United Kingdom

C. Kenney, S. Parker
University of Hawaii, Honolulu, HI 96822, U.S.A.

N. Akchurin, M. Aykac, M. Kaya, D. Magarrel, E. McCliment, K. Nelson, C. Newsom, Y. Onel, E. Ozel, S. Ozkorucuklu, P. Pogodin
University of Iowa, Iowa City, IA 52242, U.S.A.

L. J. Dauwe
University of Michigan-Flint, Flint, MI 48502, U.S.A.

T. Ferbel, C. Ginther, C. Hammer, P. Slattery, M. Zielinski
University of Rochester, Rochester, NY 14627, U.S.A.

M. Gaspero, M. Iori
University of Rome "La Sapienza" and INFN, Rome, Italy

L. Emediato, C. Escobar[15], F. Garcia, P. Gouffon, T. Lungov[16], M. Srivastava, R. Zukanovich Funchal
University of São Paulo, São Paulo, Brazil

A. Bravar, D. Dreossi, A. Lamberto, A. Penzo, G. F. Rapazzo, P. Schiavon
University of Trieste and INFN, Trieste, Italy

Figure 1: Members of the Fermilab SELEX (E781) collaboration.

CHAPTER II

THEORETICAL REVIEW

The Standard Model

According to the Standard Model (also called Glashow-Weinberg-Salam Theory of Unified Electroweak Interaction), the world is made of six quarks grouped into three generations: u(up), d(down), c(charm), s(strange), t(top), b(bottom); six leptons e(electron), ν_e(electron neutrino), μ(muon), ν_μ(muon neutrino), τ(tau), ν_e(tau neutrino), and corresponding antiparticles. The properties of these particles are shown in Table 1.

The interactions are carried by gauge bosons. There are three types of interactions: gravitational, electroweak and strong. The gravitational interaction is mediated by the graviton, it is extremely weak and will not be considered here. Electroweak interaction is mediated by the photon γ, $W^{\pm}$ and Z^0 bosons. The gluon g mediates the strong interaction between quarks and between gluons themselves. Quarks are not directly observable. Quark-antiquark combinations are called mesons, and three quark combinations are called baryons. The main characteristics of the interactions are presented in Table 2. Baryons can be grouped into an octet and a decouplet, see Table 3 and Table 4.

Baryons containing s-quark are called hyperons. The strong interaction is responsible for the hyperon production, while the weak interaction is responsible for hyperon decay. Since the parity is not conserved in weak decays, this permits measurement of the spin polarization of the hyperons (discussed later). The properties of mesons and baryons are presented in Table 5.

Production of Hyperons

Hyperons are produced in reaction $p+N \rightarrow H+X$, where p is a proton of the beam, N is a nucleon, H is a hyperon, and X represents all residual particles. It was observed that some hyperons produced on an unpolarized target by an unpolarized proton beam have a net nonzero spin polarization. The incoming beam proton and the proton of the target (it is assumed that the second interacting particle is also a proton) consist of uud quarks, the outgoing Σ^+ consists of uus-quarks. In order to produce a Σ^+ hyperon the beam proton must part with some of its quarks and pick up an s-quark. Several quantum processes may be responsible for production of the s-quark of the Σ^+, including, but not limited to quark-quark and quark-gluon scattering, quark pair annihilation and gluon fusion. These basic processes are shown in Figure 2.

The kinematic dependence of the magnitude of the hyperon polarization may shed light on the sub-processes that take place in hyperon production. Since, as will be described below, all of these sub-processes have different kinematic dependence of the polarization of the final quark, measuring actual polarization of hyperons may help to identify the dominant channel(s) of the hyperon production.

Theory of Hyperon Polarization

Although there exist some phenomenological models, the production of polarized hyperons from an unpolarized proton beam has not been adequately quantitatively described yet. Recently, considerable efforts have been made to derive formulas that predict contributions of numerous quark subprocesses to the hyperon polarization. Many questions remain unanswered, however. For example, there is still no theory which explains the dependence of the polarization on the atomic

number of the target material.

Background

Rotational symmetry with respect to the beam axis requires that the polarization must vanish as $P_t \to 0$. This was observed in numerous experiments. At high P_t the perturbative quantum chromodynamics predicts that the single quark polarization must also approach zero. In the massless quark approximation the helicity of the quark at each vertex is conserved, and as the consequence there can be no spin-flips. This phenomenological prediction must work whenever the transverse momentum is large compared to the mass of the quark [5].

It has been observed experimentally that the polarization slightly decreases with P_t, at P_t near 1 GeV/c; however it has not been observed that the polarization at the highest possible P_t approaches zero. Such behavior of the experimental data has caused suspicion that either QCD is not correct, or that the assumptions neglecting confinement for the purposes of perturbative calculations are inappropriate [5].

Since 1970's a number of models pursuing different treatment of the polarization phenomenon have been proposed to qualitatively and/or quantitatively describe the existing data. The Lund model [6] was based on the string mechanism of quark production. Other models were seeking to take into account the spin-orbital interaction in the constituent quark approximation [7].

Quark polarization resulting from various QCD subprocesses

An attempt to describe the polarization phenomena through gluon fusion of the s-quark ($g + g \to s + \bar{s}$) was first made by Dharmaratna et al. [5]. These authors

considered both lowest-order and fourth order processes that contribute to gluon-gluon fusion of an s-quark, and then used perturbative calculations to make certain predictions. In what follows I give a brief description of these quantum processes.

Gluon-gluon fusion

The two lowest order (no-loop) diagrams contributing to polarization through gluon fusion are shown on Figure 2(a). Figure 2(b) shows the fourth order processes that contribute to the hyperon polarization. The polarization of the quark resulting from the gluon fusion, is given by the following formula, see Ref. [5]:

$$P = a_s \frac{m(p^2 - k^2\cos^2\theta)}{24kD\sin\theta}[(N_1+N_2)Y_+ + (N_1-N_2)Y_- + \tag{1}$$

$$N_3 \ln\frac{(p-k)}{(p+k)} + N_4 + 18k^3\sin^2\theta\cos\theta(\Sigma_1+\Sigma_2)],$$

where:

$$D = (9k^2\cos^2\theta + 7p^2)(k^4\cos^4\theta - 2k^2m^2 sin^2\theta - p^4);$$

$$N_1 = 9k^2\cos^3\theta(p^2+2k^2) + 6kp\cos\theta(27p^2+11kp-27k^2) + 27k^4\cos\theta;$$

$$N_2 = kp\cos^2\theta(11p^2+76k^2) - 162p^2m^2 + 33k^3p;$$

$$N_3 = p\cos\theta[243m^2p\cos^4\theta - cos^2\theta(324m^2p - 54k^3) + 22kp^2 - 243m^2p + 164k^3];$$

$$N_4 = -\frac{1}{4}k\sin^2\cos\theta[72\cos^2\theta(27p^3-18k^2p+k^3)+27(97k^2p-24p^3)-8(22kp^2+45k^3)];$$

$$\Sigma_1 = \frac{2}{p^2}\sum_i \sqrt{p^2-m_i^2}(2p^2+m_i^2)\theta(p-m_i);$$

$$\Sigma_2 = \frac{1}{p^2}\sum_i [3m_i^2 p\ln[\frac{p-(p^2-m_i^2)^{1/2}}{p+(p^2-m_i^2)^1/2}] - 4(p^2-m_i^2)^{3/2}]\theta(p-m_i);$$

$$Y_\pm = \ln[\frac{(p\pm k\cos\theta)^2}{m^2}].$$

In equation (1) the polarization of the quark depends on three kinematic variables: the quark momentum k, the gluon momentum p, the scattering angle θ; and the

mass of the final state quark m. The summations are made over all intermediate quark masses m_i. The axis of the polarization is along the vector given by the following expression:

$$\frac{\mathbf{p_a} \times \mathbf{p_c}}{|\mathbf{p_a} \times \mathbf{p_c}|}.$$

Where p_a and p_c are the center of mass momenta of the incoming gluon and the produced quark, respectively. The calculation using formula (1), which takes into account only polarization acquired through gluon fusion appeared to roughly fit the kinematic dependence of the Λ^0 polarization data, see Figure 3. Indeed, for the Λ^0s produced by protons in inclusive reaction $p+p \to \Lambda^0 + X$ the creation of the strange quark through gluon fusion may be significant or even the dominant process at high P_t and small x_f, see Ref. [5]. In 1996 Dharmaratna et al. [8] also calculated the contribution to the resulting quark polarization from three other QCD subprocesses (in addition to the gluon fusion): quark-quark scattering, quark-gluon scattering, and quark pair annihilation.

Quark-quark scattering

The quark-quark scattering process (Figure 4) is merely an analog to the QED electron-muon scattering. One gluon exchange shown in Figure 4(a) is the lowest order scattering subprocess contributing to the resulting quark polarization. The single fourth order diagram contributing to the polarization and involving two gluons is shown in Figure 4(b). The contribution to the polarization of the quark resulting from the above process is given by the equation (14) of Ref. [8].

Quark-gluon scattering

The lowest order Feynman diagrams for the $q + g \to q + g$ scattering is shown in Figure 5. The fourth order diagrams contributing to the polarization are shown

in Figure 5(b). The resulting polarization can be calculated according to equation (17) of Ref. [8].

Quark pair annihilation

The case of quark-antiquark annihilation $q + \bar{q} \rightarrow q' + \bar{q}'$ (Figure 6) is substantially similar to the case of $e^+ + e^- \rightarrow \mu^+ + \mu^-$ considered in QED. The Feynman diagrams for this case are shown in Figure 6(a) (the lowest order) and Figure 6(b) (the fourth order). Equation (21) of Ref. [8] gives the contribution of this process to the polarization.

Kinematic dependence of the polarization

As indicated by equation (1) above, the magnitude of the polarization depends on several kinematic variables. The dependence of the magnitude of the polarization on the scattering angle and the momentum of the produced quark is shown in Figures 7 and 8 (taken from Ref. [8]).

Other recently developed polarization models

Quite recently at least two other models were developed based on the QCD treatment of the production of polarized quarks [9], [10].

Constituent quark model

This model assumes that the interacting hadron consists of constituent quarks, i.e. quasiparticles that contain a valence quark surrounded by a cloud of quark-antiquark pairs of different flavors [9]. For instance, a U constituent quark contains pairs of strange and antistrange quarks. It is further assumed that the spin of the constituent quark is mainly due to the orbital angular momentum of the quark-antiquark pairs inside the constituent quark. The authors proposed two mechanisms

for inclusive production of the hyperon. According to the first model the hyperon is produced by the recombination of the constituent quark with a massive s-quark from the quark-antiquark pair. According to the second one the constituent quark scatters in the mean field, excites and decays producing the strange quark which subsequently fragmentates into the hyperon. The first mechanism results in an unpolarized hyperon while in the second one the hyperon acquires a polarization due to multiple scattering in the mean field. On the other hand the first mechanism takes place at small P_t, the second one at high P_t. That is how the model accounts for the P_t dependence of the polarization magnitude. The polarization, according to this model, is caused by the orbital angular momentum of the quark-antiquark pairs inside the constituent quark. The dependence of the Λ^0 polarization on P_t, calculated according to this model [9], was in the good agreement with experimental data in a wide P_t range and with $X_f = 0.44$, see Figure 9.

Quark recombination model

The quark recombination model (QRC model) is the most likely candidate for the hyperon production process at small P_t. According to the DeGrand and Miettinen model (DM model), an early version of the QRC model [7], the hadron is produced through quark recombination with the following relation between the momentum and spin of the quark during the recombination process: if the slow quark from the sea combines with the fast valence quark, its spin will more likely point down in the scattering plane, whereas fast valence quarks recombine with fast quarks having their spin pointing up, see Ref. [7]. The authors proposed that this rule originates in the Thomas precession that the quarks participating in the recombination process experience. The Λ^0 polarization calculated using perturbation

theory and taking into account the Thomas precession of the s-quark demonstrated qualitative agreement with the experimentally observed X_f and P_t-dependence of the polarization, see Ref. [7].

In Ref. [10], the authors enhanced the recombination model by adding the correct treatment of the relativistic kinematics of the quarks, which automatically included the Thomas precession. The enhanced model correctly described the quantitative behavior of the polarization of various hyperons in the low P_t range, see Figure 10.

Quarks

Charge	Up		Charm		Top	
+2/3	u	R.G.B. 5	c	R.G.B. 1.500	t	R.G.B. 180.000
	Down		Strange		Bottom	
–1/3	d	R.G.B. 8	s	R.G.B. 160	b	R.G.B. 4.250

Leptons

Charge	Electron		Muon		Tau	
–1	e	.511	μ	105.7	τ	1.777
	Electron Neutrino		Muon Neutrino		Tau Neutrino	
0	ν_e	0?	ν_μ	0?	ν_τ	0?

Table 1: The Standard Model. The table shows properties of the six generations of quarks and leptons.

Interaction	Intensity	Characteristic radius
Strong (Color)	$a_s \approx 1$	Confignment
Strong (Nuclear)	$g_\pi^2/4\pi \approx 14$	$\approx m_\pi^{-1} \approx 1.5F$
Electromagnetic	$a = \frac{1}{137.036}$	∞
Weak	$G_F = 1.02684 \cdot 10^{-5} m_p^{-2}$	$\approx M_W^{-1} \approx 10^{-3}F$
Gravitational	$G_N = M_{P1}^{-2}$ $M_{P1} = 1.22 \cdot 10^{19}$ GeV	∞

Table 2: Phenomenology of interactions.

S						T
0		n ddu		p duu		1/2
–1	Σ^{--} dds		Λ^0, Σ^0 dus		Σ^+ uus	1
–2		Ξ^{--} dss		Ξ^0 uss		1/2
	+1	+1/2	0	–1/2	–1	T_3

Table 3: Baryon Octet.

Mass, Mev	S							T
1236	0	Δ^{--} ddd		Δ^{+} ddu		Δ^{+} duu		Δ^{++} uuu	3/2
1385	–1		Σ^{*-} dds		Σ^{*0} dus		Σ^{*+} uus		1
1530	–2			Ξ^{*-} dss		Ξ^{*0} uss			1/2
1672	–3				Ω^{--} sss				0
		+3/2	+1	+1/2	0	–1/2	–1	–3/2	T_3

Table 4: Baryon Decouplet

Particle	Wave Function	Q	S	C	B	Spin	Isospin
Baryons							
p	$\|2uud - udu - duu > /\sqrt{6}$	+1	0	0	0	1/2	1/2
n	$\|udd - dud - 2ddu > /\sqrt{6}$	0	0	0	0	1/2	1/2
Λ^0	$\|usd - sud - dsu - sdu > /2$	0	-1	0	0	1/2	0
Σ^+	$\|2uus - usu - suu > /\sqrt{6}$	+1	-1	0	0	1/2	1
Σ^0	$\|2uds + 2dus - usd - dsu -$ $-sud - sdu > /\sqrt{12}$	0	-1	0	0	1/2	1
Σ^-	$\|2dds - dsd - sdd > /\sqrt{6}$	-1	-1	0	0	1/2	1
Ξ^0	$\|uss + sus - 2ssu > /\sqrt{6}$	0	-2	0	0	1/2	1/2
Ξ^-	$\|dss + sds - 2ssd > /\sqrt{6}$	-1	-2	0	0	1/2	1/2
Δ^{++}	$\|uuu >$	+2	0	0	0	3/2	3/2
Δ^+	$\|uud + udu + duu > /\sqrt{3}$	+1	0	0	0	3/2	3/2
Δ^0	$\|udd + dud + ddu > /\sqrt{3}$	0	0	0	0	3/2	3/2
Δ^-	$\|ddd > /\sqrt{3}$	-1	0	0	0	3/2	3/2
Mesons							
π^+	$\| - u\bar{d} >$	+1	0	0	0	0	1
π^0	$\|u\bar{u} - d\bar{d} > /\sqrt{2}$	0	0	0	0	0	1
π^-	$\|d\bar{u} >$	0	0	0	0	0	1
η^-	$\|u\bar{u} + d\bar{d} - 2s\bar{s} > /\sqrt{6}$	0	0	0	0	0	0
K^+	$\| - u\bar{s} >$	+1	+1	0	0	0	1/2
K^0	$\| - d\bar{s} >$	0	+1	0	0	0	1/2
$\bar{K}^0$	$\|s\bar{d} >$	0	-1	0	0	0	1/2
K^-	$\| - s\bar{u} >$	-1	-1	0	0	0	1/2
D^+	$\| - c\bar{d} >$	+1	0	+1	0	0	1/2
D^0	$\|c\bar{u} >$	0	0	+1	0	0	1/2
D^0	$\|c\bar{u} >$	0	0	+1	0	0	1/2

Table 5: Particle Properties

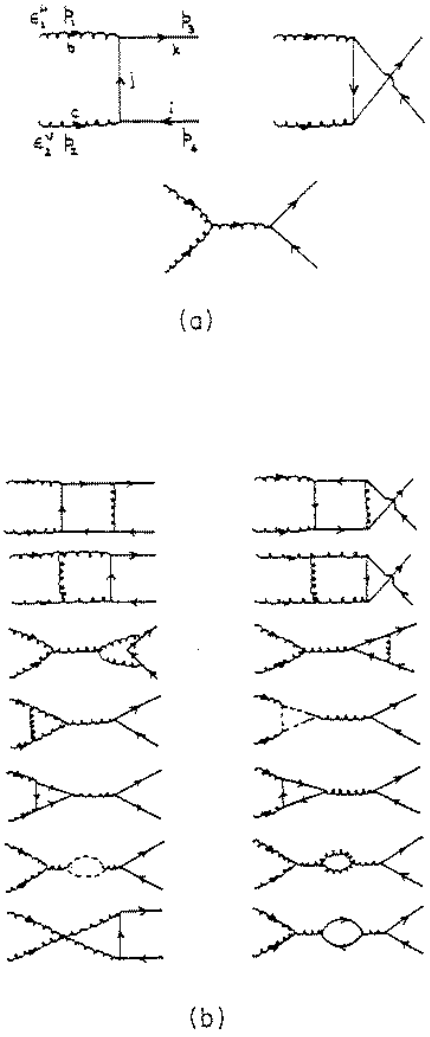

Figure 2: Processes contributing to the single quark polarization through the gluon-gluon fusion. Plots (a) and (b) show the lowest order and the fourth order diagrams, respectively, see Ref. [5].

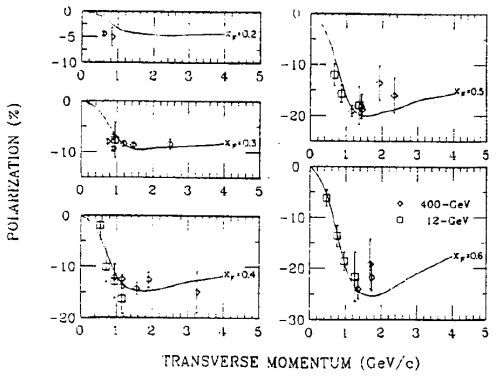

Figure 3: Fit to the Λ^0 polarization data. The fit was made using formula (1), see Ref. [5].

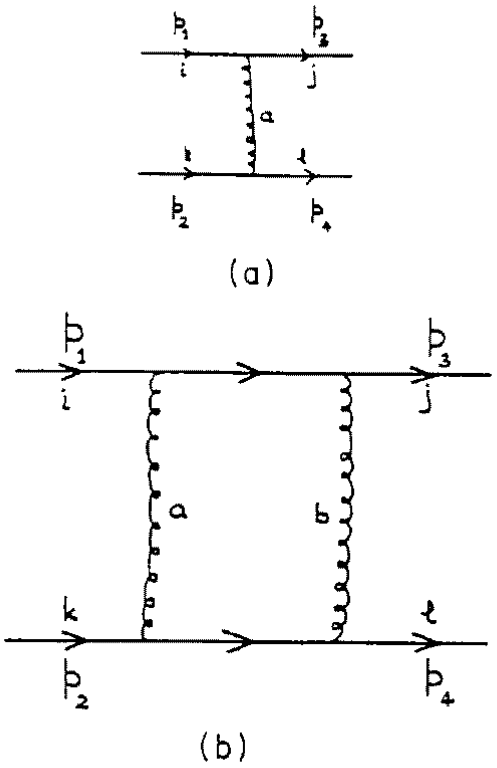

Figure 4: Processes contributing to the single quark polarization through the quark-quark scattering. Plots (a) and (b) show the lowest order and the fourth order diagrams, respectively, see Ref. [8].

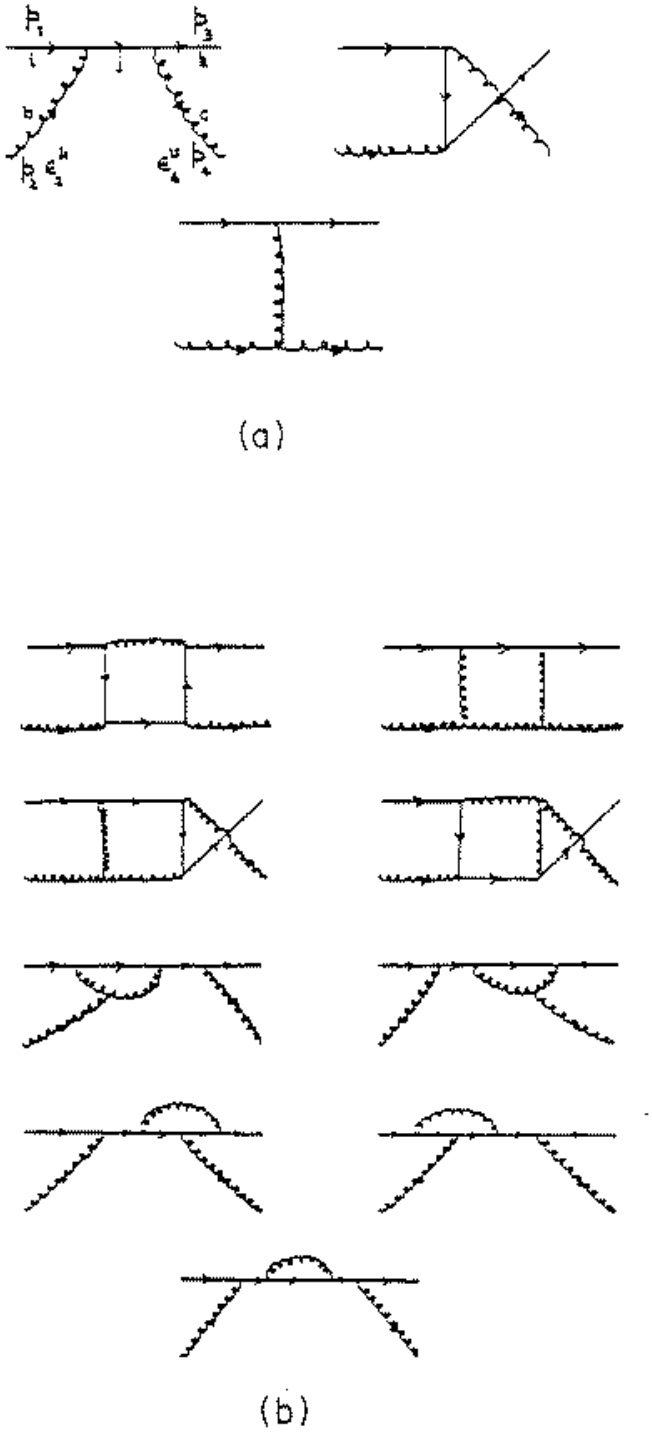

Figure 5: Processes contributing to the single quark polarization through the quark-gluon scattering. Plots (a) and (b) show the lowest order and the fourth order diagrams, respectively, see Ref. [8].

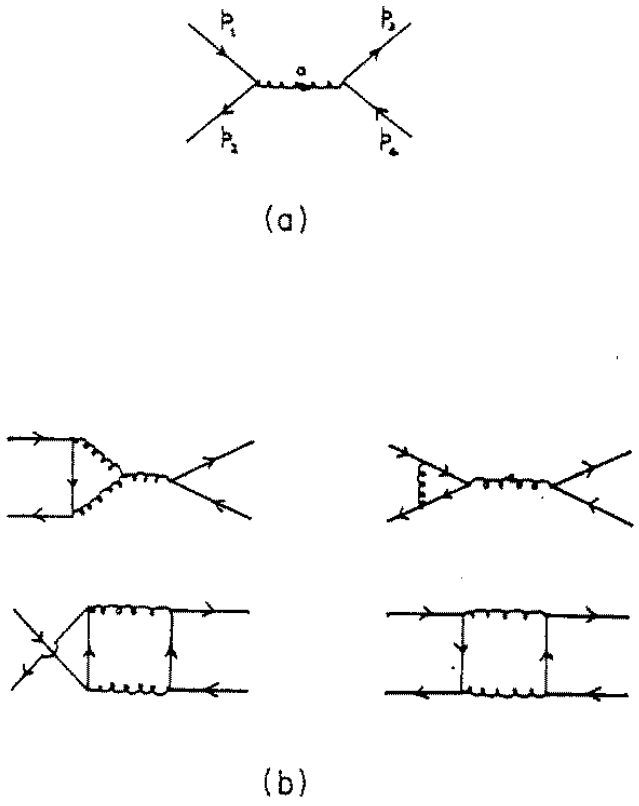

Figure 6: Processes contributing to the single quark polarization through the quark pair anihilation. Plots (a) and (b) show the lowest order and the fourth order diagrams, respectively, see Ref. [8].

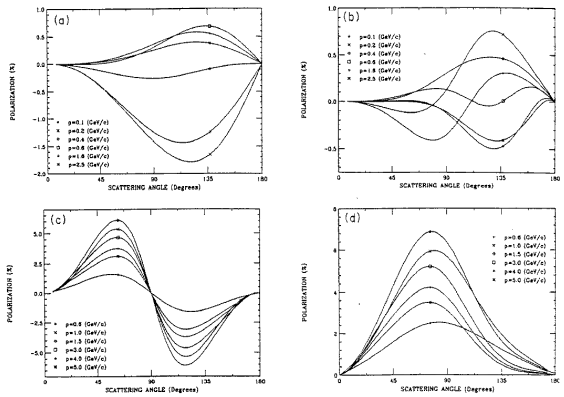

Figure 7: The scattering angle dependence of the contributions of the four QCD subprocesses to the quark polarization magnitude. Plot (a) corresponds to the gluon-gluon fusion, plot (b) – to quark-quark scattering, plot (c) – to quark-gluon scattering, and plot (d) – to quark pair anihilation, see Ref. [8].

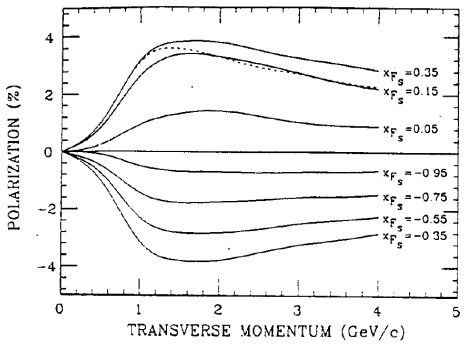

Figure 8: Strange quark polarization. The polarization was calculated in the proton center of mass frame as a function of P_t of the strange quark calculated using the gluon fusion model for various values of X_f, see Ref. [8].

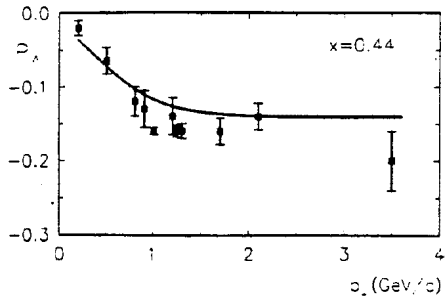

Figure 9: The P_t-dependence of the Λ^0 polarization. The solid lines are calculated using the constituent quark model. The comparison is made with the experimental data corresponding to $X_f = 0.44$, see Ref. [9].

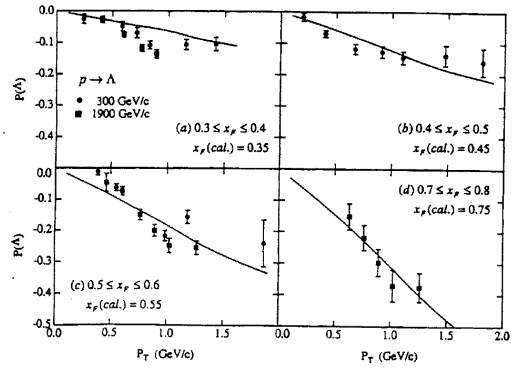

Figure 10: The P_t-dependence of the Λ^0 polarization. The solid lines are calculated using the constituent quark model. The comparison is made with the experimental data, see Ref. [10].

CHAPTER III

MEASURING POLARIZATION

What is Polarization?

Production polarization is the measure of the asymmetry in the number of Σ^+ hyperons produced with the positive and the negative projections of the spin vector onto one of the axis directions:

$$|\vec{P}| = \frac{N\uparrow - N\downarrow}{N\uparrow + N\downarrow}.$$

Σ^+ is produced in the reaction $p + N \to \Sigma^+ + X$. Parity conservation requires the polarization to be proportional to the following vector product:

$$\vec{P} \sim \vec{p}_{proton} \times \vec{p}_{\Sigma^+}.$$

The convention on the choice of the direction of the polarization vector is such that for the protons pointing at the target at an angle $+4$ mrad with the direction of the outgoing hyperons in the xz-plane, the direction of the polarization of the hyperons will be *down* (in accordance with the above vector product), see Figure 11. For the targeting angle -4 mrad the direction of the polarization will be *up*, see Figure 11. The production polarization of Σ^+ hyperon can be measured by looking at its decay. In the hyperon decay of the type $\Sigma^+ \to B + \pi$ angular momentum conservation requires that the angular distribution of the outgoing baryon B (p or n) in the center of mass system of the Σ^+ be given by the following formula:

$$I(\theta,\phi) = \frac{1}{N_0}\frac{dN}{d\Omega} = \frac{1}{4\pi}(1+\alpha\vec{P}\cdot\frac{\vec{p}_B}{|p_B|}) = \frac{1}{4\pi}(1+\alpha|P|\cos\Theta_y) = \frac{1}{4\pi}(1+A\cos\Theta_y). \quad (2)$$

Quantity $\vec{A} = \alpha\vec{P}$ is called asymmetry. Here $\vec{p}_B$ is the momentum vector of the Σ^+ daughter baryon (in the Σ^+ center of mass system), Θ_y is the angle that the track of the daughter baryon B forms with the vertical axis, see Figure 11.

To obtain this formula one should write down the angular momentum state of the combination of the two particles: baryon B with spin 1/2 and π - meson with spin zero. If the parity were conserved, the parity conservation would yield the following equation, see Ref. [16]:

$$P(\Sigma^+) = P(\pi^0) \cdot P(p) \cdot (-1)^l.$$

Σ^+ has $P = +1$, P(B) is also +1, and $P(\pi) = -1$, see Ref. [19]. This requires the orbital angular momentum l of the $B - \pi$ pair be equal to 1.

Angular momentum conservation requires that the orbital angular momentum l of the $(B - \pi)$ pair to be 0 or 1. Since Σ^+ decays through the weak interaction, parity is not conserved. Therefore the wave function of the $B - \pi$ pair will have both S (l=0) and P (l=1) components:

$$\Psi_{B\pi} = A_s \Psi_s(J = 1/2, l = 0) + A_p \Psi_p(J = 1/2, l = 1),$$

where A_s and A_p are the amplitudes of S and P waves, respectively. Using Clebsch-Gordon coefficients the total three dimensional wave function of the $B - \pi$ pair can be further written in the following way:

$$\Psi_{p\pi^0} = A_S Y_0^0 \chi^+ + A_P(\sqrt{\frac{2}{3}} Y_1^1 \chi^- \sqrt{\frac{1}{3}} Y_1^0 \chi^+)$$

The corresponding angular distribution of the decays is given by, see Ref. [16]:

$$I(\theta, \phi) = |\Psi|^2 = \frac{1}{N_0} \frac{dN}{d\Omega} = \frac{1}{4\pi}(1 + \alpha \cdot \vec{P} \cdot \frac{\vec{p}_B}{|p_B|}). \quad (3)$$

Where $\alpha = \frac{-2ReA_S^* A_P}{|A_S|^2 + |A_P|^2}$. For the two main decay modes of the Σ^+ hyperon the values of the parameter α are the following [19]:

$$\alpha = -0.980^{+0.017}_{-0.015}, \Sigma^+ \to p\pi^0;$$

$$\alpha = +0.068 \pm 0.013, \Sigma^+ \to n\pi^+.$$

In the SELEX apparatus the targeting angle is in the horizontal plane and the direction of the polarization vector $\vec{P}$ is along the Y axis. The magnetic field in all the magnets of the apparatus is also directed along the Y axis, which means the polarization vector does not precess in the magnetic field. For this reason, the angular distribution of daughter baryons in formula (1) depends only on the angle Θ_y – the angle between the direction of the daughter baryon track and the Y axis, see Figure 11. Note that the angular distribution of daughter protons $I(\theta, \phi)$ from the Σ^+ decay $\Sigma^+ \to p\pi^0$ with $\alpha = -0.980$ is 14 times more asymmetric for a given polarization value then the corresponding angular distribution of neutrons from the $\Sigma^+ \to n\pi^+$ decay with $\alpha = +0.068$. If the absolute error in the measured asymmetry is the same for both decays,[3] the $\Sigma^+ \to p\pi^0$ decay is a much more sensitive analyzer of the Σ^+ production polarization than the $\Sigma^+ \to n\pi^+$ decay.

Bias Cancellation Techniques

If one wants to measure the angular distribution of the daughter baryons $I(\theta, \phi)$ directly, one must take into account the acceptance function $a(\Omega)$ of the apparatus and the data analysis. The acceptance function $a(\Omega)$ is simply the efficiency of detecting a given particle (daughter baryon here) going into solid angle Ω in the Σ^+ rest frame. This function is different for each experimental apparatus and data analysis. It reflects the efficiency and geometrical properties of various detectors forming the apparatus, as well as the reconstruction efficiency of the particles by the analysis algorithm. The following is the angular distribution of daughter baryons

[3] The absolute error in the measured asymmetry depends on the resolution of the decay angle measurement and the number of the decay events used.

actually observed:

$$\frac{dN}{d\Omega}(EXP) = a(\Omega) \cdot N_0 \frac{1}{4\pi}(1 + |A| \cdot \cos\Theta_y).$$

When such a measurement is made, it is hard to determine whether the given measured asymmetry in $\frac{dN}{d\Omega}$ is caused by the polarization factor $|A| \cdot \cos\Theta_y$ or by the non-uniform acceptance of the apparatus $a(\Omega)$. In other words, if we want to calculate the polarization we would need to write the last formula in the following form:

$$|P| = \frac{1}{\alpha \cdot \cos\Theta_y} \cdot (\frac{4\pi}{a(\Omega)} \frac{1}{N_0} \frac{dN}{d\Omega}(EXP) - 1).$$

Ideally, the acceptance of the apparatus is 1 independently of the angle Ω. All the dependencies of the $|P|$ on the angle Ω will cancel out and we will get a constant. In practice, however we are dealing with an unknown function $a(\Omega)$ which generally is not uniformly equal to 1. In this, real case, it is impossible to calculate $|P|$ without knowing $a(\Omega)$.[4] For this reason, it is desirable to eliminate the acceptance of the apparatus $a(\Omega)$ from the final answer for $|P|$. If two samples of data with opposite directions of the polarization vector are taken, the apparatus acceptance function can be eliminated from the resulting expression for $|P|$ using one of the two methods: the method of the arithmetic mean and the method of the geometric mean.

Method of arithmetic mean

The two samples of data with opposite (vertical) directions of the polarization vector may be produced by using two complementary primary beam targeting angles in the horizontal plane, see Figure 11. Dividing the difference of the angular distributions of the decay particles corresponding to the positive and negative proton targeting angles by the acceptance of the apparatus function $\alpha(\Omega)$, which is the

[4] In some cases the function $a(\Omega)$ can be estimated by using Monte-Carlo simulation.

normalized sum of these distributions, one can eliminate the $\alpha(\Omega)$:

$$A_i = \frac{1}{\cos\Theta_i} \frac{\frac{1}{N_0^+}N_i^+ - \frac{1}{N_0^-}N_i^-}{\frac{1}{N_0^+}N_i^+ + \frac{1}{N_0^-}N_i^-}$$

The number of baryons here has been averaged over the azimuthal ϕ angle and the Θ angle space has been subdivided into i bins designated with index i. In this formula $N_i^{\pm} = \frac{dN^{\pm}}{d\cos\Theta_i}$ is the number of baryons with $\cos\Theta_y$ within the i-th bin for the positive (negative) targeting angle. This method presents a problem of choosing the correct normalization constant $N_0^{\pm}$. If the average acceptances for the beam components with positive and the negative targeting angles are the same, the total number of counts in the corresponding $\cos\Theta_y$ histogram can be used. On the other hand, if the average acceptances are different, [5] one should probably normalize $N_i^{\pm}$ by the total number of the events (triggers) in the data sample corresponding to the respective beam targeting angle.

Method of geometric mean

The method of the geometric mean [17] does not use the normalization of the number of the events in the $\cos\Theta_y$ bin. Thereby it avoids the problem of choosing the correct normalization factor $1/N_0^{\pm}$. In the geometric mean method A_i is written as:

$$A_i = \frac{1}{\cos\Theta_i} \frac{\sqrt{N_i^{+r} \cdot N_i^{-l}} - \sqrt{N_i^{-r} \cdot N_i^{+l}}}{\sqrt{N_i^{+r} \cdot N_i^{-l}} + \sqrt{N_i^{-r} \cdot N_i^{+l}}}.$$

In this formula, bins containing events with the negative values of $\cos\Theta_y$ are designated by superscript l, while bins corresponding to the positive $\cos\Theta_y$ by subscript r. Here again the superscripts $+$ and $-$ designate data sets corresponding to positive

[5] The difference in the average acceptance may be due to an asymmetric "dip" (with respect to $\cos\Theta_y$) in the acceptance function due to some kind of inefficiency in the detectors. The particle distributions corresponding to the two targeting angles are also asymmetric with respect to $\cos\Theta_y$. Accordingly, the data set that would have a higher number of particles at said "dip" will loose more events due to the inefficiency and its average acceptance will be lower.

(negative) beam targeting angle in the horizontal plane. Variations in the polarization and acceptance cancel to the first order, see Ref. [17] if one uses the method of the geometric mean.

Properties of Σ^+ Hyperon

Knowing the properties of the Σ^+ hyperon is important for its identification in the apparatus. Σ^+ hyperon has a mass of 1189.37 ± 0.07 MeV/c^2 and mean life $\tau = 0.799 \cdot 10^{-10} s$ in its own rest frame [19]. In this experiment the $\Sigma^+ s$ are produced in the hyperon production target of the apparatus and are selected by the Hyperon Magnet to have a nominal momentum of 572 GeV/c. The γ factor of the Σ^+ hyperon with this value of the momentum may be found in the following way:

$$\gamma \approx \frac{p}{m_{\Sigma^+} c} \approx 481.$$

The mean distance the Σ^+ travels before it decays is accordingly:

$$l = \gamma c \tau \approx 11m.$$

For a beam momentum of 500 GeV/c the decay length becomes 9.61m, and for 375 GeV/c this number is 7.21m. Σ^+ hyperon has two principal decay modes: $\Sigma^+ \to p\pi^0$ with branching ratio 51.57% and $\Sigma^+ \to n\pi^+$ with branching ratio 48.30%.

Kinematics of the Σ^+ Decays

Knowing the kinematic properties of the Σ^+ decays is important for the efficient selection of those decays for polarization measurement. In the Σ^+ decay the daughter particles (baryon B and pion π) each carry the momentum (in the Σ^+ hyperon center of mass frame) given by the following formula (derived from the 4-momentum conservation):

$$p_{CM} = \frac{1}{2 \cdot m_{\Sigma^+}} \cdot \sqrt{(m_{\Sigma^+}^2 - (m_B - m_\pi)^2) \cdot (m_{\Sigma^+}^2 - (m_B + m_\pi)^2)}.$$

For $\Sigma^+ \to p\pi^0$ $p_{CM} = 189$ MeV/c, while for the second decay $\Sigma^+ \to n\pi^+$ this value is 185 MeV/c. If the direction cosines[6] of the daughter baryon in the Σ^+ center of mass system are $\cos\Theta_x$, $\cos\Theta_y$, and $\cos\Theta_z$, the relevant relativistic transformations relate these angles with the decay angle θ in the lab frame in the following way:

$$\cos\Theta_x = \frac{p_B}{p_{CM}} \cdot \theta_x;$$

$$\cos\Theta_y = \frac{p_B}{p_{CM}} \cdot \theta_y;$$

$$\cos\Theta_z = -\frac{E_{CMB}}{p_{CM}} + \frac{m_{\Sigma^+}}{p_{CM}} \cdot \frac{p_B}{p_{\Sigma^+}}.$$

These formulas are used to calculate the direction cosines of the baryon track in the Σ^+ center of mass frame from the experimentally measured momenta and track angles of these particles in the lab frame.

Note that $\cos^2\Theta_x + \cos^2\Theta_y + \cos^2\Theta_z = 1$ and $\theta_y^2 + \theta_x^2 = \theta^2$, the Σ^+ decay angle in the lab frame. Because of these relations, θ and $R = \frac{p_B}{p_{\Sigma^+}}$ are related (for a given p_{Σ^+}) by a mutually unique relationship. A plot of the decay angle Θ as a function of R is shown in Figure 24 for $\Sigma^+ \to p\pi^0$ decay mode and the Σ^+ momenta of 572 GeV/c. This plot makes it easy to select appropriate Σ^+ decays using proper R and θ cuts.

Existing Data on the Polarization of Σ^+ Hyperons

Experiments studying the hyperon polarization proceeded since the discovery by Bunce et al. of a large transverse polarization of Λ^0s produced by proton beam at Fermilab [18]. In that experiment Λ^0s were produced by unpolarized 300 GeV/c protons in an unpolarized target in the inclusive reaction $p + Be \to \Lambda^0 + X$. The

[6] The cosines of the three angles that the baryon track forms with respective coordinate axis in the Σ^+ center of mass frame. Note that $\cos\Theta_y$ is used to measure Σ^+ polarization.

polarization of Λ^0 hyperon was analyzed through its decay $\Lambda^0 \to p\pi^-$. The polarization was observed to increase monotonically from zero to about 0.28 with P_t increasing from zero to about 1.5 GeV/c, and was almost independent on the center of mass energy. The discovery that Λ^0 hyperons are produced polarized prompted extensive experimental work in this area which resulted in the discovery of similar hyperon production polarization in the following hyperon production processes: $p \to \Xi^0$ [3]; $p \to \Xi^-$ [24]; $p \to \Sigma^+$ [22]; and $p \to \Sigma^-$ [23]. The dependence of Λ^0 polarization on the material of the production target was first reported by K. Heller et al. in Ref. [3, 4]. While there is no simple satisfactory explanation for the entire polarization phenomenon, the dependence of the polarization on the A of the target can not be explained at all at the today's level of knowledge in the field.

In a recent work done at Fermilab by the E761 collaboration, Antonio Morelos et al. [1], high statistics data samples were used to measure with high accuracy polarization and magnetic moments of Σ^+ and $\bar{\Sigma}^-$ hyperons. The Σ^+ and $\bar{\Sigma}^-$ hyperons were produced by 800 GeV/c proton beam on a copper target. The polarization of the Σ^+ hyperon was found to be of the order of -10 to -14% for 1 GeV/c $< P_t <$ 1.5 GeV/c. Another analysis by the same group [2] used the same data to study the P_t and X_f dependence of the polarization of Σ^+ hyperons in the range 1 GeV/c $< P_t <$ 1.5 GeV/c. Σ^+ polarization was observed to increase with X_f slower at higher P_t values.

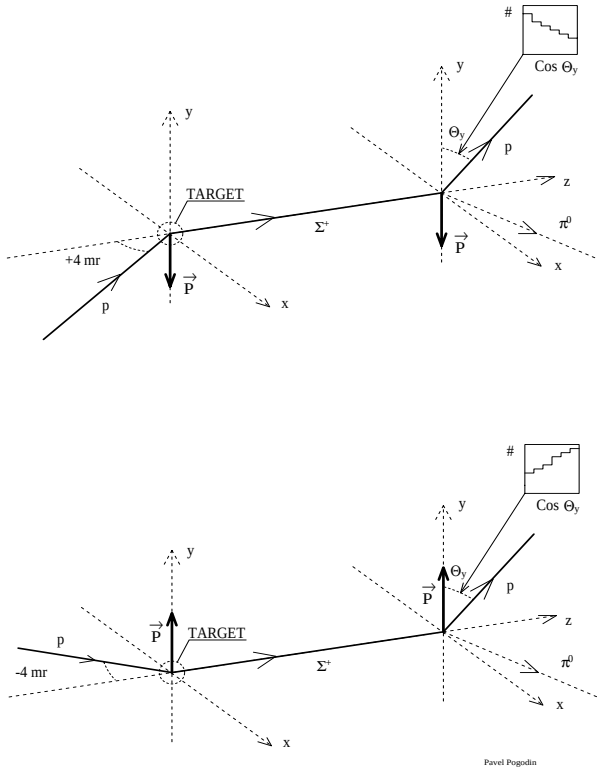

Figure 11: Production of polarized Σ^+ hyperon and its decay. The proton beam hits the target at two non-zero targeting angles of ± 4 mrad. This results in production of polarized Σ^+ hyperons with two opposite polarization vector directions. The hyperons subsequently decay through $\Sigma^+ \to B + X$ parity non-conserving decay mode. The asymmetry in cosine of the angle Θ_y that the track of the Σ^+ daughter baryon (proton in the case shown) forms with the vertical axis (in the center of mass frame of the Σ^+) can be used to measure the Σ^+ production polarization.

CHAPTER IV

EXPERIMENTAL APPARATUS

Overview of the Experimental Apparatus

The experimental apparatus used to measure the hyperon polarization was designed to produce polarized Σ^+ hyperons, detect their decays, and measure kinematic parameters (angles, momenta) of their charged daughter particles (p, π^+). Production of polarized Σ^+ hyperons was accomplished through steering and focusing the unpolarized primary proton beam from the Tevatron on the unpolarized hyperon production target at two complementary non-zero targeting angles in the horizontal plane. Such beam targeting produces hyperons with polarization vector directed vertically, see Figure 11. The Hyperon Magnet of the apparatus was then used to perform the momentum selection of the produced hyperons. Because the magnetic field in the Hyperon Magnet also points vertically, the spin of the hyperons does not precess in the magnetic field and the polarization vector is not affected by the hyperons' passing through the magnetic field of the Hyperon Magnet and other magnets of the apparatus. The portion of the experimental apparatus downstream of the production target forms a spectrometer for studying the decays of the polarized hyperons produced on the target.

Fermilab Accelerator Complex

The 800 GeV/c primary proton beam used in the present study to produce Σ^+ hyperons was delivered by the Tevatron accelerator of the Fermilab's Accelerator Complex. The schematic diagram of the accelerator complex is shown in Figure 12. Various stages and components of the complex are presented in Table 6. The beam

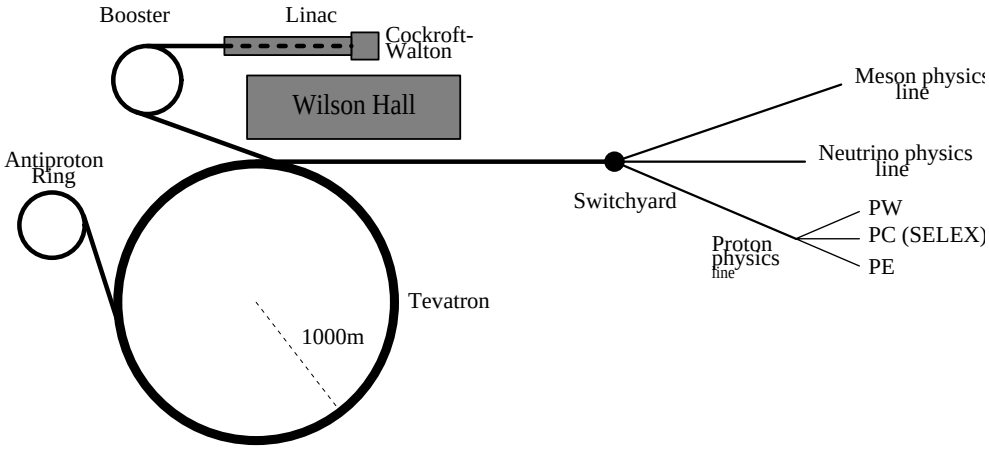

Figure 12: Fermilab accelerator complex

delivered by the accelerator is derived from negative hydrogen ions generated by the Magnetron ion source. The Cockcroft-Walton electrostatic accelerator is used on the first acceleration stage. After the Cockcroft-Walton, the ions pass though the Linac (linear accelerator), which is the second accelerator of the complex. After that, the still negative ion beam enters the third accelerator, called the circular Booster, where the ions lose both of their electrons, becoming protons. The protons are then injected into the Main Ring and, finally, the Tevatron, both of which occupy the circular tunnel 1 km in radius. When the accelerator operates in the fixed target mode, the proton beam is being extracted and distributed by the Switchyard among users in Meson, Proton, and Neutrino experimental areas.

Hyperon Beam

In the present measurement the hyperons were produced by the 800 GeV/c primary proton beam steered and focused onto a 1-interaction length Cu or Be target that could be moved into its position using a remotely controlled stepping

Acceleration stage	Component type	Final beam momentum	Particle
Cockcroft-Walton	Static Charge	750 KeV/c	H^-
Linac	Linear (RF) Accelerator	200 MeV/c	H^-
Booster	Synchrotron	8 GeV/c	p
Main Ring	Synchrotron	150 GeV/c	p
Tevatron	Synchrotron	800 GeV/c	p

Table 6: Fermilab's Accelerator Complex Components.

motor. Dimensions of the hyperon production targets (taken from the SELEX shop drawings) are given in Table 7. The photograph of SELEX target assemblies is shown Figure 13.

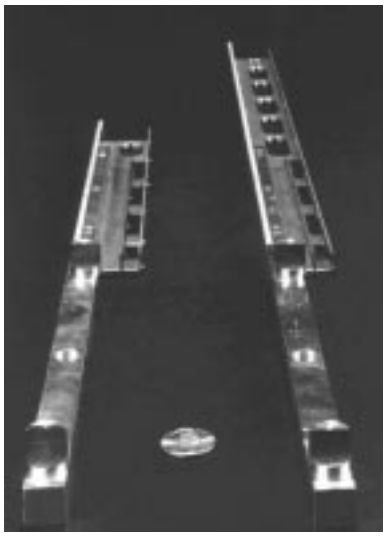

Figure 13: SELEX target assemblies.

Beam Targeting Angles and PC3 Magnets

Dipole targeting magnets PC3BR,[7] PC3V, PC3H1 and PC3H2 shown in Figure 14 were used to set the correct targeting angle in the range -5 mrad to $+5$ mradin

[7] Targeting magnet PC3BR consisted of three identical targeting magnets PC3BR1, PC3BR2, and PC3BR3, with the same value of electric current supplied to them.

Target	X [in]	X [cm]	Y [in]	Y [cm]	Z [in]	Z [cm]
Cu	0.040	0.102	0.080	0.203	5.927	15.055
Be	0.040	0.102	0.080	0.203	16.020	40.691

Table 7: Target dimensions from SELEX shop drawings.

the horizontal plane.[8] The targeting angle in the vertical plane was set at 0. Ta-

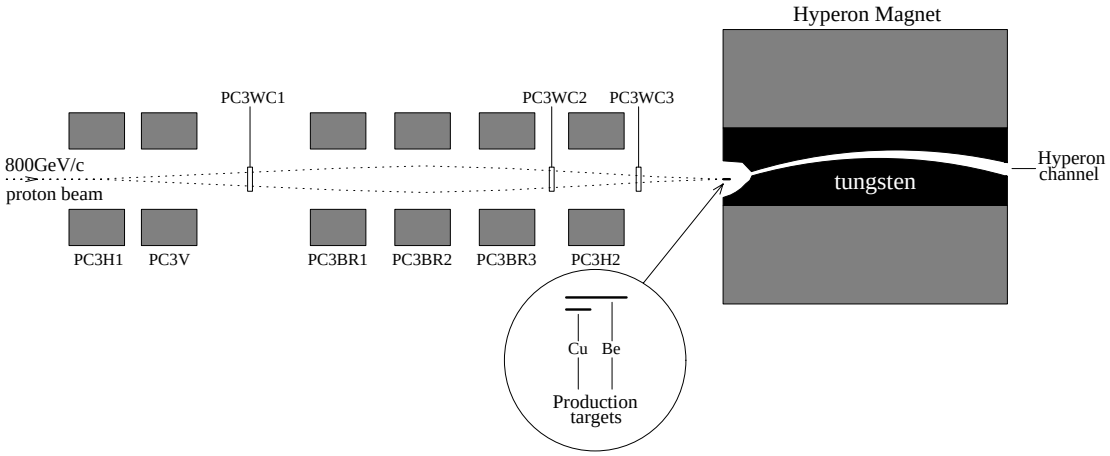

Figure 14: Beam steering and targeting systems.

ble 8 presents the primary beam targeting angles for the primary beam momentum of 800 GeV/c, calculated for $0.3 \leq X_f \leq 0.95$ and 0.5 GeV/c $\leq P_t \leq$ 2.75 GeV/c.

A 7.3 m-long Hyperon Magnet having a curved hyperon channel, see Figures 14 and 15 performed the momentum selection of the particles in the secondary beam by imparting a transverse momentum of up to 7.5 GeV/c. The secondary beam at the exit of the hyperon channel consists of the primary beam protons scattered off the production target as well as secondary particles, primarily Σ^+ hyperons and pions, that are produced in the target, and, possibly, on the walls of the hyperon

[8]See Chapter 7 on the targeting angle calculation for more elaborate description of the targeting magnets.

X_f	P_t [GeV/c]									
(P_{BM}[GeV/c])	0.5	0.75	1	1.25	1.5	1.75	2	2.25	2.5	2.75
0.3(195)	2.56	3.84	5.12	6.41	7.69	8.97	10.25	11.53	12.82	14.1
0.35(227)	2.19	3.29	4.39	5.49	6.59	7.69	8.79	9.89	10.98	12.08
0.4(260)	1.92	2.88	3.84	4.8	5.76	6.73	7.69	8.65	9.61	10.57
0.45(292)	1.7	2.56	3.41	4.27	5.12	5.98	6.83	7.69	8.54	9.4
0.5(325)	1.53	2.3	3.07	3.84	4.61	5.38	6.15	6.92	7.69	8.46
0.55(357)	1.39	2.09	2.79	3.49	4.19	4.89	5.59	6.29	6.99	7.69
0.6(390)	1.28	1.92	2.56	3.2	3.84	4.48	5.12	5.76	6.41	7.05
0.65(422)	1.18	1.77	2.36	2.95	3.55	4.14	4.73	5.32	5.91	6.5
0.7(455)	1.09	1.64	2.19	2.74	3.29	3.84	4.39	4.94	5.49	6.04
0.75(487)	1.02	1.53	2.05	2.56	3.07	3.58	4.1	4.61	5.12	5.64
0.8(520)	0.96	1.44	1.92	2.4	2.88	3.36	3.84	4.32	4.8	5.28
0.85(552)	0.9	1.35	1.8	2.26	2.71	3.16	3.61	4.07	4.52	4.97
0.9(585)	0.85	1.28	1.7	2.13	2.56	2.99	3.41	3.84	4.27	4.7
0.95(617)	0.8	1.21	1.61	2.02	2.42	2.83	3.23	3.64	4.04	4.45

Table 8: Targeting angles (in mrad) for 800 GeV/c primary proton beam momentum and different values of P_t and X_f.

channel. The content of the secondary beam at the exit of the hyperon channel is shown in Table 9. Scattered protons constitute the major fraction of the secondary beam ($\approx 94\%$). Σ^+ and π^+ have approximately the same fractions of about 2.8%.

The value of the electric current in the magnets PC3BR and PC3H2 determined the targeting angle of the primary proton beam in the horizontal plane. In order to "focus" the proton beam on the target for each targeting angle we performed a number of "beam scans" – measurements of the ratio of the intensity of the secondary beam (the particles produced on the target) to the intensity of the primary proton beam as a function of the current in the horizontal bending magnet PC3H1 and vertical bending magnet PC3V. This ratio is also called the "yield" on the target. The maximum of this ratio corresponds to the correct beam steering position. First, the horizontal scan was performed using PC3H1 magnet to determine

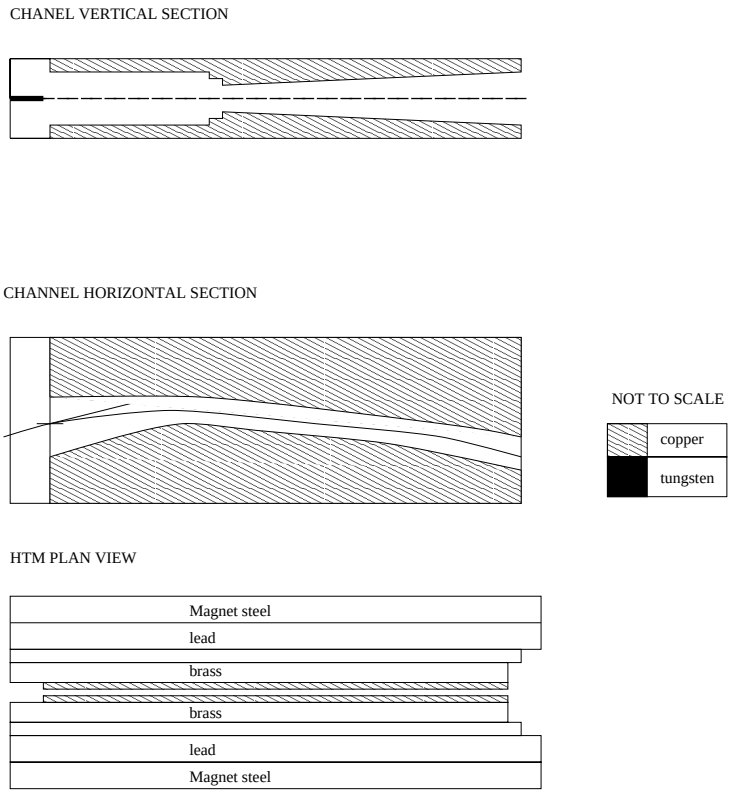

Figure 15: Schematic drawing of the hyperon channel.

the value of the electric current that would give maximum yield on the target. The current in PC3H1 magnet was subsequently set at that value. Then, the vertical scan was performed to get the optimal value of the current in PC3V.

Once the position of the maximum was found, we removed the target and repeated the measurements to determine the ratio of the intensity of the beam of secondary particles produced in the target (target in intensity) to the background intensity (target out intensity). Presumably, the hyperons created in the target have a right value of the targeting angle and P_t, while those which were created elsewhere do not. The ratio of the target in/target out intensities was found to be better than 20:1 for the most runs.

Prticle	Fraction of the beam [%]	Mass $[MeV/c^2]$	Life Time τ[s]	Primary decay mode	γ	Decay length l [m]
π^+	≈ 2.8	139.57	$2.6630 \cdot 10^{-8}$	$\mu^+ + \nu_\mu$ 99.9%	4300	34353
K^+	≈ 0.8	493.77	$1.2371 \cdot 10^{-8}$	$\mu^+ + \nu_\mu$ 63.51% $\pi^+ + \pi^0$ 21.16%	1215	1833
Σ^+	≈ 2.8	1189.37	$0.799 \cdot 10^{-10}$	$p + \pi^0$ 51.57% $n + \pi^+$ 48.30%	504	12.08
p	≈ 94	938.27	∞		639	∞

Table 9: Content of the positive secondary beam produced by primary 800 GeV/c protons at 10 m downstream of the production target, see Ref. [21].

Experimental Apparatus

The portion of the experimental apparatus downstream of the production target is shown in Figure 16. Pions in the secondary beam were separated from the heavier particles using the beam transition radiation detectors (TRD) installed at the exit of the hyperon channel. The $\Sigma^+ \to p\pi^0$ decay mode of the Σ^+ hyperon with branching ratio 52 % was used in the polarization measurement. This mode has a large asymmetry parameter and therefore it is a sensitive analyzer of Σ^+ polarization, see Ref. [19]. The $\Sigma^+ \to p\pi^0$ decay was reconstructed using the track of the Σ^+ hyperon, the track of its daughter proton, and the momenta of these two particles. The track and the momentum of the Σ^+ hyperon was measured using the detectors of the Hyperon Spectrometer, see Figure 16. The Hyperon Spectrometer consists of the Hyperon Magnet and 8 planes of the beam silicon strip detectors (SSD) with resolution 5 μ and aperture 2 cm each. The momentum of the hyperon was reconstructed using the known position of the hyperon production target and the coordinates of the beam track measured in the beam SSD detectors. The momentum resolution of the Hyperon Spectrometer is 0.6%. It is limited mainly by the finite width (1 mm) of the production target, see Table 7.

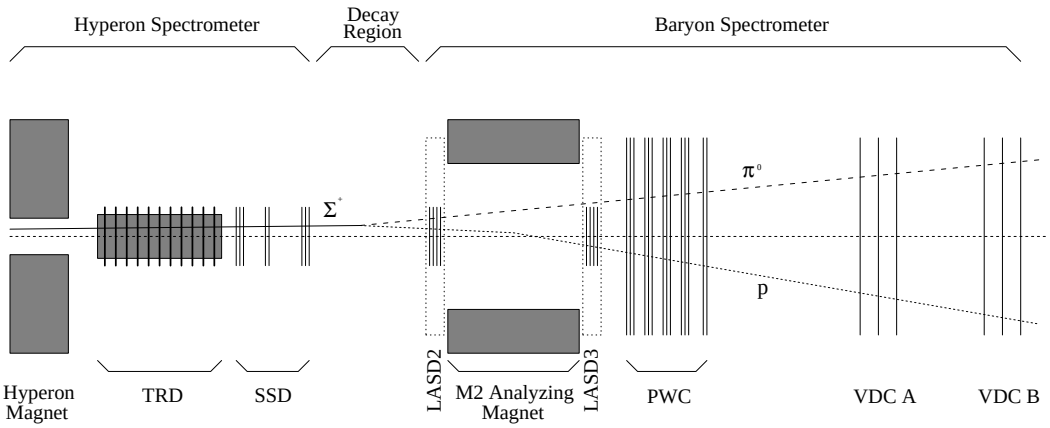

Figure 16: The portion of the experimental apparatus used in the polarization measurement downstream of the production target.

The Baryon Spectrometer of the apparatus, see Figure 16, was used to reconstruct the track and momentum of the hyperon's daughter proton. The Baryon Spectrometer consists of an M2 Analyzing Magnet[9] and 12 planes of the large aperture silicon detector (LASD). Each LASD plane has resolution 14 μm and aperture 6 cm. The LASD planes are grouped into 2 stations LASD2 and LASD3 positioned upstream and downstream of the Analyzing Magnet, respectively.[10] The Baryon Spectrometer also includes 14 planes of large-aperture proportional wire chambers (PWC) with single plane resolution 700 μm and 6 vector drift chambers (VDC). Each of these 6 VDC includes 8 drift chamber planes of the same orientation (X, Y, U and V). The 6 vector drift chambers are grouped into 2 VDC stations VDCA and VDCB. The station VDCA includes vector drift chambers with U, Y, and X-oriented planes, and the station VDCB includes vector drift chambers with V, Y,

[9]M1 Analyzing Magnet positioned upstream of the M2 Analyzing Magnet was switched off and not used in the measurement.

[10]LASD1 station positioned on the downstream side of the M1 Analyzing Magnet, upstream of LASD2 and LASD3 stations, was not used in the measurement.

and X-oriented planes. Each of the six 8-plane vector drift chambers provides approximately 140 μm coordinate resolution.

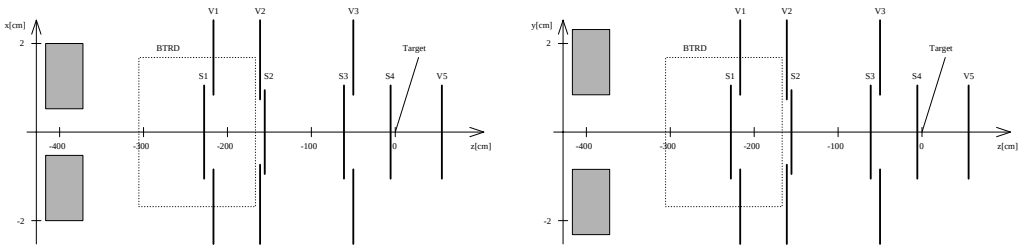

Figure 17: Position of the trigger and veto scintillators used in the trigger T0.

Trigger

The trigger was made using 3 beam scintillators (S_1, S_2, and S_3) and 3 veto scintillators (V_1, V_2, and V_3) placed in such a way that all of the beam particles that fire the trigger go through all the planes of the Hyperon Spectrometer. The trigger used the following logical combination: $S_1 \cdot S_2 \cdot S_3 \cdot \bar{V}_1 \cdot \bar{V}_2 \cdot \bar{V}_3$. The veto scintillators restricted the beam to 2 cm by 2 cm aperture. With this aperture all the Σ^+ daughter protons produced in $\Sigma^+ \to p\pi^0$ decay go through all the detectors used in the measurement. This provides for a uniform acceptance of the apparatus for $\Sigma^+ \to p\pi^0$ decays used to measure the polarization. Figure 17 shows the position of the trigger scintillators in the SELEX coordinate system.

Alignment

The alignment of the apparatus was performed using the tracks of the primary beam protons scattered off the production target. Such tracks go through the decay region without a kink. After all alignment was completed, the same proton tracks were used to determine the resolution of the kink angle reconstruction. The resolu-

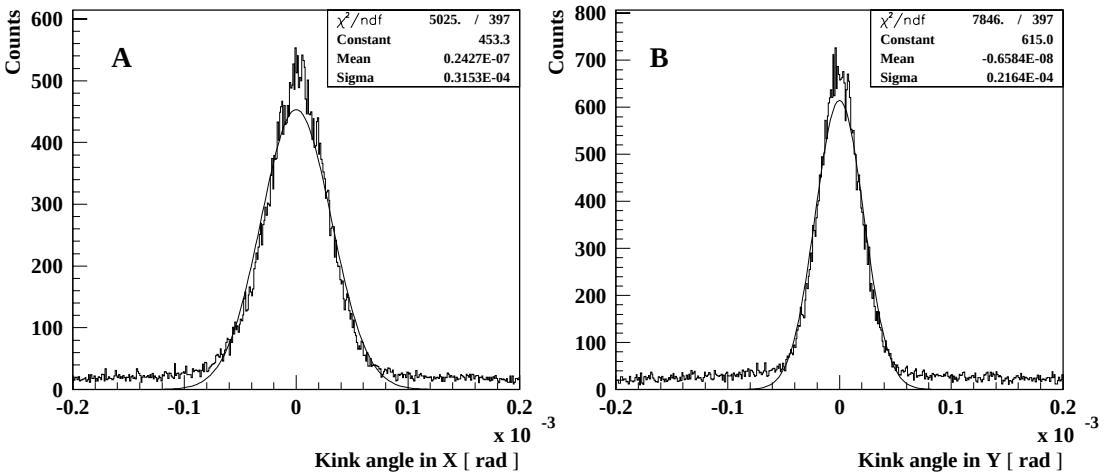

Figure 18: Resolution of kink angle reconstruction. Plot A corresponds to kink angle in X-Z plane for a straight proton track. Plot B shows similar distribution for a a kink angle in Y-Z plane.

tion of the kink angle reconstruction was measured to be approximately 30 μrad in X-Z plane (bending plane of the Analyzing magnet) and approximately 20 μrad in Y-Z plane (non-bending plane of the Analyzing magnet), see Figure 18.

CHAPTER V

DATA ANALYSIS

Overview of the Data Analysis Algorithm

The non-zero polarization of the Σ^+ hyperons produced on the primary target results in an asymmetry in the distribution of the angle that the trajectory of the daughter baryon from the Σ^+ hyperon decay forms with the vertical axis of the SELEX apparatus. Accordingly, the main goal of the entire data analysis algorithm is to measure this asymmetry which carries the information on the polarization of the produced Σ^+ hyperons. The data analysis algorithm consists of two main steps. First, the identification of the Σ^+ signal was performed using the known properties of the Σ^+ hyperon and its decay.[11] At this stage, various selection cuts were applied to the data producing the Σ^+ decay sample for polarization study. At the second stage, the asymmetry in the appropriate angle of the trajectory of the daughter baryon in the identified Σ^+ decays from the previously selected data sample was measured. The value of this asymmetry provided the information on the polarization of the Σ^+ hyperons produced on the primary target.

Stripping Pass: Identifying Decays of Σ^+ Hyperons

To reduce the amount of data to be handled by the main analysis program, an additional data stripping program was written. This program selected only those events from the raw data that potentially could be hyperon two-body decays and wrote those events into strip files to be used on a later stage by the main analysis program. Several selection criteria were imposed by the stripping program. All events selected and written by the stripping program have two essential properties:

[11] See Chapter 3 above for the summary of the relevant properties of Σ^+ hyperon.

they include a track segment of the incoming beam Σ^+ hyperon reconstructed in the SSD detector of the Hyperon Spectrometer and a track segment of the Σ^+ daughter proton reconstructed in the PWC detector of the Baryon Spectrometer. In addition, the Σ^+ hyperon track in the event must form a non-zero kink (decay) angle with the daughter proton track extended upstream of the M2 Analyzing Magnet (AN). In this case the event is considered to be Σ^+ decay candidate. Additional selection criteria used by the stripping program included a relativistic γ-factor selection of the beam particles using the transition radiation detector (TRD) at the exit of the hyperon channel and the requirement of the valid momentum measurement for the beam Σ^+ hyperon in the Hyperon Spectrometer and for the daughter proton in the Baryon Spectrometer. The description below elaborates on the selection criteria used in the stripping of the raw data and provides step-by-step guide to the analysis algorithm. The fractions of the events in the initial data sample rejected by several event selection criteria used by the stripping program described below are summarized in Table 10 and Figure 19.

Fuducial volume of the identified hyperon decays

The $\Sigma^+ \to p\pi^0$ decay was identified as a kink between the Σ^+ track reconstructed in the Hyperon Spectrometer and the track of the Σ^+ daughter proton reconstructed in the Baryon Spectrometer and extended upstream of the M2 Analyzing Magnet. For such a kink to be detected, the track segment of the Σ^+ hyperon must be reconstructed in the Hyperon Spectrometer and the track segment of the daughter must be reconstructed in the Baryon Spectrometer. In addition, to calculate the hyperon mass using 4-momentum conservation the momentum of the hyperon and the daughter must be measured in the Hyperon and Baryon Spectrom-

Criterion	Variable	Limits		Units	Events
		Lower	Upper		[%]
Total unstripped events					100
TRD reading rejection	N_{TRD}	–	5	–	14.6
No reconstructed Σ^+ segment	$--$	–	–	–	8.5
No reconstructed p segment	$--$	–	–	–	12.4
No refined p segment	$--$	–	–	–	6.2
No p segment upstream of AN	$--$	–	–	–	1.8
Good kink events	$--$	–	–	–	2.2
Rejected by residual cuts					54.3
Y kink angle	θ_y	0.05	–	mrad	65.1
Σ^+ and p segments closest approach	dr	0.05	–	cm	11.8
Y kink in M2 Analyzing Magnet	$\theta_{y_{AN}}$	–	$3 \cdot \sigma$	mrad	36.7
Decay angle	θ	0	4	mrad	8.2

Table 10: Criteria used to select candidates for $\Sigma^+ \to p\pi^0$ and $\Sigma^+ \to n\pi^+$ decay events during the stripping pass. Events have been selected by selection criteria in the order shown. A single event could be rejected by one or more residual cuts at the same time.

eters, respectively. A minimal detector set capable of reconstructing the required segments and momenta includes the SSD for reconstructing the hyperon track and determining its momentum, and the LASD2 station, which in conjunction with the LASD3 station and stations A and B of the VDC is used to reconstruct the track of the hyperon decay product and measure its momentum. To be detected, therefore, the decay of a hyperon must occur between the last plane of a SSD of the Hyperon Spectrometer ($z_{SSD} = -15cm$) and the first plane of the LASD2 station

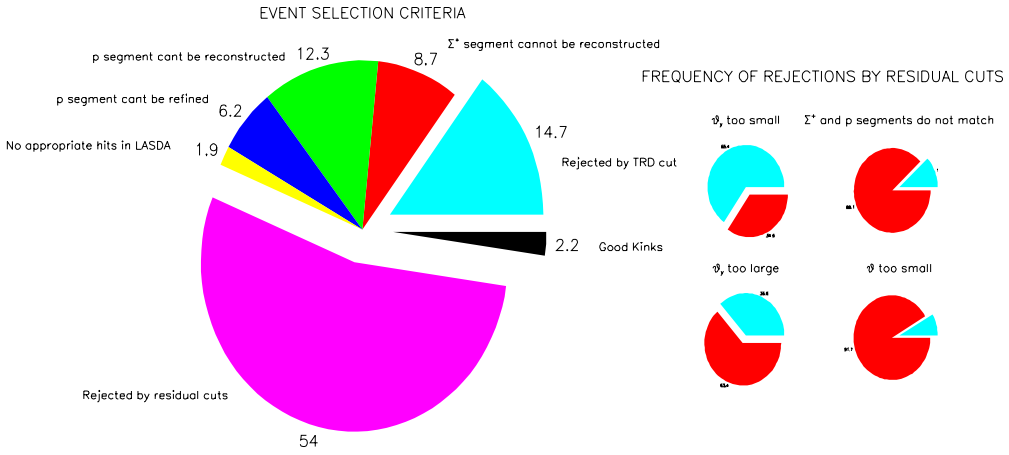

Figure 19: Criteria used to select candidates for $\Sigma^+ \to p\pi^0$ and $\Sigma^+ \to n\pi^+$ decay events during the stripping pass. Events have been selected by selection criteria in the order shown. A single event could be rejected by one ore more residual cuts at the same time.

($z_{LASD2} = 625cm$). This decay region is 6.4 m long.[12,13]

[12]The fraction of the Σ^+ hyperons that decay in this region can be determined in the following way (the position of the hyperon target is $z_{TGT} = -1111cm$, and the 572 GeV/c Σ^+ hyperon travels $l = 11m$, see Chapter 3 above):

$$k = e^{-(z_{HS}-z_{TGT})/l} - e^{-(z_{LASD3}-z_{TGT})/l} = e^{-0.996} - e^{-1.578} = 0.163.$$

According to this calculation, only about 16.3% of all Σ^+ hyperons produced on the hyperon target with momentum 572 GeV/c decay in the designated decay region. For hyperons having momentum of 375 GeV/c and 500 GeV/c this numbers are 12.9% and 15.6%, respectively. Note that in practice the decay region is even smaller because of the z_{kink} cut, see Table 12.

[13]The largest fraction of the Σ^+ that can be reconstructed using the SELEX spectrometer is determined by z coordinates of the most upstream and downstream detectors of suitable resolution. These would probably still be the SSD with $z_{SSD} = -15cm$ and station A of Vector Drift Chambers with $z_{VDCA} = 28m$. Accordingly, the maximum fraction is about 29%. In this case the M3 Spectrometer with its M3 M2 Analyzing Magnet, a set of Λ proportional wire chambers, and the VDC station C has to be used to measure the momentum of the daughter. If the M3 Spectrometer is not used, the most upstream detector would be the LASD2 with $z_{LASD2} = 625cm$ and this fraction drops to 16.3%.

Rejecting light particles with the TRD

Pions in the secondary beam were separated from the heavier particles using the transition radiation detectors (TRD) installed at the exit of the hyperon channel. Heavy hyperons and protons have a relatively low relativistic factor γ as compared to lighter beam particles, such as pions. The TRD detector produces hits with multiplicity proportional to γ of the particles passing through it. The TRD detector was used to reject events with light beam particles by imposing cut on the TRD hit multiplicity (N_{TRD}). Figure 20 shows the TRD multiplicity histograms as a function

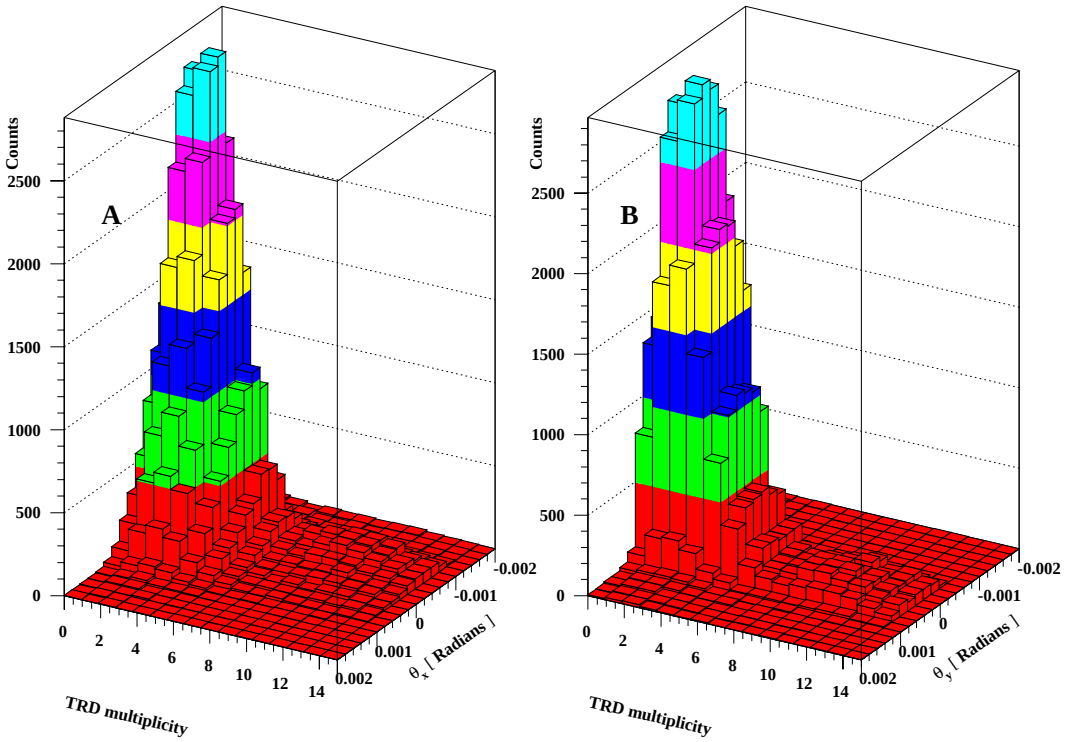

Figure 20: Multiplicity of the hits in the TRD detector N_{TRD} as a function of the particle's angles at the Hyperon Spectrometer. Plot (A) shows the dependence of the N_{TRD} on the angle θ_x of the particle in the X-Z plane and Plot (B) shows the corresponding dependence on the angle θ_y of the particle in the Y-Z plane.

of the beam hyperon angles at the SSD detector. A small number of counts with $N_{TRD} > 5$ corresponds to the pions in the beam, see Figure 20. Accordingly, the

selection cut was made at the TRD multiplicity 5, see Table 10.

Reconstruction of the track segments of the hyperon and its daughter proton

The track segments of the hyperon and the daughter baryon were reconstructed by conventional tracking routines integrated into the Selex Offline Analysis Program (SOAP) environment. The track and the momentum of the Σ^+ hyperon was measured using 8 high resolution planes of the silicon strip detectors of the Hyperon Spectrometer, see Figure 16. Out of these 8 planes, at least 4 were required to be in the fit. A χ^2 cut for the track segment fit was made at $\chi^2 = 4$. A typical plane combination required for the reconstruction of a Σ^+ track segment in the SSD detector would include one or two X–oriented planes, one or two Y–oriented planes and 1 U or V–oriented plane. Similarly, a daughter proton track was initially reconstructed in the proportional wire chambers (PWC) of the Baryon Spectrometer. Out of 14 available planes at least 4 were required to be in the fit. For the daughter proton, the χ^2 of the track fits was required to be less than 2.5. Various plane combinations including all available X, Y, U, and V–oriented planes were used.

The stripping program selected only those events that had at least one track segment in the SSD detectors of the Hyperon Spectrometer and at least one track in the PWC chambers of the Baryon Spectrometer. The presence of these two segments in the event is required for the selection of decayed Σ^+ and for measuring the momentum of the daughter proton. Table 10 shows number of events that were rejected by the foregoing selection criteria.

Reconstructing the track segment of the daughter proton upstream of the M2 Analyzing Magnet

In order to increase the decay region, only one LASD station, upstream of the M2 Analyzing Magnet was used to reconstruct the track of the hyperon decay product upstream of the Baryon Spectrometer.[14] With only one LASD station, there is insufficient information to reliably reconstruct track upstream of the Baryon Spectrometer due to the short distance between LASD planes within single LASD station. Accordingly, in order to extend the track segment of the daughter upstream of the M2 Analyzing Magnet, the reconstructed track segment of the daughter downstream of the Analyzing Magnet and separate hits in the LASD2 station and stations A and B of the VDC were used. The track segment of the daughter upstream of the M2 Analyzing Magnet was reconstructed in the following way. First, the track segment of the daughter originally reconstructed in the PWC chambers downstream of the M2 Analyzing Magnet was extended further downstream and matched to the VDC vector reconstructed in the VDC A and VDC B chambers having the closest intercept coordinate. [15] Similarly, the track segment of the daughter in the PWCs was then projected upstream to find matching hits in the LASD3 station.

The hits found in the LASD3 station and VDC A and B were used to generate new "refined" daughter track segment. After the daughter track segment has been so refined, it was extrapolated upstream to the mid point of the M2 Analyzing Magnet. The software then tried to find hits in the LASD2 station that would

[14]The third, most upstream LASD station of the SELEX apparatus LASD1 was not used in the analysis in order to increase the decay region for the Σ^+ hyperons.

[15]In more detail, the program looped through all vectors for each A and B VDC stations which are stored in the database having their respective coordinates in the center of VDC detectors coordinate system. The program then projected these vectors back to the VDC 6-plane clusters where these hits originated from and found vectors with minimal deviation of the intercept from the coordinate of the projection of the daughter track segment.

match the extrapolated segment of the daughter to form a valid track segment upstream of the M2 Analyzing Magnet. This was done in two steps. First, the program connected all possible X and Y hits in the LASD2 station to the point of the intersection of the downstream refined track segment of the daughter and the mid plane of the Analyzing Magnet to form a set of daughter segment candidates upstream of the magnet, as shown in Figure 21. The second step was the validation

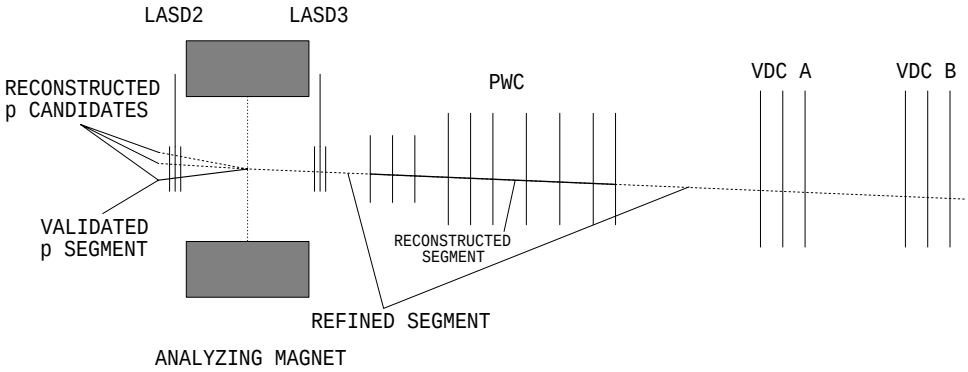

Figure 21: Method for reconstruction track segment of a Σ^+ daughter proton upstream of the M2 Analyzing Magnet.

of the reconstructed upstream segment candidates. For this purpose, at least one additional X and one additional Y hit in the LASD2 station were required to be within the 3 σ distance of the projection of a newly reconstructed upstream track segment of the daughter on the appropriate LASD plane. Validated in such a way upstream daughter track segments were used in a subsequent kink finding.

Kink finding: matching the track segments of the Σ^+ and the daughter

Ideally, the reconstructed tracks of the Σ^+ hyperon and its daughter proton meet at the decay point. In practice because of measurement errors the tracks rarely meet. Thus, one looks for a distance of closest approach of the tracks. A decay point

is established if the closest approach distance is consistent with the measurement error. In the present analysis a point of the closest approach of the Σ^+ hyperon track segment reconstructed in the SSD detector of the Hyperon Spectrometer and the daughter track segment upstream of the M2 Analyzing Magnet defines a potential point of the Σ^+ hyperon decay. To be a valid decay point, it must be within the decay region that starts after the most downstream plane of the SSD detector and continues up to the front of the most upstream plane of the LASD2 station of the Baryon Spectrometer. This decay volume is about 6.4 m long. The hyperon has to travel about 11 m through the Hyperon Magnet and various beam detectors before it enters this decay region. With a momentum of 572 GeV/c the Σ^+ hyperon travels on average about 11 meters before decaying. Therefore, only $1/2.71 = 0.37$ of all Σ^+ hyperons with momentum 572 GeV/c produced on the hyperon production target enter in the designated decay volume.

The distance of the closest approach dr of the Σ^+ hyperon track segment and the daughter track segment has to be less than the value of the corresponding error in the tracking σ_r:

$$dr < 3 \cdot \sigma_r,$$

$$\sigma_r = ((\sigma(\theta_{x_{\Sigma^+}})^2 + \sigma(\theta_{y_{\Sigma^+}})^2)(z_{HS} - z_{kink})^2 + \sigma(x_{\Sigma^+})^2 + \sigma(y_{\Sigma^+})^2 +$$

$$(\sigma(\theta_{x_{cd}})^2 + \sigma(\theta_{y_{cd}})^2)(z_{BS} - z_{kink})^2 + \sigma(x_{cd})^2 + \sigma(y_{cd})^2)^{1/2}.$$

Only the lowest order (in σ) terms were kept. z_{HS} and z_{BS} are the global z-coordinates of the origins of the Hyperon and the Baryon spectrometers, respectively, z_{kink} is the global z coordinate of the Σ^+ decay point, and index cd designates the charged daughter particle. Figure 22 shows distribution of the distance of the closest approach of the reconstructed Σ^+ hyperon track segments and its daughter proton

track segments after a cut on the Y component of the kink angle at $\theta_y > 50$ μrad. [16] This cut was used to separate the primary beam protons, which constitute the major fraction of the secondary positive beam at the exit of the hyperon channel. The cut on the closest approach distance dr was made at dr <500 μm, see Figure 22.

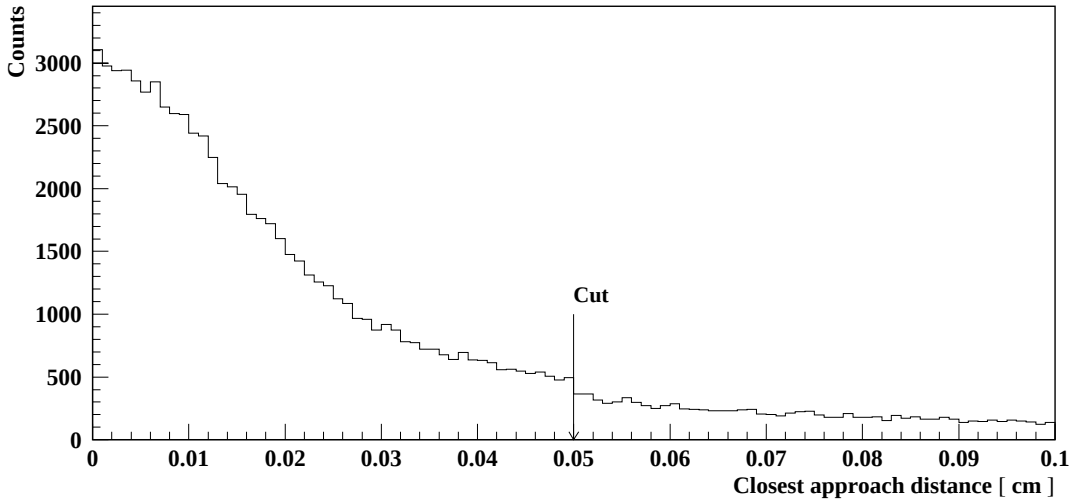

Figure 22: Distribution of the distance of the closest approach of the reconstructed track segments of the Σ^+ hyperon and its charged daughter. The vertex is considered to be a "good" one when the distance of the closest approach is less than 500 μm.

Analysis Pass: Identifying Σ^+ Signal

At this stage of the analysis the signal from the Σ^+ hyperon decays has been identified and separated from the background consisting primarily of scattered protons and decays of other particles. The separation of the Σ^+ signal was accomplished using the $R-\theta$ kinematic plots of the decay and the plots of reconstructed mass of the decaying particle. [17] The observables necessary for separation of the Σ^+ signal

[16] The resolution for the θ_y angle is 20 μrad, see Chapter 4 above.

[17] See below for definition of R and θ variables.

using $R - \theta$ and mass plots include the momenta of the hyperon and its charged daughter, as well as the angle θ that the trajectory of the hyperon's charged daughter forms with the trajectory of the hyperon. This angle will be called here the decay angle.

Measuring the hyperon momentum

It is necessary to know the momentum of the hyperons to calculate the mass of the hyperons and the kinematic parameter R of their decays. The momentum of the Σ^+ was measured using the coordinates of its track segment reconstructed in the SSD detector of the Hyperon Spectrometer, the known coordinates of the hyperon production target, and the value of the magnetic field in the Hyperon Magnet. The assumptions necessary for the momentum reconstruction is that all the hyperons in the beam are produced on the production target and that the production target is infinitesimally small. Figure 23 illustrates the method for reconstructing the Σ^+ hyperon momentum. From this figure it can be seen that the bend angle $\delta\theta_x$ in the Hyperon Magnet of the track of the hyperon originating in the production target and having coordinates x and θ_x measured in the SSD detector can be calculated using the following formula:

$$\delta\theta_x \approx \tan^{-1} \frac{\theta_x(z_{SSD} - z_{TGT}) + (x_{TGT} - x)}{z_{mid}^{eff} - z_{TGT}}.$$

Assuming that the magnetic field is uniform everywhere inside the Hyperon Magnet, the hyperon momentum can be calculated using the following formula:

$$p_{\Sigma^+} = \frac{p_t^{HM}}{\sin \delta\theta_x} \approx \frac{p_t^{HM}}{\tan \delta\theta_x}.$$

Here p_t^{HM} is the value of the transverse momentum kick of the Hyperon Magnet which is perpendicular to the motion direction of a passing particle; p_{Σ^+} is the

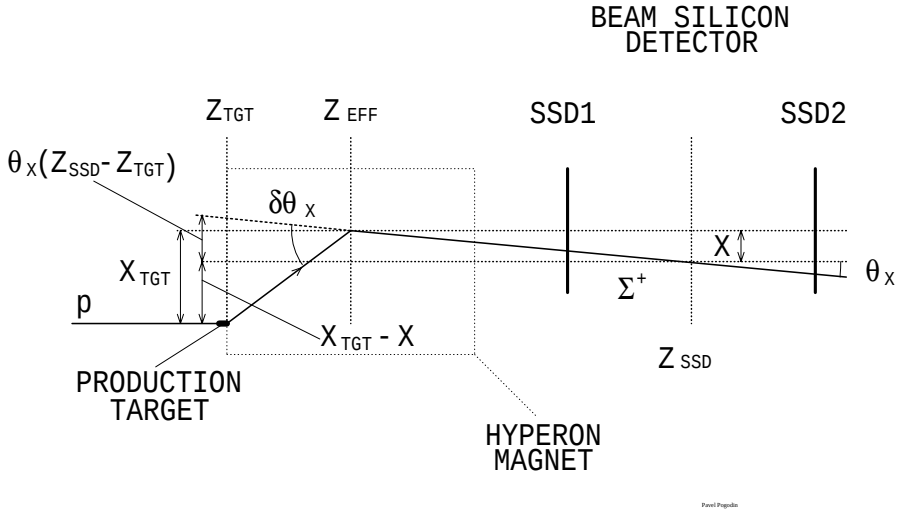

Figure 23: Method for reconstructing the Σ^+ hyperon momentum in the Hyperon Spectrometer.

momentum of the hyperon.[18,19]

[18]If the position of the target is unknown or the existing value is not reliable, one can use the above formulas to determine the x coordinate of the production target using the momentum measurement for non-decaying particle tracks in the Baryon Spectrometer:

$$x_{TGT} = \frac{P_t}{P_p^{M2}}(z_{mid}^{eff} - z_{TGT}) - \theta_x(z_{HS} - z_{TGT}) + x.$$

In this formula all the variables are the same as above, except for the momentum of the beam particle (proton) which now is measured in the Baryon Spectrometer. The mean of the distribution of x_{TGT} values calculated according to this formula would give the correct production target position, see Figure 23.

[19]The error in the momentum measurement is mainly due to the finite width of the production target, which is $1mm$ wide. The value of the uncertainty in the hyperon momentum may be determined by the following formula:

$$\sigma(p_{\Sigma^+}) = \sqrt{(\frac{\partial p}{\partial x_{TGT}}\sigma(x_{TGT}))^2 + (\frac{\partial p}{\partial x}\sigma(x))^2 + (\frac{\partial p}{\partial \theta_x}\sigma(\theta_x))^2}.$$

$$\frac{\Delta p_\Sigma^+}{p_\Sigma^+} = \sqrt{\frac{\sigma(x)^2 + \sigma(x_{TGT})^2 + \sigma(\theta_x)^2(z_{HS} - z_{TGT})^2}{(\theta_x(z_{HS} - z_{TGT}) + (x_{TGT} - x))^2}}.$$

Measuring the momentum of the daughter particle

The Baryon Spectrometer of the apparatus was used to find the momentum of the charged daughter particle produced in the Σ^+ decay (p of the $\Sigma^+ \to p\pi^0$ decay mode and π^+ of $\Sigma^+ \to n\pi^+$). The value of the p_t^{AM}-kick of the Analyzing Magnet of the Baryon Spectrometer has been accurately measured. The momentum of the charged decay product can be calculated similarly to the beam momentum:

$$p_p^B = \frac{p_t^{AM}}{\sin \delta\theta_x^{BS}} \approx \frac{p_t^{AM}}{\tan \delta\theta_x^{BS}} \approx \frac{p_t^{AM}}{\delta\theta_x^{BS}}.$$

Here $\delta\theta_x^{BS}$ is the angle between the projections on the X-Z plane of the daughter particle track segments upstream and downstream of the M2 Analyzing Magnet. [20]

Calibrating the momentum measurements

The p_t-kicks for all magnets of the SELEX apparatus have been measured using a Ziptrack machine for a set of different values of the electric current flowing through the magnets, see Ref. [14]. These values are contained in the database. To obtain a p_t-kick value corresponding to a given current, the value of the p_t-kick corresponding to the closest current value is scaled proportionally to the reading of the Hall probes mounted on the magnets. This procedure, however, did not give

If the only error taken into account is the $\sigma(x_{TGT})$, the relative uncertainty in the hyperon momentum is:

$$\frac{\Delta p_\Sigma^+}{p_\Sigma^+} = \frac{\sigma(x_{TGT})}{\sqrt{12} \cdot x_{TGT}} \approx 0.6\%.$$

This error, along with the actual variation in the beam momentum due to the finite width of the hyperon channel contributes to the width of the observed momentum distribution, see Figure 23.

[20] The uncertainty in the value of the momentum measured in this way is determined by the uncertainties in $\sigma(\theta_x^{BS})$:

$$\frac{\Delta p}{p^{BS}} = \sqrt{\frac{\sigma(\theta_x^{BSUS})^2 + \sigma(\theta_x^{BSDS})^2}{(\delta\theta_x^{BS})^2}}.$$

$\sigma(\theta_x^{BSUS})^2$ and $\sigma(\theta_x^{BSDS})^2$ stand for the errors in the measurements of the slope of the daughter track segment upstream and downstream of the M2 Analyzing Magnet, respectively.

sufficiently accurate p_t-kick values for the magnets to provide the best possible mass resolution for the Σ^+ decays. The resolution of the Σ^+ hyperon mass calculated using $\Sigma^+ \to p\pi^0$ decay is sensitive to the systematic difference in the momentum measurements in the Hyperon Spectrometer and the Baryon Spectrometer. To eliminate this systematic differences, the values of the p_t-kicks in these two magnets need to be adjusted so that both the Hyperon Spectrometer and the Baryon Spectrometer give systematically equal momentum reading for straight tracks of non-decaying protons. This operation was performed during the alignment stage of the analysis. The p_t of the M2 Analyzing Magnet was scaled in such a way that the two spectrometers produce systematically equal momentum measurements for non-decaying particles.

Selecting Σ^+ decays using the $R - \theta$ plot

The decay (kink) angle θ can be calculated using the values of $\theta_x(\Sigma^+)$, $\theta_y(\Sigma^+)$, $\theta_x(D)$, $\theta_y(D)$ – the x and y slopes of the track segments of the Σ^+ hyperon and its charged daughter particle, respectively:

$$\theta = \sqrt{(\theta_x(\Sigma^+) - \theta_x(D))^2 + (\theta_y(\Sigma^+) - \theta_y(D))^2}.$$

The scatter-plots of the decay angle θ as a function of the ratio R of the charged daughter momentum to the Σ^+ momentum are shown in Figure 24 for 572 GeV/c Σ^+ hyperons.

Because the charged daughter particle is produced in the two-body decay of the Σ^+ hyperon, the decay angle θ and the ratio R are not independent of each other, but related through the 4-momentum conservation, see Chapter 3 above for details. Figure 24 shows areas where (R, θ) pairs corresponding to the two primary decay modes of the Σ^+ hyperons fall. Points near $R = 1$ and $\theta = 0$ correspond to the

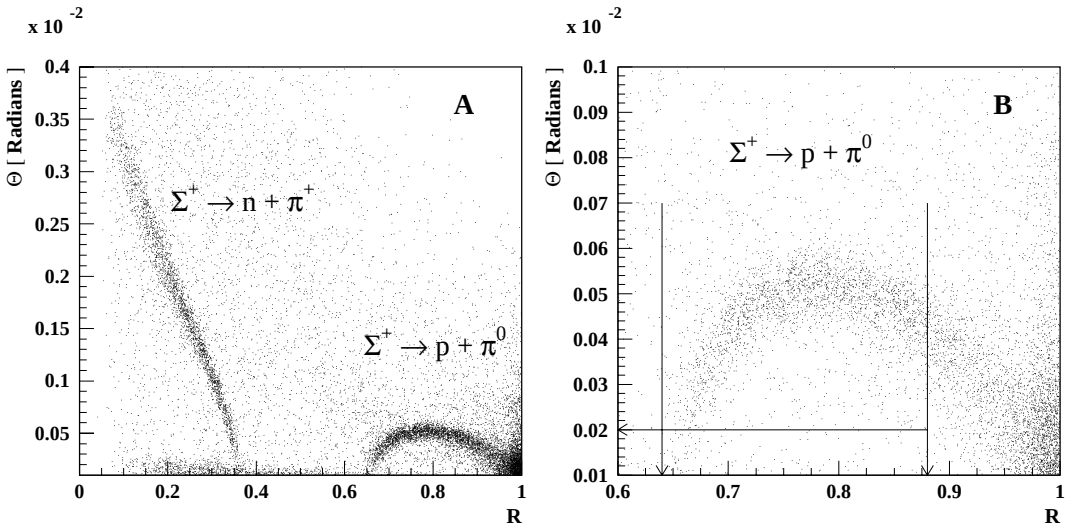

Figure 24: R vs. θ kinematic plot of the Σ^+ decay modes. Plot (A) shows both $\Sigma^+ \to p\pi^0$ and $\Sigma^+ \to n\pi^+$ decays modes. Plot (B) provides a closer view of the $\Sigma^+ \to p\pi^0$ region.

elastically scattered protons. Such events were eliminated from the consideration by imposing cuts on R and θ. An event was selected as a $\Sigma^+ \to p\pi^0$ decay candidate, if $0.64 < R < 0.88$ and $\theta > 200\mu$rad.

Distributions of the Σ^+ hyperon momentum measured in the Hyperon Spectrometer are shown in Figure 25. These distributions are fit with gaussian.

Reconstructing the mass of the Σ^+ hyperon

The Σ^+ mass was calculated from the 4-momentum conservation that relates the 4-momenta of the Σ^+ hyperon and its two daughter particles:

$$P_{\Sigma^+} = P_0 + P_+,$$

where $P_{\Sigma^+} = (\vec{p}_{\Sigma^+}, E_{\Sigma^+})$ is the 4-momentum of the hyperon, $P_0 = (\vec{p}_0, E_0)$ is the 4-momentum of the neutral daughter particle and $P_+ = (\vec{p}_+, E_+)$ is the 4-momentum of the Σ^+ charged daughter particle. The above equation is valid for every compo-

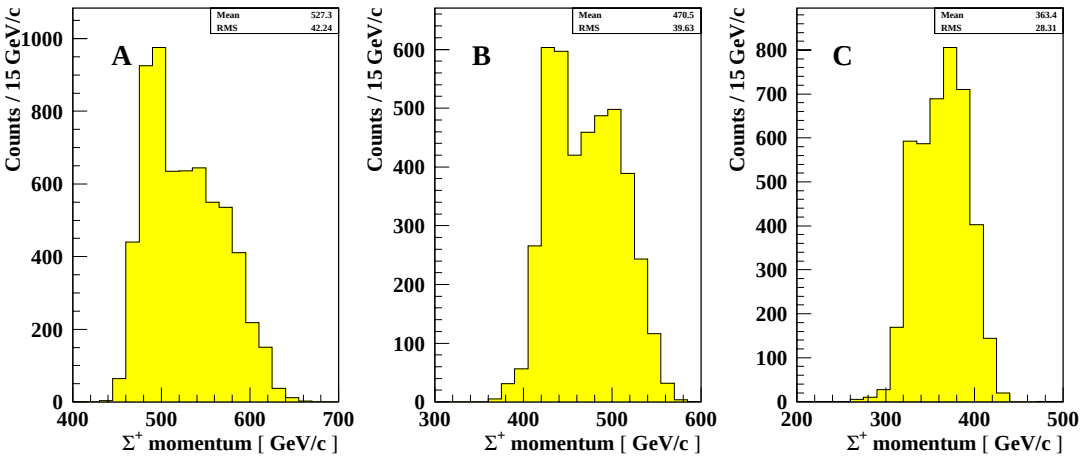

Figure 25: Fits to the Σ^+ hyperon momentum distributions. The Σ^+ momentum was measured in the Hyperon Spectrometer. Plot (A) corresponds to nominal Σ^+ momentum of 572 GeV/c, Plot (B) to nominal momentum of 500 GeV/c, and Plot (C) to nominal momentum of 375 GeV/c.

nent of the 4-momentum.

The momentum of the neutral daughter particle may be obtained from the conservation of 3-momentum – the first 3 components of the 4-momentum vector:

$$\vec{p}_0 = \vec{p}_{\Sigma^+} - \vec{p}_+.$$

In order to calculate the total energy of the neutral daughter particle, it is necessary to make an assumption about its mass:

$$E_0 = \sqrt{m_0^2 + |\vec{p}_0|^2}.$$

The total energy of the Σ^+ can be calculated using conservation of the fourth component of the 4-momentum vector:

$$E_{\Sigma^+} = E_0 + E_+.$$

The mass of the decaying hyperon is calculated using the relation among m_{Σ^+}, p_{Σ^+}

and E_{Σ^+}:

$$m_{\Sigma^+} = \sqrt{E^2_{\Sigma^+} - |\vec{p}_{\Sigma^+}|^2}.$$

When the above formulas are applied to the $\Sigma^+ \to p\pi^0$ decay, π^0 is used as a neutral daughter particle, whereas in case of the $\Sigma^+ \to n\pi^+$ decay the neutral daughter particle is n. Figure 26 shows the mass distribution plots for both primary decay

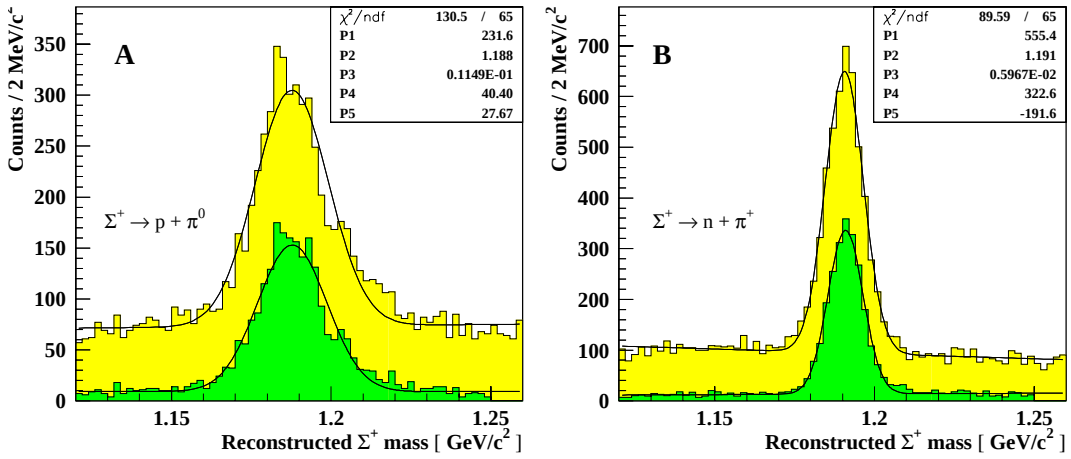

Figure 26: Σ^+ mass distributions calculated from the $\Sigma^+ \to p\pi^0$ decay (Plot (A)) and $\Sigma^+ \to n\pi^+$ decay (Plot (B)) (upper histograms). The lower histograms corresponds to the same mass distributions, but after selection cuts were imposed. Fit parameters P2 and P3 represent the center and the width of the Gaussian fit to the Σ^+ mass distribution, respectively.

modes of the Σ^+ hyperon. The Σ^+ mass distribution for the $\Sigma^+ \to p\pi^0$ decay has width of about 10 MeV/c^2 and centers at 1.189 GeV/c^2. Corresponding histogram for the $\Sigma^+ \to p\pi^0$ decay has width of only 5 MeV/c^2, mainly because the kink angles for this mode are larger, due to a lighter charged decay product, see the $R - \theta$ plot, Figure 24. Σ^+ hyperons were selected by making a cut $1.154 \leq m_{\Sigma^+} \leq 1.224$ on the above mass plots, see Table 11 and Figure 26. The top histograms in Figure 26 correspond to the mass peak before the analysis cuts (Σ^+ mass distribution of all

stripped events). Corresponding bottom histograms show the mass plots after the analysis cuts listed in Table 11 were imposed. It can be seen that 10% background remains under the $\Sigma^+ \to p\pi^0$ mass peak even after imposition of the analysis cuts.

It was assumed that the events in the tails of the mass peak have the distribution of various parameters (Z of the decay, asymmetries, etc.) identical to the events in the background under the mass peak. This assumption was used to "subtract" the background under the mass peak from all the studied distributions. For instance, the average distribution of the Z coordinate of the decay for the events in two 70 MeV/c^2-wide regions to the left and to the right of the mass peak (1.084 GeV/c^2 $\leq m_{\Sigma^+} \leq$ 1.154 GeV/c^2 and 1.224 GeV/c^2 $\leq m_{\Sigma^+} \leq$ 1.294 GeV/c^2) was subtracted bin-by-bin from the Z of the decay distribution of the events in the 70 MeV/c^2-wide selected mass window (1.154 GeV/c^2 $\leq m_{\Sigma^+} \leq$ 1.224 GeV/c^2). This procedure permitted to "eliminate" the influence of the background under the mass peak on the studied angular distributions.

Σ^+ rates

The predicted Σ^+ fraction for the beam momentum 572 GeV/c and P_t = 1.5 GeV/c is $\approx$2% of the beam at 10 m from the production target [17, 21].[21] The number of reconstructed Σ^+ decays can be measured by fitting the Σ^+ mass peak with a gaussian interposed on some function (usually 1st order polynomial) fitting the background and calculating the area under the gaussian. For 572 GeV/c Σ^+ momentum the number of reconstructed Σ^+ decays (both primary decay modes) estimated using this method is 2,217 per million triggers. The decay region limitation dictates that only 43 % of the Σ^+ at 10 m from the production target decay in the

[21] Note that the present measurement was done for different P_t and X_f, therefore this number should be taken with a caution.

dedicated volume. Therefore the reconstruction rate is 5,156 per million triggers, or 0.52%. Accordingly, the efficiency of the reconstruction is about 26%. The primary sources of the inefficiency in the reconstruction are the inefficiencies of the apparatus and the analysis, as well as the affect of the θ_y cut used to reduce the proton background, see Tables 10 and 11.[22]

Σ^+ mass resolution

The resolution of the reconstructed Σ^+ mass depends on the resolution of the measurement of the hyperon momentum and the momentum of the hyperon's daughter particle as well as the error in the decay angle θ.

The multiple scattering contribution can be calculated using the following formula, see ref. [19]:

$$\theta_{rms} = \frac{13.6 MeV/c}{p} z\sqrt{x/X_0}[1 + 0.038\ln(x/X_0)].$$

the total radiation length is $x/X_0 = 0.1242(\text{Upstream of } BS)+0.069(BS)+0.1(air) = 0.29$. Where the first term represents contribution of the material in the beam path upstream of the Baryon Spectrometer, the second term represents the contribution of the material in the Baryon Spectrometer, and the last term represents the contribution of the air. For a 400 GeV/c particle the multiple scattering contribution to the error in x and y coordinates at the VDC A can be calculated as follows[23]:

$$y_{rms} = z{\cdot}\theta_{rms}/\sqrt{3} = 30m{\cdot}\frac{13.6\ MeV/c}{400,000\ MeV/c}{\cdot}1{\cdot}\sqrt{0.29}[1{+}0.038\ln(0.29)]/\sqrt{3} = 0.3mm$$

Measurements of the Polarization of the Σ^+ Hyperon

The polarization of Σ^+ hyperons produced on the primary target was measured using events of the $\Sigma^+ \to p\pi^0$ decay. Both arithmetic and geometric mean

[22] See Chapter 6 below for the value of the simulated reconstruction efficiency.
[23] The average momentum of the daughter proton is close to 400 GeV/c.

bias cancelling methods described in Chapter 3 above were used. The result was subsequently verified against the $\Sigma^+ \to n\pi^+$ data. Finally, the behavior of false asymmetries was investigated.

Selecting $\Sigma^+ \to p\pi^0$ decay sample for polarization measurement

The α factor corresponding to $\Sigma^+ \to p\pi^0$ decay mode is about 14 times greater than of the $\Sigma^+ \to n\pi^+$ decay. Therefore, the decay asymmetry in the first decay mode must be 14 times greater and determination of polarization using this decay requires 14^2 times lesser statistics in order to provide comparable accuracy with the $\Sigma^+ \to n\pi^+$ mode, see Chapter 3 above for details. On the other hand, the region on the $R-\theta$ plot where the daughter protons from the $\Sigma^+ \to p\pi^0$ decay lie is at the high R and low kink angle θ. For this reason, the background from the elastically scattered protons is hard to separate and eliminate. Table 11 summarizes the cuts used to select sample of $\Sigma^+ \to p\pi^0$ and $\Sigma^+ \to n\pi^+$ events for polarization measurement during the analysis pass. For instance, the Z of the kink cut, 80 cm$<$ z_{kink} $<$610 cm, removed most of the background lying under the $\Sigma^+ \to p\pi^0$ curve on the $R-\theta$ plot. In order to further eliminate the background due to the elastically scattered protons, an R cut $0.64 < R < 0.88$ was made. The kink angle cut $\theta > 150$ μrad and the Y kink angle cut $\theta_y > 50$ μrad were introduced in order to eliminate small kink angle particles which lie below Σ^+ on the $R-\theta$ plot. Finally, the mass cut was made at 1.154 GeV/c^2 $< m_{\Sigma^+} <$1.224 GeV/c^2 to select well measured $\Sigma^+ \to p\pi^0$ decays. Table 11 also lists all other cuts used in selecting $\Sigma^+ \to p\pi^0$ events for polarization measurement. The hyperon decay reconstruction yields after these cuts were made are also shown in Table 11.

Variable name	Variable	Limits		Units	Rejected Σ^+ [%]
		Lower	Upper		
$\Sigma^+ \to p\pi^0$ decay sample					
Kink angle	θ	0.15	–	mrad	3.6
Y Kink angle	θ_y	0.05	–	mrad	0
R	R	0.64	0.88		0.2
Σ^+ mass	m_{Σ^+}	1.154	1.224	GeV/c^2	4.2
Z-coordinate of the kink	z_{kink}	80	610	cm	29.3
Phase space of the beam	P_{beam}	$73.33 \cdot x + 503.33$	–	GeV/c	1.0
χ^2 of the p segment	χ^2	–		–	13.4
Total $\Sigma^+ \to p\pi^0$ decays after cuts					55.3
Total $\Sigma^+ \to p\pi^0$ decays before cuts					100
$\Sigma^+ \to n\pi^+$ decay sample					
Kink angle	θ	0.3	–	mrad	0.7
Y Kink angle	θ_y	0.05	–	mrad	0
r parameter	r	0.1	0.4		0.8
Σ^+ mass	m_{Σ^+}	1.154	1.224	GeV/c^2	2.5
Z-coordinate of the kink	z_{kink}	80	610	cm	26.2
Total $\Sigma^+ \to n\pi^+$ decays after cuts					69.8
Total $\Sigma^+ \to n\pi^+$ decays before cuts					100

Table 11: Cuts used to select sample of $\Sigma^+ \to p\pi^0$ and $\Sigma^+ \to n\pi^+$ events for polarization measurement during the analysis pass.

Reality check: length of Σ^+ decays in the final data sample

Plotting decay lengths of the Σ^+ hyperon in the final data sample selected for the polarization measurement helps to verify that selected by the stripping and analysis cuts particles are indeed Σ^+ hyperons. In addition, the Z distribution of the decays shows whether the reconstruction efficiency is uniform with Z. It also helps to study the Z distribution of the background kinks. Figure 27 shows a fit of the Z distribution of the kinks in the decay region with the function $p1 \cdot e^{-(z+1111cm)/p2}$ for one of the data sets taken. The background under the Z distribution has been subtracted using tails of the mass peak, as described above.

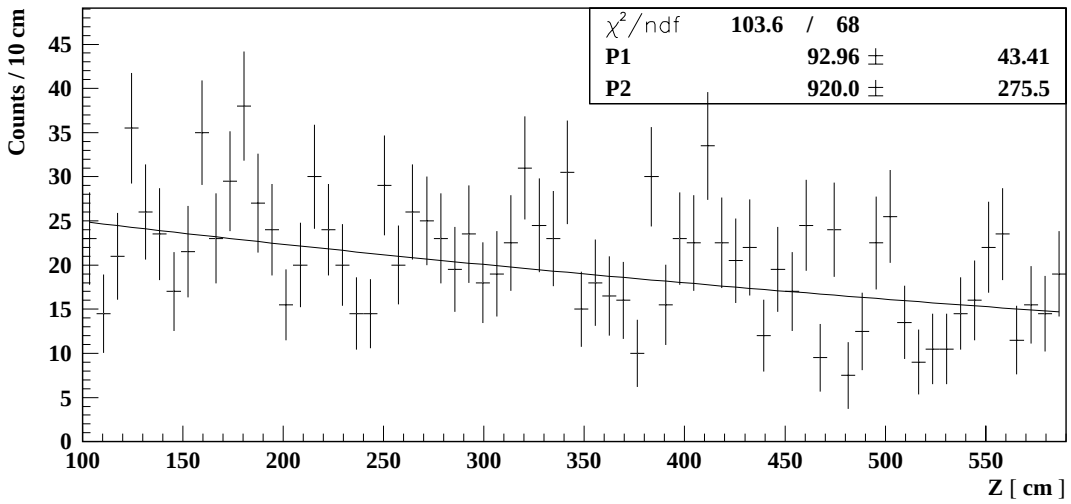

Figure 27: Fit of the Z distribution of the kinks. The fit was made with the function $p1 \cdot e^{-(z+1111cm)/p2}$ for all data sets taken. The value of parameter p2 corresponds to the decay length of Σ^+ hyperon.

Figure 28 shows summary plots for Σ^+ hyperon decay lengths fitted as shown in Figure 27 for all data sets taken. Expected decay lengths are shown with solid lines. Plot (A) corresponds to Σ^+ momentum 572 GeV/c, Plot (B) to 500 GeV/c, and Plot (C) to 375 GeV/c. The decay lengths obtained from the data are very close (well within the σ of the statistical error) to what is expected. This demonstrates that the reconstruction efficiency is probably uniform with Z and that the background in the final data sample is small.

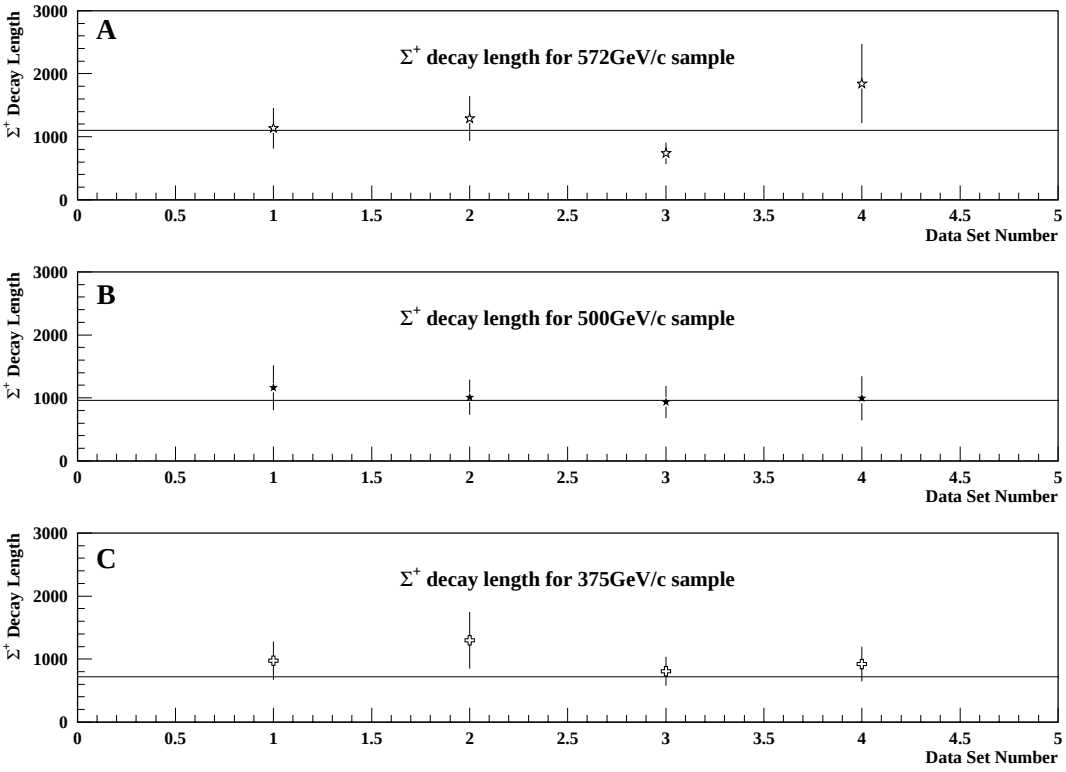

Figure 28: Summary plots showing Σ^+ hyperon decay lengths in the final data sample. The plotted decay length values were determined according to the kink Z distribution fits shown in Figure 27 for all data sets taken (the background under Z distributions has been subtracted using tails of the mass peak). Expected decay lengths are shown with solid horizontal lines. Plot (A) corresponds to Σ^+ momentum 572 GeV/c, Plot (B) to 500 GeV/c, and Plot (C) to 375 GeV/c.

Phase space of the beam at different targeting angles

Figure 29 shows the beam phase space, i.e. plots representing the x_{Σ^+} vs. $\theta_{x\Sigma^+}$, y_{Σ^+} vs. $\theta_{y\Sigma^+}$, and p_{Σ^+} vs. x_{Σ^+} of the beam hyperons from the data samples corresponding to the ± 4 mrad targeting angles. As can be seen, the regions of the phase space occupied by the $+4$ mrad and -4 mrad components partially overlap. In order to provide an accurate measurement of polarization, one only should select phase space regions where both components are present. For the p_{Σ^+} vs. x_{Σ^+} phase

space plot this region of the overlap is above the line representing the phase space cut shown in Figure 29. The events lying below the line were rejected by this cut. Even better accuracy can be achieved by subdividing the phase space into box-

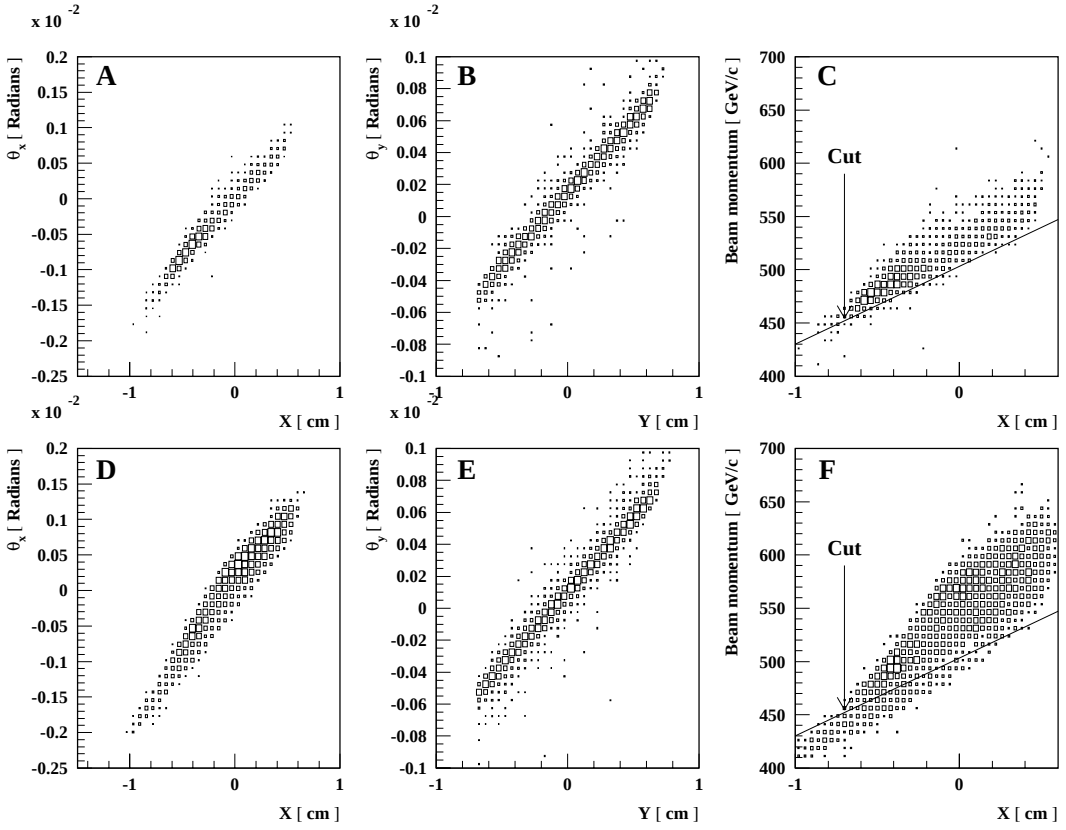

Figure 29: The phase space locations of the beam components with +4 mrad and −4 mrad targeting angles and beam momentum 572 GeV/c. Both beams were produced on Be target. Plots (A-C) correspond to +4 mrad primary beam targeting angle, Plots (D-F) to −4 mrad. Plots (A) and (D) show x_{Σ^+} vs. $\theta_{x\Sigma^+}$ distributions, Plots (B) and (E) show y_{Σ^+} vs. $\theta_{y\Sigma^+}$ distributions, and Plots (C) and (F) show p_{Σ^+} vs. x_{Σ^+} distributions. See Figure 43 presented in Appendix A for corresponding distributions for Cu production target.

shaped areas, see Chapter 6 below, and calculating the polarization for each area separately. As the average momentum of the particles in different areas may vary, the polarization need not be the same for all of them.

Calculating the CM parameters of the decay

Once the event samples corresponding to the complementary primary beam targeting angles are selected as outlined above, the quantities describing the decay in the hyperon center of mass frame can be calculated according to the formulas of the Chapter 3 above using the parameters of the track segments of the hyperon and its daughter. The cosine of the angle that the hyperon's daughter proton track forms (in the Σ^+ CM frame) with the vertical (Y) axis is given by the formula:

$$\cos\Theta_Y = \theta_y \cdot \frac{p_B}{p_{CM}},$$

The corresponding relations for $\cos\Theta_X$ and $\cos\Theta_Z$ components can be found in Section 4 of Chapter 3 above. In this formula p_B is the momentum of the baryon in the lab frame and p_{CM} is the momentum of the baryon in the Σ^+ center-of-mass frame. This momentum is calculated using energy conservation. Its value is given by the following formula, see Chapter 3 above:

$$p_{CM} = \frac{1}{2}\frac{\sqrt{(m^2_{\Sigma^+} - (m_B - m_\pi)^2)(m^2_{\Sigma^+} - (m_B + m_\pi)^2)}}{m_{\Sigma^+}}$$

For the $\Sigma^+ \to p\pi^0$ decay mode $p_{CM} = 0.189\ GeV/c$ and for the $\Sigma^+ \to n\pi^+$ decay mode $p_{CM} = 0.185\ GeV/c$.

Calculation of the asymmetry

parameter and polarization

Histograms showing the number of selected $\Sigma^+ \to p\pi^0$ decays verses cosines of the angles Θ_x, Θ_y, and Θ_z are presented in the Figure 30. This figure shows the data corresponding to the Σ^+ momentum 572 GeV/c and both targeting angles of $+4$ mrad and -4 mrad and the sum thereof. The central region of these graphs corresponds to the small kink angles and has been affected by the θ and θ_y cuts,

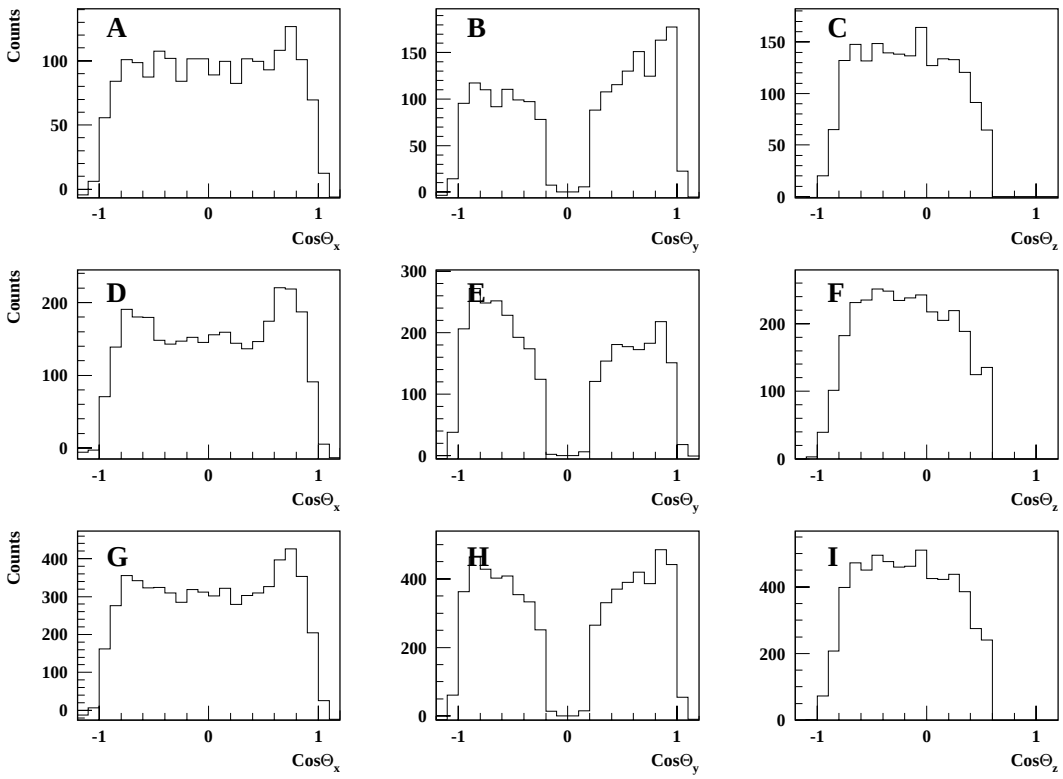

Figure 30: Distribution of the cosines of the X, Y, and Z components of the Σ^+ decay angle (proton angle) $\cos\Theta$. The distribution was calculated in the center of mass of the decay system (for 572 GeV/c hyperons produced on Be target). Plots (A)-(C) correspond to +4mrad targeting angle, Plots (D)-(F) to −4mrad targeting angle, and Plots (G)-(I) to the sum of both +4mrad and −4mrad components.

see Table 11. At this point only statistical errors were taken into account. They are equal to $\sqrt{N_i^{\pm}}$ for the i-th bin. These values of the statistical error for each bin are used in the subsequent error propagation to obtain the value of the statistical error in the final polarization answer. The bottom plots in Figure 30 show the acceptance of the apparatus functions, which is just a normalized sum of the $\cos\Theta$ distributions for each of the three components of the decay angle. Note that the acceptance functions corresponding to $\cos\Theta_x$ and $\cos\Theta_y$ are symmetric with respect

to zero.[24] This may be taken as an evidence of the absence of an angular biases in the system.

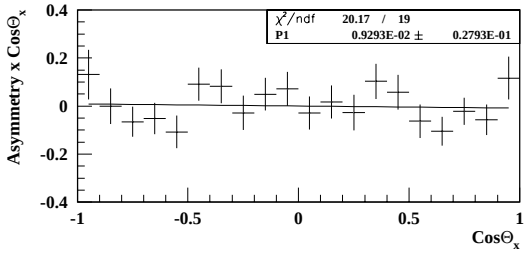

Figure 31: Asymmetries with respect to the cosines of the Σ^+ decay angles (proton angle) $\cos\Theta_x$, $\cos\Theta_y$, and $\cos\Theta_z$ in the center of mass frame of the decaying hyperon. Shown distributions correspond to Σ^+ hyperons with momentum 572 GeV/c produced on Be target. Plots (A), (C) and (E) show the asymmetries calculated using method of arithmetic mean. Plots (B), (D) and (F) show the corresponding asymmetries calculated using method of geometric mean.

Figure 31 shows the asymmetry plots corresponding to these angular event distributions determined in accordance with the bias cancelling techniques of Section 2 of Chapter 3 above. The P1 parameter of the fits represents the magnitude of the polarization vector. The left plots in this figure (Plots (A), (C), and (E))

[24] The acceptance function corresponding to Θ_z was affected by R cut that rejects particles with values of $\cos\Theta_z$ near 1. This causes the observed asymmetry in the distribution of $\cos\Theta_z$.

contain the asymmetries calculated using the method of arithmetic mean. The same asymmetries calculated using the geometric mean method are shown in the right plots of the figure (Plots (B), (D), and (F)). For both bias cancelling methods the values of the polarization are equal with up to 10^{-3} accuracy. Similar plots for the remaining 5 data sets are shown in the Appendix A.

False asymmetries

Because the targeting of the primary beam on the production target is done in the horizontal X-Z plane, there is no non-zero targeting angle in vertical plane. The polarization vector of a hyperon produced on the hyperon production target must point along Y axis.[25] Note that the magnetic field in the Hyperon Magnet and in all other magnets of the apparatus also points in the Y direction and therefore the spin vector of hyperons does not precess in the magnetic field. Accordingly, a polarization vector at the decay point of a hyperon also points vertically and the angular distribution of the baryon in formula (3) of Chapter 3 depends only on the cosine of the Y component of the kink angle $\cos\Theta_y$ and does not depend on the cosines of components $\cos\Theta_x$ and $\cos\Theta_z$. Therefore, there should be no asymmetry with respect to the latter two angles, unless there is X or Z component of the magnetic field which causes the spin precession, or there is a small targeting angle in the vertical plane. The presence of an asymmetry with respect to $\cos\Theta_x$ and $\cos\Theta_z$ kink angle components may indicate that the system has an angular bias and the asymmetry with respect to $\cos\Theta_y$ is measured incorrectly. The $dN^+/d\cos\Theta$ and $dN^-/d\cos\Theta$ distributions of daughter protons from $\Sigma^+ \to p\pi^0$ decay are presented in Figure 30 for angles Θ_x, Θ_y, and Θ_z for a beam momentum of 572 GeV/c. Figure 32 summarizes the values of false asymmetries with respect to $\cos\Theta_x$, $\cos\Theta_z$

[25] See Chapter 3 above.

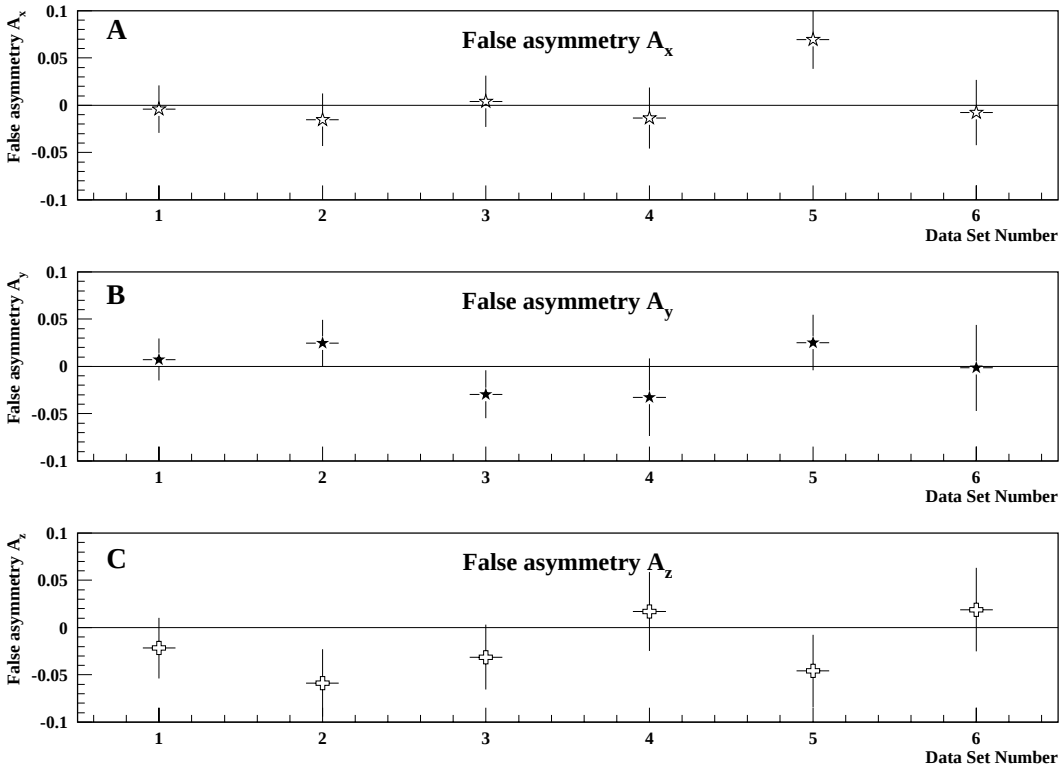

Figure 32: False asymmetries. Plots (A) and (C) show asymmetries of $\Sigma^+ \to p\pi^0$ decays with respect to $\cos\Theta_x$ and $\cos\Theta_z$. Plot (B) shows asymmetry of $\Sigma^+ \to n\pi^+$ decays with respect to $\cos\Theta_y$.

for $\Sigma^+ \to p\pi^0$ decay, and also $\cos\Theta_y$ of $\Sigma^+ \to n\pi^+$ decay (see the next section). The false asymmetry distributions for those angles are consistent with zero.

$\Sigma^+ \to n\pi^+$ decay sample

The small value of α parameter, $\alpha = 0.068$ makes the observable asymmetry in $\Sigma^+ \to n\pi^+$ decay 14 times smaller than in $\Sigma^+ \to p\pi^0$ decay. Assuming that the value of absolute error in the measured asymmetry is the same (this error is determined primarily by the angular resolutions of the spectrometers) as that of $\Sigma^+ \to n\pi^+$ decay, the relative error in the polarization value calculated from the formula $P = A/\alpha$ will be proportionally higher for the $\Sigma^+ \to n\pi^+$ decay and 14^2

more events will be required to achieve the same level of precision. On the other hand, since the observable asymmetries in the $\Sigma^+ \to n\pi^+$ decay are very small, this data may be used in systematic studies to test the biases of the experimental apparatus and the analysis software. Accordingly, the $\Sigma^+ \to n\pi^+$ data was analyzed to verify the polarization measurement using the $\Sigma^+ \to p\pi^0$ decay and to detect potential angular biases in the system.

Selection of the $\Sigma^+ \to n\pi^+$ decay events

The $\Sigma^+ \to n\pi^+$ events are well separated in the $R-\theta$ plot from the potential background decays, see Figure 24. The mass peak for this decay is also exceptionally clean and has width of about 5.3 Mev, see Figure 26. Therefore, the mass cut was made at 1.154 GeV/c^2 $< m_{\Sigma^+} <$ 1.224 GeV/c^2. Other cuts performed on the $\Sigma^+ \to n\pi^+$ event sample are presented in Table 11 and are similar to the cuts used in selection of $\Sigma^+ \to p\pi^0$ events. Note that because the $\Sigma^+ \to n\pi^+$ signal was very clean(see the mass plots in Figure 26), no phase space cut was performed on the data.

Calculation of the asymmetry parameter and polarization

Asymmetry and polarization values were calculated for the $\Sigma^+ \to n\pi^+$ decays in the similar way as for the $\Sigma^+ \to p\pi^0$ decays. Because the asymmetry parameter α in formula (2) of Chapter 3 is only 0.068, one should not observe significant angular asymmetries A of $\Sigma^+ \to n\pi^+$ decays. Values of the asymmetry A for the $\Sigma^+ \to n\pi^+$ decays with respect to $\cos\Theta_y$ are shown in Figure 32, Plot (B). Note that all the asymmetry values for the $\Sigma^+ \to n\pi^+$ decays are consistent with zero, as expected.

CHAPTER VI

EMBEDDING AND SYSTEMATIC ERROR STUDIES

This section describes the treatment of the systematic uncertainty in the measured polarization value. Systematic uncertainty is present in the measurement result when it deviates from the "correct value" due to factors other than a statistical fluctuation. Both the apparatus and the data analysis algorithm may contribute to the systematic error in the measured polarization value. All possible contributions to the systematic error will be analyzed below and the conservative upper bound on the systematic error will be calculated. The data analysis algorithm used to measure the polarization consists of two main steps – identification of the Σ^+ signal and the calculation of the asymmetries[26]. Both these steps may contribute to the systematic error in the polarization. Respective contributions of both these steps will be analyzed.

Results of the Monte-Carlo Simulation

To test potential systematic uncertainties due to the properties of the experimental apparatus and the data analysis algorithm we used Monte-Carlo generated Σ^+ decays that were embedded into the data. The Monte-Carlo events were generated with a predetermined -20% value for the Σ^+ hyperon polarization. For each decay event the decay angles, as well as the daughter particles momenta were simulated in the center of mass system of the decay. So obtained decay angles in the rest frame of the decaying Σ^+ hyperon were then converted to the decay angles in the laboratory coordinate frame. The Σ^+ track was then rotated and translated to coincide with a beam track from the real data. This permitted one to create a sample

[26]See the detailed explanations of the data analysis algorithm in Chapter 4.

of Monte-Carlo generated Σ^+ decays with Σ^+ hyperons having a phase space distribution of the real beam Σ^+ hyperons. Obtained in this way Monte-Carlo generated tracks were then used to simulate hits for every detector plane of the apparatus. Coordinate smearing due to the multiple scattering was taken into account. Subsequently, the original track reconstruction program was run on the simulated hits. Monte-Carlo generated data were then analyzed by the data analysis program in the same way and using the same selection cuts as the real data.

Reconstruction of Kinematic Variables and Σ^+ Mass

Figures 33 and 34 show the $R-\theta$ kinematic plots and Σ^+ mass distribution calculated using the real data [27] and the embedded events. The Σ^+ mass distri-

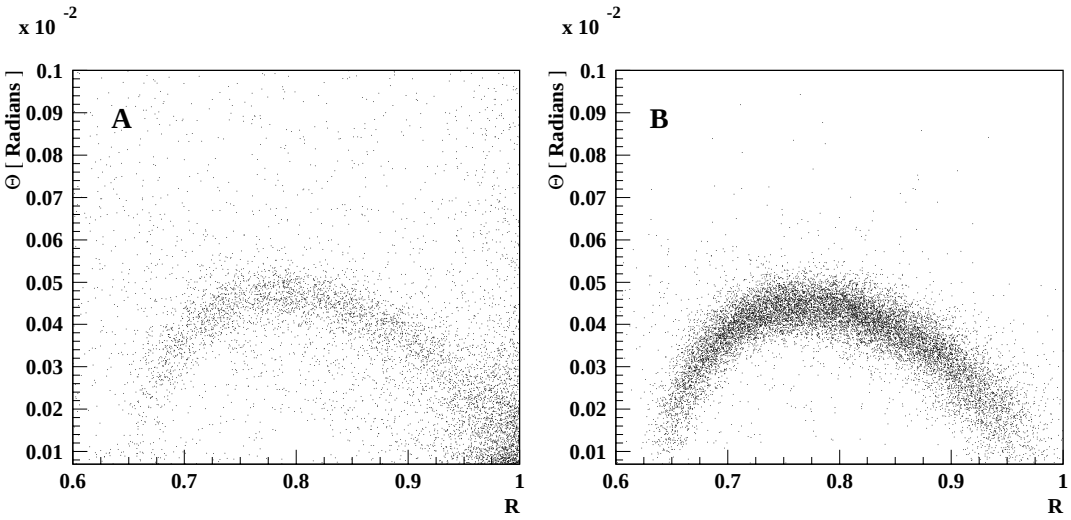

Figure 33: $R-\theta$ kinematic plots for Σ^+ decays. Plot (A) was obtained using experimental data, Plot (B) – using embedded Monte-Carlo events.

butions for the real data decays and the embedded events center at substantially the same mass value (1.188 GeV/c^2 and 1.190 GeV/c^2) and have very close widths

[27] Values of the kinematic variables shown were calculated for 572GeV/c Σ^+ hyperons produced on Be target at +4 mrad targeting angle.

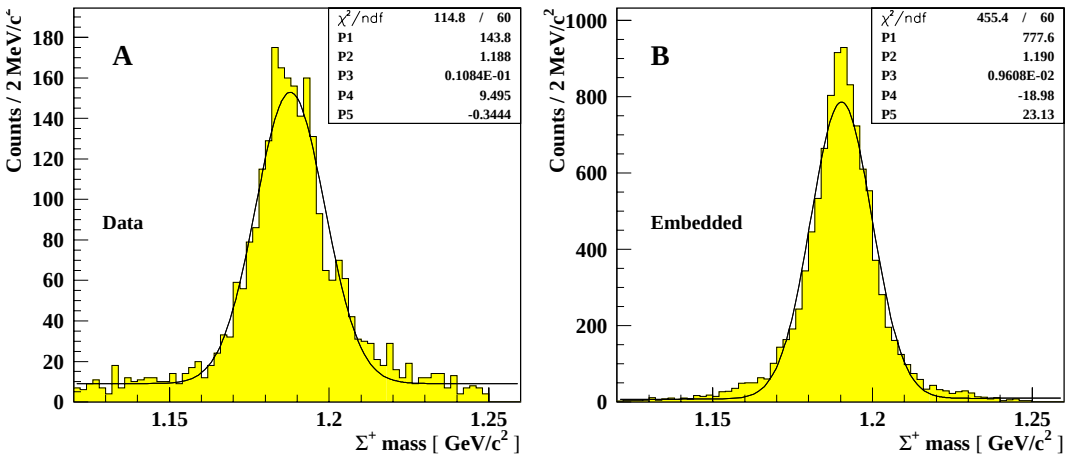

Figure 34: Σ^+ mass distributions for the actual Σ^+ decays (Plot (A)) and the embedded Monte-Carlo events (Plot (B)).

(10.8 MeV/c^2 and 9.4 MeV/c^2). The difference in the amount of the background under the mass peaks in the Σ^+ mass distributions is probably attributable to the lack of a large proton background in the embedded data sample.

Efficiency of $\Sigma^+ \to p\pi^0$ Decay Reconstruction

Next, the embedding was used to determine the efficiency of the reconstruction of the $\Sigma^+ \to p\pi^0$ decays used to measure the Σ^+ hyperon polarization. To study the reconstruction efficiency, an embed-data file containing only $\Sigma^+ \to p\pi^0$ Monte-Carlo generated decays was prepared. The number of reconstructed events in the Σ^+ mass peak was compared to the total number of the embedded decays. This procedure was done for a set of bins in the Z coordinate of the kink. Figure 35 shows the Z coordinate distributions of the embedded (a) and the reconstructed (b) $\Sigma^+ \to p\pi^0$ decays, as well as the efficiency (c) of this reconstruction as a function of Z coordinate of the decay. The efficiency of the reconstruction is almost uniform with Z in Z range 100 cm to 600 cm. Its average value in the designated decay region

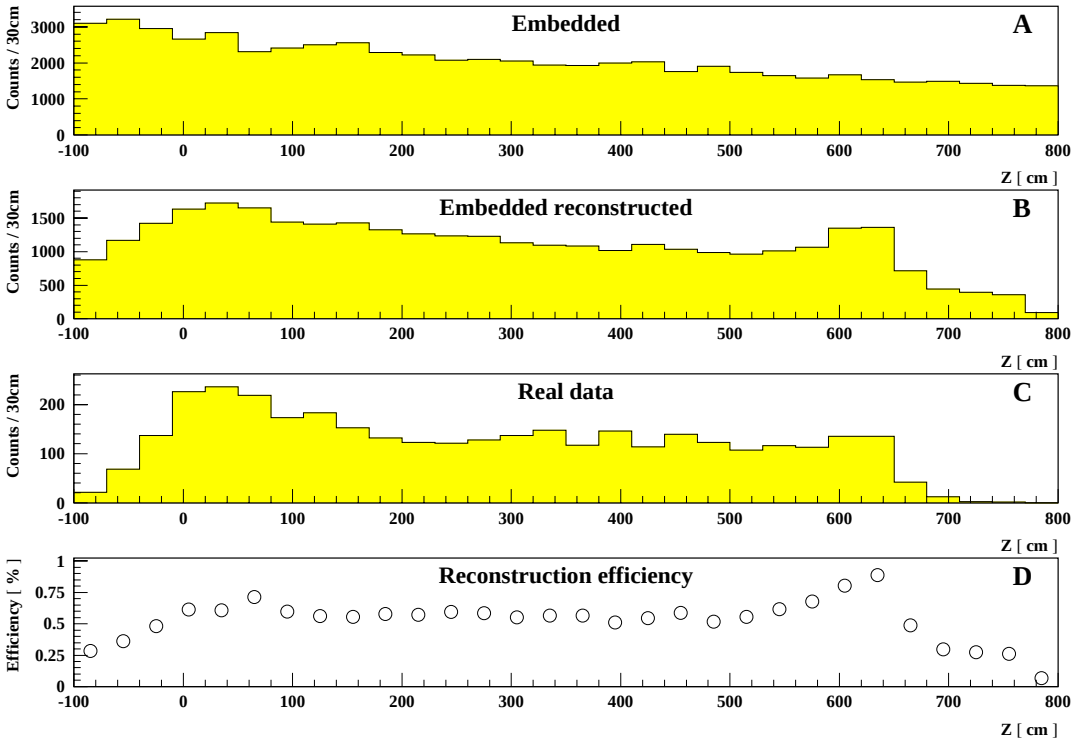

Figure 35: Z distributions of the Σ^+ decays. Plot (A) corresponds to the embedded $\Sigma^+ \to p\pi^0$ events; Plot (B) to reconstructed $\Sigma^+ \to p\pi^0$ embedded events; Plot (C) to $\Sigma^+ \to p\pi^0$ decays from 572 GeV/c data; and Plot (D) to the reconstruction efficiency for the $\Sigma^+ \to p\pi^0$ decay.

(from 100 cm to 600 cm) is about 50 %. 30 % of the reconstruction inefficiency is the result of the cut in the y projection of the Σ^+ decay angle (daughter proton angle relative to the original Σ^+ track direction), which was used to eliminate underlying proton background, see discussion in Chapter 5 above. The remaining reconstruction inefficiency is due to the limited resolutions and efficiencies of the detectors, multiple scattering, detector noise, and other inefficiencies and limitations.

Reconstruction of the apparatus

function and the polarization

The $\cos\Theta_y$ distributions corresponding to the Σ^+ hyperons produced at positive and negative targeting angles, as well as the sum thereof are shown in Figure 36. Plots (A), (C), and (E) on the left side of this figure represent the distributions calculated from the real data [28]. The right three plots (Plots (B), (D), and (F)) show the same distributions, but obtained using the embedded Monte-Carlo simulated events. The angular distributions presented in Figure 36 were simulated with -20% Σ^+ production polarization. Finally, the polarization value obtained from the analysis of the embedded events was checked for agreement with the polarization value used in the generation of the events. Figure 37 shows the asymmetry plots with respect to the $\cos\Theta_y$ variable in the Σ^+ center of mass system calculated using the bias cancelling techniques. Note that the asymmetry with respect to cosine of the angle Θ_y gives the right polarization value (-20%). Accordingly, the results of the Monte-Carlo simulation do not reveal the presence of any significant systematic bias in the experimental apparatus or the data analysis software that may affect the measured polarization value.

Systematic Error Due to the Event Selection

Imposing analysis cuts may introduce a systematic error into the measured polarization. This happens if there is a systematic dependence of the polarization on the variable used in the cut. If the polarization values for the rejected events and for the events used in the measurement are the same, imposing the analysis cut will not affect the measured polarization value. On the other hand, if the polarization of the events being rejected by the cut is different from the polarization of the kept events,

[28] Corresponding to 572GeV/c Σ^+ hyperons produced on Be target at +4 mrad targeting angle.

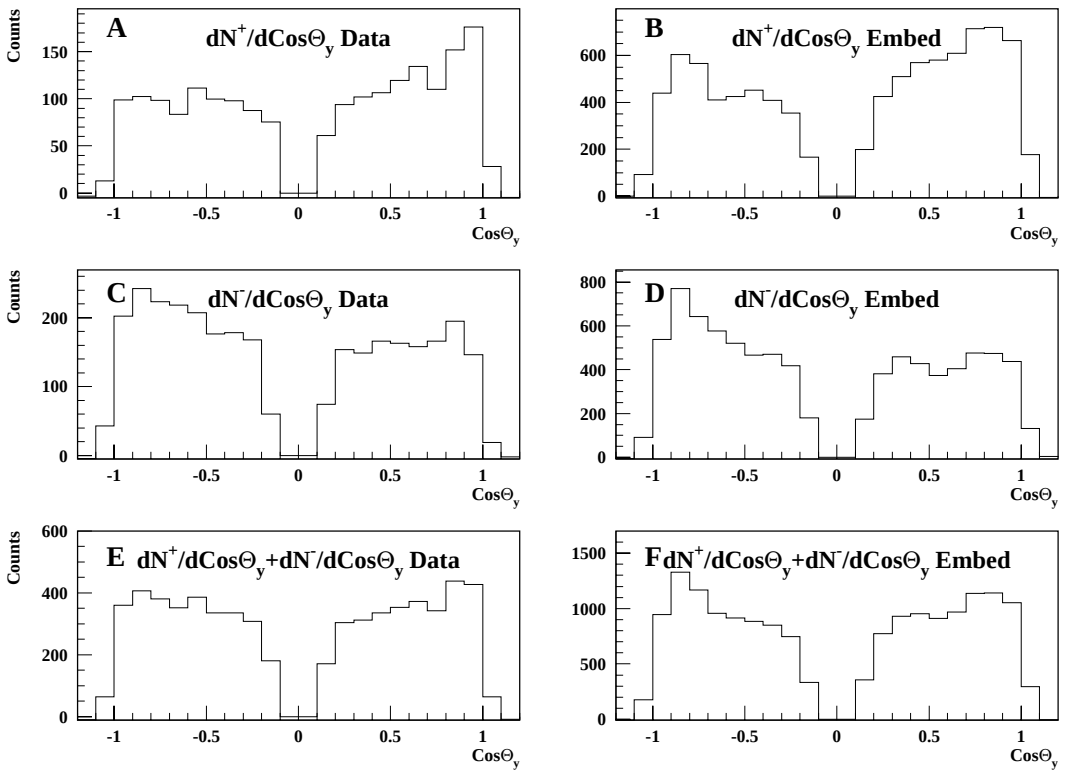

Figure 36: $\cos\Theta_y$ distributions. Plots (A) and (C) correspond to the real data, Plots (B) and (D) to the embedded events. Plots (A) and (B) correspond to +4 mrad targeting angle, Plots (C) and (D) to −4 mrad targeting angle, and Plots (E) and (F) to the sum of both +4 mrad and −4 mrad components (representing measured apparatus functions).

it is possible to cut events with, for example, higher than average polarization, and the measured polarization value will, therefore, decrease. To detect the presence of a systematic error, we first use test cuts to measure the polarization of the events near the regions that are being rejected by the analysis cuts. Subsequently, the polarization of the kept events is measured. Then both values are fitted with a constant. The χ^2 of this fit tells whether the two values are consistent with one another. This procedure is repeated for all the cuts made. All these fits have a

[28]Given polarization values for rejected and kept events correspond to the test cuts performed on the 572GeV/c Σ^+ hyperons produced on Be target at +4 mrad targeting angle.

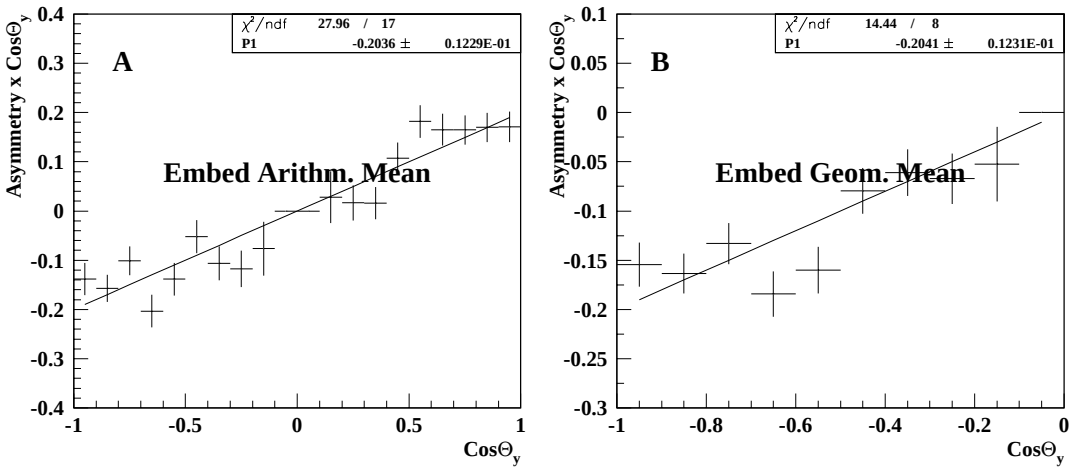

Figure 37: $\cos\Theta_y$ asymmetry plots for embedded events with polarization -20%. Fit parameter P1 represents the polarization value.

single degree of freedom. The χ^2 distribution must, therefore, have a mean of 1 and a width of $\sqrt{2} \approx 1.4$.

To determine the polarization of the events near the edges of the cuts, we used a set of test cuts shown in Table 12. We take the systematic difference between the polarization of the "nearly" rejected and the kept events as an upper bound on the systematic error in the answer. Indeed, keeping the rejected events will not be able to pull the polarization value of the rest of the data sample by more than this difference. The systematic difference in polarization can be determined by looking at the χ^2 of the above fits. The problem is that for one degree of freedom the above χ^2 distribution is fairly wide. To estimate the systematic error more accurately, we subdivided corresponding ranges of the cut variables into 4 bins, making the number of degrees of freedom equal to 3 as opposed to 1 for 2 bins.

Again, if there is no systematic error, the χ^2 distribution of the fits of the polarization values for these bins with a constant must have a mean of 1. Any deviation of the mean of the χ^2 distribution from 1 is due to the systematic de-

Variable name	Variable	Limits			
		Original Cut		Test Cut	
		Lower	Upper	Lower	Upper
Kink angle	θ_{kink}[mrad]	0.2	–	0.3	–
Y Kink angle	θ_y[mrad]	0.1	–	0.2	–
R parameter	R	0.64	0.88	0.68	0.84
Σ^+ mass	m_{Σ^+}[GeV/c^2]	1.16	1.21	1.17	1.20
Z-coordinate of the decay	z_{kink}[cm]	80	610	100	590

Table 12: Original analysis cuts and the test cuts used in estimating the systematic error in the polarization due to the non-stability of the polarization across the ranges of the corresponding cut variables.

pendence of the polarization on the cut variable. The value of the mean of the χ^2 distribution provides information on the systematic difference of the polarizations within the sample, as compared to the corresponding statistical error. The value of the systematic difference in this case will be the following [20]:

$$\sigma_{syst} = \sigma_{stat}\sqrt{< \chi^2 > -1},$$

where σ_{stat} and σ_{syst} are values of the statistical and estimated systematic errors in the polarization, respectively. Figures 38 (A)-(E) show the variation in the polarization value with variation of the cuts used in the event selection. Polarization values for sets of two bins representing rejected and kept events for every test cut are fitted with a constant and the χ^2 distribution of these fits is shown in Figure 38 (F). The mean of the shown χ^2 distribution is 1.32. The deviation of the χ^2 from 1.0 (which in the present case is 0.32) is presumably due to the systematic error. Accordingly, the value of the systematic error in the polarization estimated using this method is $\sqrt{0.32} \approx 0.55$ of the value of the corresponding statistical error. It must be noted that the value of the systematic error contribution from the event selection determined in such a way is very dependent on the original analysis cuts

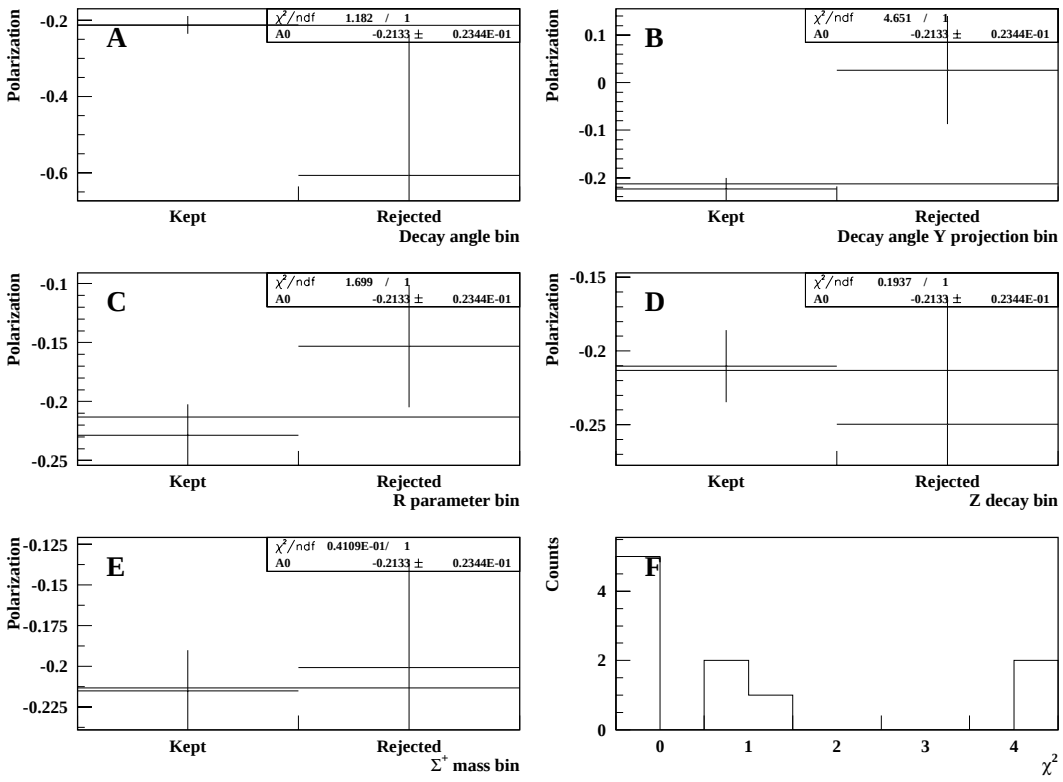

Figure 38: Polarization values corresponding to events rejected by the selection cuts, as well as the kept events. Both of the above values are fitted with a constant (Plots (A)-(E)). The Plots (A)-(E) were made for 572GeV/c hyperons produced on Be target. The χ^2 distribution of these fits as well as the corresponding fits for the second (Cu) production target is shown in Plot (F).

as well as the test cuts used. Another quite obvious explanation for the observed discrepancy is the large value of statistical fluctuation in the value of the χ^2 due to the small number of bins (2) in individual polarization distributions (Figures 38 (A)-(E)) and the small number of variables (5) over which the values of χ^2 were averaged. Therefore, if the systematic error is not clearly detected by the above method, its value should be neglected. Here, because the value of the average χ^2 is statistically consistent with 1.0, any discrepancy cannot be taken seriously as an indication of a systematic error in the polarization caused by the cuts.

Another way to estimate the systematic uncertainty in the polarization measurement result is to use the stability of the polarization value across the entire ranges of variables used in the event selection cuts. Figures 39 (A)-(E) show the

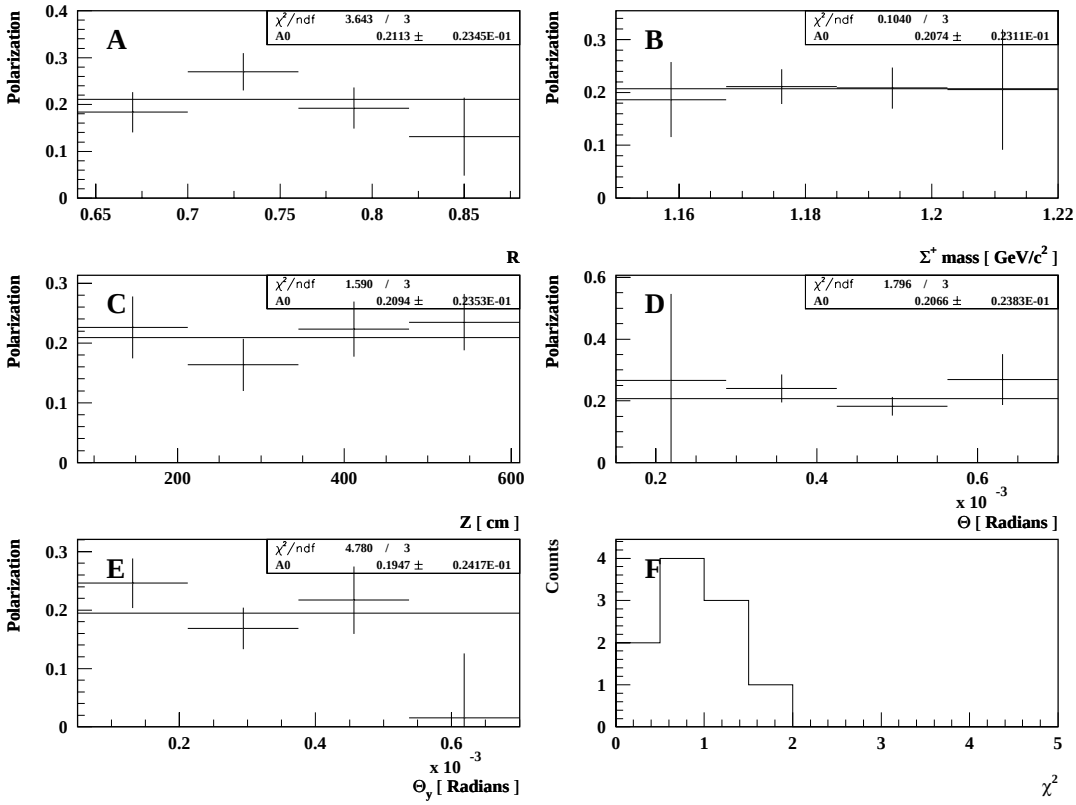

Figure 39: Stability of the polarization value across the ranges of variables used in the event selection cuts. The plots were made for 572GeV/c hyperons produced on Be target. Plots (A)-(E) show the polarization values for sets of four bins fit with a constant. The last plot (Plot (F)) represents the χ^2 distribution of these fits, as well as the corresponding fits for the second (Cu) production target.

polarization values for four separate bins in the ranges of the five variables used in the event selection. Polarization values for sets of four bins are fitted with a constant and the χ^2 distribution of these fits is shown in Figure 39, Plot (F). The mean of the χ^2 distribution is 0.94. Deviation of the χ^2 from 1 in the present case is negative, therefore no systematic error is seen.

Systematic error due to the

mis-measurement of the decay angle

An incorrectly measured decay angle θ_y will also introduce a systematic error into the polarization value. The correctness of the angle may be checked roughly using the $\cos\Theta_y$ distributions. First of all, because these distributions center at 0, we conclude that there is no significant shift in the θ_y scale. θ_y decay angle plots obtained using straight undecaying tracks also center at 0. This supports the above conclusion. Additionally, because $\cos\Theta_y$ distributions do go to 0 at $\cos\Theta_y = \pm 1$, the scale of the θ_y measurement is not significantly wrong.

The embedded data were used to determine the resolution of $\cos\Theta_y$ reconstruction. Figure 40 (a) shows the histogram of the difference in the $\cos\Theta_y$ of the generated and the reconstructed embedded events. The resolution of the measurement of the cosine of the decay angle Θ_y is about 0.05. Note that the width of the bins in the $\cos\Theta_y$ plots used in the asymmetry fits was selected to be not smaller than this value. Plot (b) in Figure 40 shows the systematic change in the error of the $\cos\Theta_y$ as a function of $\cos\Theta_y$. The slope of the fit is $\approx 3 \cdot 10^{-3}$. It is easy to see that this value of the slope will result in $P \times 3 \cdot 10^{-3}$ error in the polarization P, or ≈ 0.0006. The observed uncertainty in $\cos\Theta_y$ is the result of the limited resolution of the detectors as well as the effect of the multiple scattering.

Systematic error due to non-uniform

acceptance of the apparatus

The non-uniform acceptance function of the experimental apparatus can also contribute to the systematic error in the measured polarization value. Non-uniformity of the acceptance my be caused by faults in the detectors (dead wires), geometry

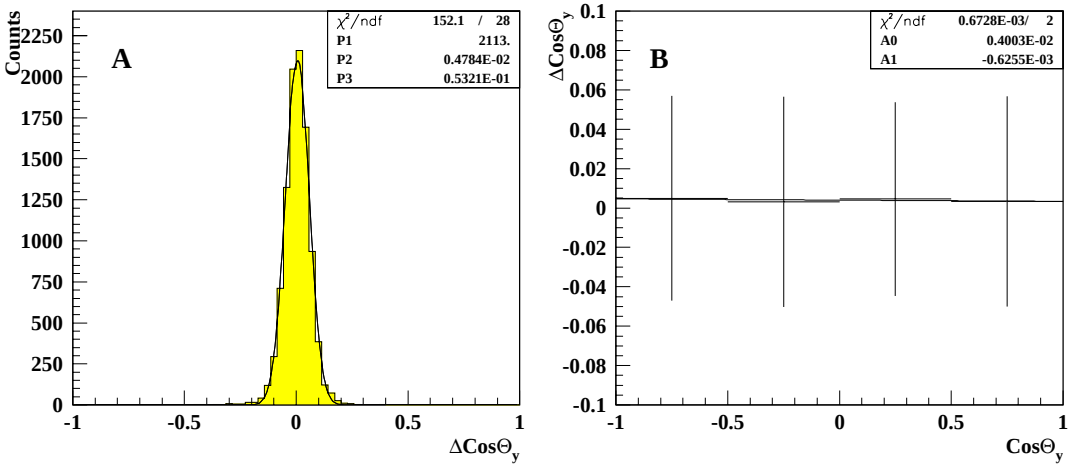

Figure 40: Difference in $\cos\Theta_y$ decay angle of the generated and reconstructed embedded events. Plot (A) shows the value of this difference; Plot (B) shows this difference as a function of $\cos\Theta_y$. Fit parameters P2 and P3 in Plot (A) represent the mean and the width of the $\Delta\cos\Theta_y$ distribution, respectively. Fit parameter A1 in Plot (B) represents the value of the corresponding slope.

(some particles miss certain detectors), and properties of the data analysis algorithm. For the bias cancelling technique to effectively eliminate the acceptance function of the apparatus, this function must be the same (in the center of mass of the decay frame) for corresponding beam components with both positive and negative targeting angles. In other words, the beam components with both positive and negative targeting angles must go into the same phase space region. Yet in other words, for each phase space region of the beam within which the bias cancelling technique is applied, the distribution of the beam particles should be the same (or even better uniform) for both beam components. Non-uniformity in the phase space distribution of the beam Σ^+ hyperons may cause systematic uncertainty in the measured polarization. To eliminate this systematic error, the phase space of the beam is

[29]Polarization value is given for 572GeV/c Σ^+ produced at +4 mrad targeting angle on Be target.

Combination number	Number of bins			Polarization [29] value	Statistical uncertainty
	$\theta_{y_{BM}}$	$\theta_{x_{BM}}$	$\cos\Theta_y$		
1	1	1	24	-0.210	0.023
2	2	1	24	-0.206	0.024
3	1	2	24	-0.196	0.026
4	1	1	48	-0.192	0.025
5	2	1	48	-0.201	0.025
6	1	2	48	-0.179	0.027
7	**2**	**2**	**24**	**-0.192**	**0.026**
8	2	2	48	-0.174	0.028

Table 13: Various binning combinations used in estimating the systematic error in the polarization caused by the non-uniformity in the phase space distribution of the beam hyperons. Averaged (over all bins in the binning combination) polarization value corresponding to combination 7 (in bold) was used as the measured polarization value.

divided into a number of bins with a roughly uniform distribution of beam particles for both positive and negative beam components within the bin, and the polarization is measured for each of these bins. The polarization values corresponding to a particular set of bins are then averaged to obtain a bin-averaged polarization value corresponding to a given binning combination (column 5 of Table 13. Finally, the bin-averaged polarization values for each set of bins are fit with a constant.

To estimate the systematic error due to the non-uniformity of the phase space distributions of the Σ^+ hyperons produced at positive and negative targeting angles, the number of bins is varied and the corresponding variation in the measured polarization value is taken as an upper limit of the corresponding systematic error. Table 13 shows eight combinations used in the binning of the Σ^+ phase space and the range of $\cos\Theta_y$ used in estimating the systematic error and the corresponding bin-averaged polarization values. Figure 41 (A) shows the distribution of these bin-averaged polarization values. Plot (B) in this figure shows the corresponding

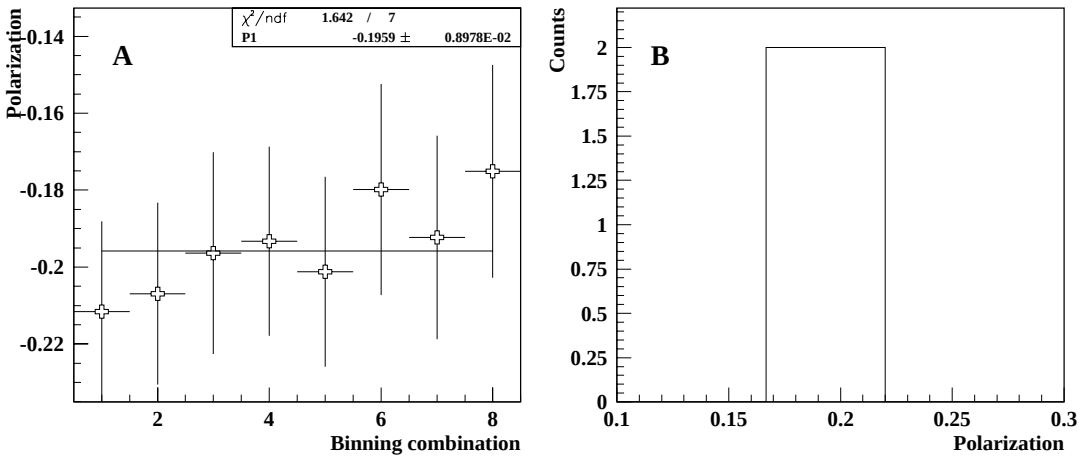

Figure 41: Average polarization magnitude. The result was obtained by averaging the polarization values corresponding to individual bins for binning combinations listed in Table 13 (Plot (A)), corresponding histogram of the average polarization values (Plot (B)).

histogram of the averaged polarization values, which centers at -0.195 and has the standard deviation of 0.009. The value of the standard deviation can be taken as an estimate for the systematic error contribution due to the non-uniformity in the phase space distribution of the beam Σ^+ hyperons. Figure 42 shows the stability of the polarization value across the ranges of the phase space parameters of the hyperon beam θ_x and θ_y. The polarization values for all sets of four bins are consistent with a constant.

Source of the contribution	Value of the contribution
Mismeasurement of the Θ_y	Negligible
Non-uniform beam phase space	0.009
Event selection	Negligible
Aggregate systematic error	**0.009**
Statistical error	**0.023**

Table 14: Various contribution to the systematic error in the measured polarization value.

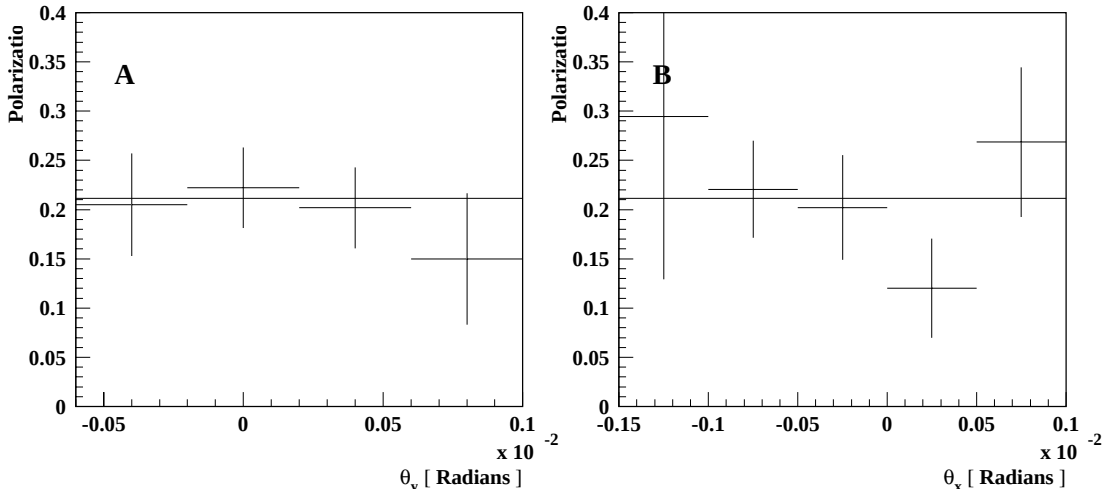

Figure 42: Stability of the polarization value across the ranges of the variables θ_y and θ_x describing the phase space of the hyperon beam. Plots (A) and (B) show the stability of the polarization as a function of θ_y and θ_x of the Σ^+ hyperon at the Hyperon Spectrometer, respectively.

Total Systematic Error

Table 14 summarizes various estimated contributions to the systematic error in the polarization. The total value of the systematic error of 0.009 was obtained by adding in quadratures the values of various contributions listed in Table 14.

Phase space of the beam

for different target materials

As another test of the reliability of the comparison of the values of the polarization corresponding to two different production targets, it can be checked whether the phase spaces of the beam corresponding to the two target materials significantly differ.

Figures 43 and 43 can be used to compare phase spaces of the secondary hyperon beams produced on different hyperon production targets. The figure shows

[29] The value of the systematic error quoted corresponds to 572GeV/c Σ^+ produced on Be target.

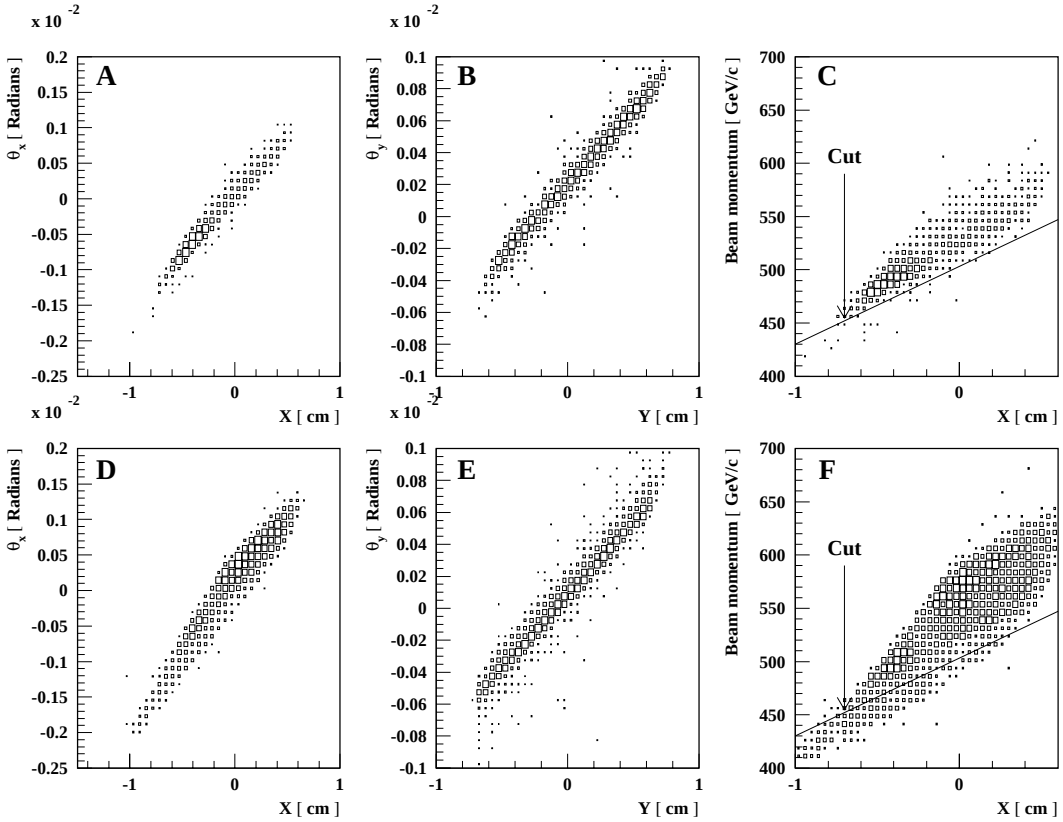

Figure 43: The phase space locations of the beam components with +4 mrad and −4 mrad targeting angles and beam momentum 572 GeV/c. Both beams were produced on Cu target. Plots (A-C) correspond to +4 mrad primary beam targeting angle, Plots (D-F) to −4 mrad. Plots (A) and (D) show x_{Σ^+} vs. $\theta_{x\Sigma^+}$ distributions, Plots (B) and (E) show y_{Σ^+} vs. $\theta_{y\Sigma^+}$ distributions, and Plots (C) and (F) show p_{Σ^+} vs. x_{Σ^+} distributions. This figure is to be compared with Figure 29, which shows corresponding distributions for Be target.

a good match between the phase spaces of the two beams.

It should be noted that even if the phase spaces were different, this would not automatically mean that the measurement of the polarization ratio is incorrect. As it has been stated in detail above, the bias cancelling technique applied to individual bins of the beam phase space would eliminate any influence of the non-uniformity of the phase space on the polarization answer.

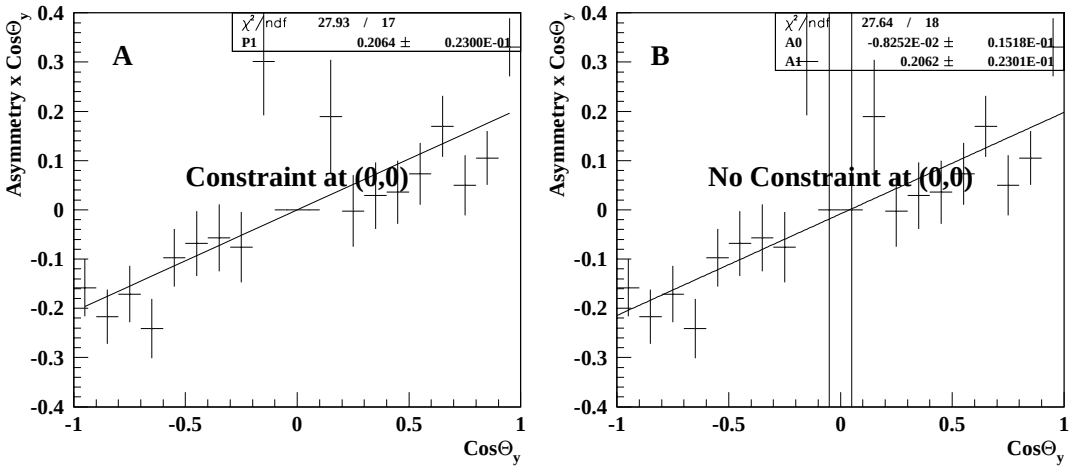

Figure 44: Comparison of the two fitting methods used to calculate the polarization. Plot (A) correspond to the fit with a constraint at 0, 0; while Plot (B) imposes no such constraint.

Dependence of the polarization

on the asymmetry fitting method

The asymmetry in the $\cos\Theta_y$ distribution used in the method of arithmetic mean to calculate the polarization may be fit with with a first order polynomial without a constraint at 0, 0 (two parameter fit), and also by demanding that the fit pass through 0, 0 (one parameter fit). The question arose whether these two fitting methods give the same polarization value. Note, that for the geometric mean method, both sides of corresponding distribution are symmetric, and the constraint must be imposed.

Figure 44 compares the results of the above two fitting methods. The polarization value differs for the two methods by less then 0.0002 and the intercept constant of the first order polynomial used in the fit is -0.008. The results are so close because $dN^+/d\cos\Theta_y$ and $dN^-/d\cos\Theta_y$ distributions used in the fit are scaled to have the same average (per bin) number of counts. When we subtract

these two distributions bin-by-bin the average number of counts in each bin is 0. For this reason, and because one distribution is approximate mirror of the other, the polynomial fit of the $(dN^+/d\cos\Theta_y - dN^-/d\cos\Theta_y)$ is close to 0 at 0.

CHAPTER VII

CHECK ON THE TARGETING ANGLES

The values of the electric currents in the magnets were originally calculated to provide chosen primary beam targeting angles using Fermilab's beam ray tracing program. This note attempts to verify the values of these angles using an independent calculation based on the values of the currents in the targeting magnets actually used. Figure 45 shows the schematic layout of the SELEX beam steering and targeting system.

p_t-kick in the Targeting Magnets

Dipole targeting magnets in the PC3 beam steering and targeting system are of two types. PC3H1 and PC3V are 6-3-120 beam line dipoles. For these magnets the Bdl integral is nearly linear for $I < 1000\ A$ and is given by the following formula: $\int Bdl = I(A)/195\ kG \cdot m$. Magnets PC3H2, PC3BR1, PC3BR2, and PC3BR3 are of 5-1.5-120 type. This type of magnet has a standard excitation curve. The excitation curve for the targeting magnets was taken from TM-434 manual. The manual gives the tabulated values of the magnetic integral Bdl in the magnet for a given set of the electric current values. These values were fitted with a 4rd order polynomial. The coefficients of the fit are the following: $a_0 = 1.956$, $a_1 = 0.01766$, $a_2 = 3.059 \cdot 10^{-5}$, $a_3 = -2.273 \cdot 10^{-8}$, $a_4 = 4.516 \cdot 10^{-12}$. Figure 46 shows the fitted Bdl excitation curve. Note that for electric currents above 1500 A deviation of the fit from a straight line is significant. The current values used with the polarization runs were used to calculate the appropriate values of the P_t-kick. Note that magnet PC3BR consists of 3 serially connected magnets PC3BR1, PC3BR2, and PC3BR3.

Figure 45: Schematic layout of the SELEX beam steering and targeting system. The figure depicts Hyperon Magnet as well as targeting magnets H1, V, BR1-BR3 and H2. The solid line corresponds to the trajectory of 800 GeV/c protons producing +4 mrad beam targeting angle.

Table 15 summarizes for each polarization run the values of the current in the horizontal targeting magnets and the values of the p_t-kick $p_t = q \cdot \int Bdl$ calculated using the excitation curve fit.

The contribution of the fringe field of the Hyperon Magnet was calculated using Figure 6 of Ref. [13] representing the p_t deflection of the Hyperon Magnet at 3250 Amps. From this figure the p_t deflection of the beam corresponding to the Cu target with its center at 7.5 cm downstream of the channel entrance is 0.17 GeV/c,

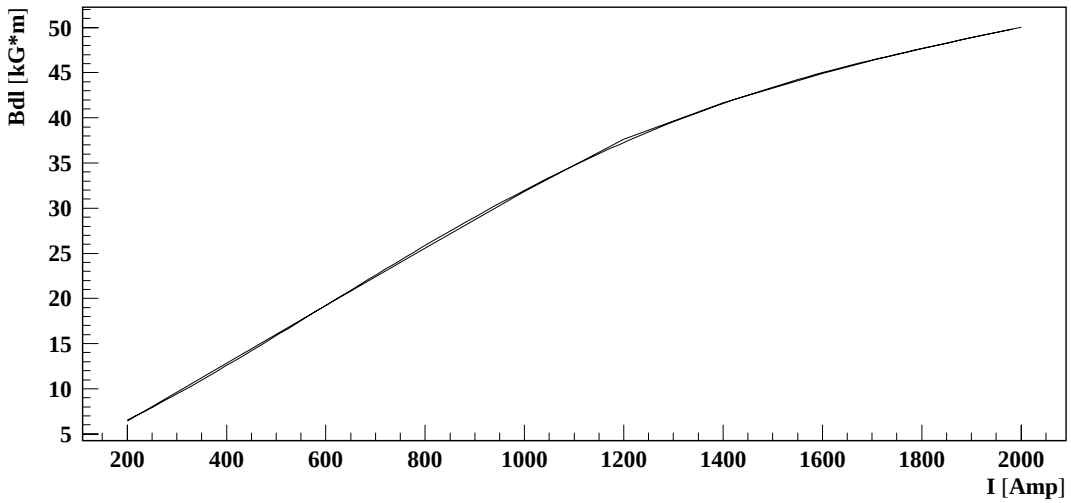

Figure 46: Bdl excitation curve for type 5-1.5-120 targeting magnet fitted with 4th order polynomial.

and for the Be target with its center at 20.3 cm downstream of the channel entrance the p_t deflection is 0.29 GeV/c, for the Hyperon Magnet current of 3250 Amps. These numbers were scaled in proportion to the momentum of the hyperon beam for each of 3 beam momenta. The resulting p_t contributions of the Hyperon Magnet fringe field are given in Table 15.

The total targeting angle (with respect to the direction of the primary beam entering the targeting system) is just a sum of the p_t-kicks in all the (horizontal) targeting magnets divided by 800 GeV/c – the momentum of the primary proton beam. This value is also given in the Table 15. As it can be seen from the table, the average magnitude of the targeting angle for all beam momenta is 3.87 mrad.

The numbers in the table show that positive targeting angles have been reproduced with high accuracy, while actual negative angles are generally smaller in magnitude than expected 4 mrad. This is because of the saturation in the PC3BR

TGT angle mrad	P_{BM} [GeV/c]	H1 I [A]	BR I [A]	H2 I [A]	H1 p_t-kick [GeV/c]	BR p_t-kick [GeV/c]	H2 p_t-kick [GeV/c]	PC3AN p_t-kick [GeV/c]	Calc angle mrad
Cu target									
+4	572	483	-892	-800	0.77	-2.588	-0.776	0.15	4.08
-4	572	-992	1882	800	-1.55	4.376	0.776	0.15	-3.72
+4	500	503	-892	-800	0.77	-2.588	-0.776	0.13	4.07
-4	500	-1010	1882	800	-1.55	4.376	0.776	0.13	-3.66
+4	375	502	-892	-800	0.77	-2.588	-0.776	0.1	4.11
-4	375	-1005	1882	800	-1.55	4.376	0.776	0.1	-3.63
Be target									
+4	572	483	-892	-800	0.77	-2.588	-0.776	0.26	3.95
-4	572	-992	1882	800	-1.55	4.376	0.776	0.26	-3.86
+4	500	503	-892	-800	0.77	-2.588	-0.776	0.22	3.96
-4	500	-1010	1882	800	-1.55	4.376	0.776	0.22	-3.77
+4	375	502	-892	-800	0.77	-2.588	-0.776	0.17	4.03
-4	375	-1005	1882	800	-1.55	4.376	0.776	0.17	-3.72

Table 15: Values of the currents in targeting magnets, corresponding p_t-kick values and the total bend angle with respect to the entering primary beam direction for six configurations of the apparatus: a set of three different beam momenta and 2 complementary targeting angles. 1 mrad rotation of the target with respect to the PC3 beam line direction was taken into account in calculating the targeting angle, see Ref. [13].

magnets at 1881 amperes which was not taken into account when the currents were calculated.

Uncertainty in the Beam Targeting Angles

Uncertainty in the primary beam targeting angles is primarily due to the following three factors: the angular dispersion of the primary proton beam, the finite width of the hyperon production target, and the finite angular acceptance of the hyperon channel.

The primary proton beam has the angular divergence on the target of 0.17 mrad HWHM. This value can be taken as a rough estimate for the spread in targeting

angle. The resulting targeting angle is therefore 3.87 ± 0.2 mrad.

CHAPTER VIII

DISCUSSION OF THE RESULTS

Table. 16 summarizes for each data sample the number of events in the sample, the target material, the mean hyperon momentum, the corresponding P_t and X_f values, and the measured polarization. Statistical, as well as systematic errors are shown. The systematic uncertainties in the polarization value were estimated

Data Set	P_{beam} [GeV/c]	P_t [GeV/c]	X_f	Number of events	Polarization [%]	Uncertainty [%]	
						Stat	Syst
Copper target							
1	366(24)	1.41(0.09)	0.46(0.03)	2723	-12.9	± 3.3	± 1.1
2	478(36)	1.85(0.14)	0.60(0.05)	2905	-18.2	± 3.3	± 1.1
3	540(39)	2.09(0.15)	0.68(0.05)	4575	-14.2	± 2.9	± 1.0
Beryllium target							
4	364(27)	1.41(0.10)	0.46(0.03)	3542	-17.8	± 2.9	± 1.0
5	473(39)	1.83(0.15)	0.59(0.05)	3933	-23.0	± 2.8	± 0.9
6	535(40)	2.07(0.15)	0.67(0.05)	5128	-19.2	± 2.6	± 0.9

Table 16: Data samples utilized to measure Σ^+ polarization. For each data sample, the table gives the value of the Σ^+ momentum, values of the corresponding P_t and X_f variables, number of the $\Sigma^+ \to p\pi^0$ decays used to measure the polarization, the polarization value and the uncertainty. Numbers in parentheses next to P_{beam}, P_t, and X_f represent the widths (σ of the gaussian fit) of the corresponding P_{beam}, P_t, and X_f distributions.

by measuring false asymmetries i.e. the asymmetries of the $\Sigma^+ \to p\pi^0$ decays with respect to the angle that the daughter proton track forms with the two horizontal axes, see Chapter 5 above. We also studied the dependence of the measured polarization on the event selection criteria (see above) and the phase space binning of the hyperon beam, see Chapter 6 above.

Figure 47. shows the results of our measurements plotted against the existing data on the Σ^+ polarization. In order to compare our data with the results from

the Fermilab E761 experiment [1, 2], where data samples with higher statistics were used, we measured the polarization at P_t = 1.5 GeV/c, which corresponds to one of the E761 settings. The value of -12.9 ± 3.3 % for the Σ^+ polarization obtained here is in a good agreement with -12.0 ± 0.3 % reported in Ref. [1], see Figure 47.

To extend the study of the dependency of the polarization on the P_t and X_f obtained in E761 [1, 2], we performed measurements of the Σ^+ polarization at three P_t values of 1.41GeV/c, 1.84 GeV/c, and 2.08 GeV/c. We observe that Σ^+ hyperons are produced significantly (≈20 %) polarized at these high P_t. Comparison of the measurement at $P_t \approx 2$ GeV/c with the E761 results [2] for $P_t \approx 1$ GeV/c and $P_t \approx 1.5$ GeV/c suggests that the magnitude of the polarization grows more slowly with X_f at higher P_t values.

The dependence of the hyperon polarization on the production target material was studied by Heller *et al.* in Ref. [3, 4] for Λ^0 and Ξ^- hyperons at 0.6 GeV/c $< P_t <$ 1.9 GeV/c. In that study the production polarization of Λ^0 hyperons was measured for Be and combined Cu/Pb targets. The Λ^0 polarization magnitude obtained from the combined Cu/Pb data was observed to be smaller than that from Be data by about 2/3. We are the first to observe a similar effect for Σ^+ hyperons at 1.41 GeV/c $< P_t <$ 2.08 GeV/c. The dependence of the polarization on the production target material was studied here by using Cu and Be targets. The magnitude of the polarization for Σ^+ hyperons produced on the heavier (Cu) target were found to be consistently smaller than the corresponding polarization magnitudes for Σ^+ hyperons produced on the lighter (Be) target, see Figure 47. Measurements were performed at three different P_t values in P_t range 1.41 GeV/c $< P_t <$ 2.08 GeV/c. The average ratio of the Σ^+ polarization values for Cu and Be in this P_t range is 0.71 ± 0.08, see Figure 48. This is the first observation of the

A-dependence of the hyperon polarization at $P_t \approx 2$ GeV/c. Such A-dependence is not clearly understood, especially for high P_t values. Supposedly, at high P_t the effects of the nuclear structure of the production target should be negligible. Our measurement indicates that, to the contrary, a significant A-dependence still exists for P_t values of up to 2 GeV/c.

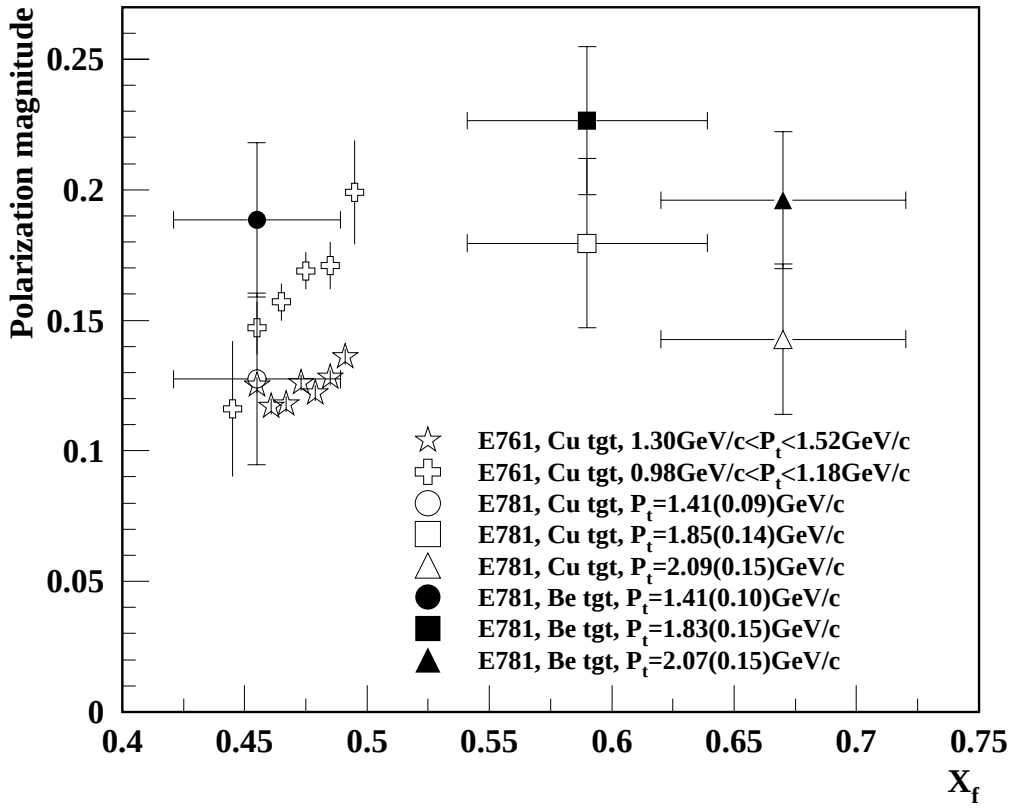

Figure 47: X_f dependence of the Σ^+ polarization (only statistical errors are shown). Open symbols correspond to the Cu production target, filled symbols – to the Be target. Open crosses and stars represent the E761 data [2] at $P_t \approx 1$ GeV/c and $P_t \approx 1.5$ GeV/c, respectively. Circles correspond to the present measurement at $P_t \approx 1.41$ GeV/c. Boxes correspond to the present measurement at $P_t \approx 1.84$ GeV/c. And, finally, triangles correspond to the present measurement at $P_t \approx 2.08$ GeV/c. Horizontal error bars represent the widths (σ of the gaussian fit) of the corresponding X_f distributions. Numbers in parentheses next to P_t represent the widths (σ of the gaussian fit) of the corresponding P_t distributions.

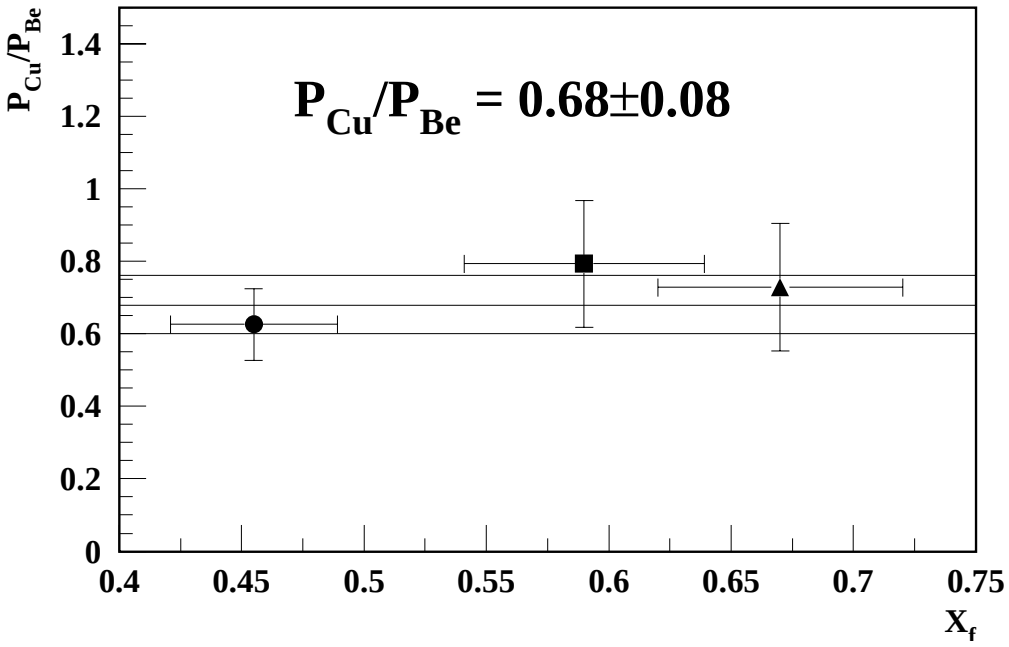

Figure 48: Ratio of the Σ^+ polarization values for Cu and Be targets. The ratio was calculated using the results of the present measurement and the E761 data [2] (only statistical errors are taken into account). The horizontal line corresponds to the average ratio of 0.71 ± 0.08. Horizontal error bars represent the widths (σ of the gaussian fit) of the corresponding X_f distributions.

APPENDIX A

ADDITIONAL DATA PLOTS

This Appendix provides additional data plots that were not included in the main body of the thesis because of the space limitations. However, these plots are necessary to present a complete picture of the results of the data analysis described above.

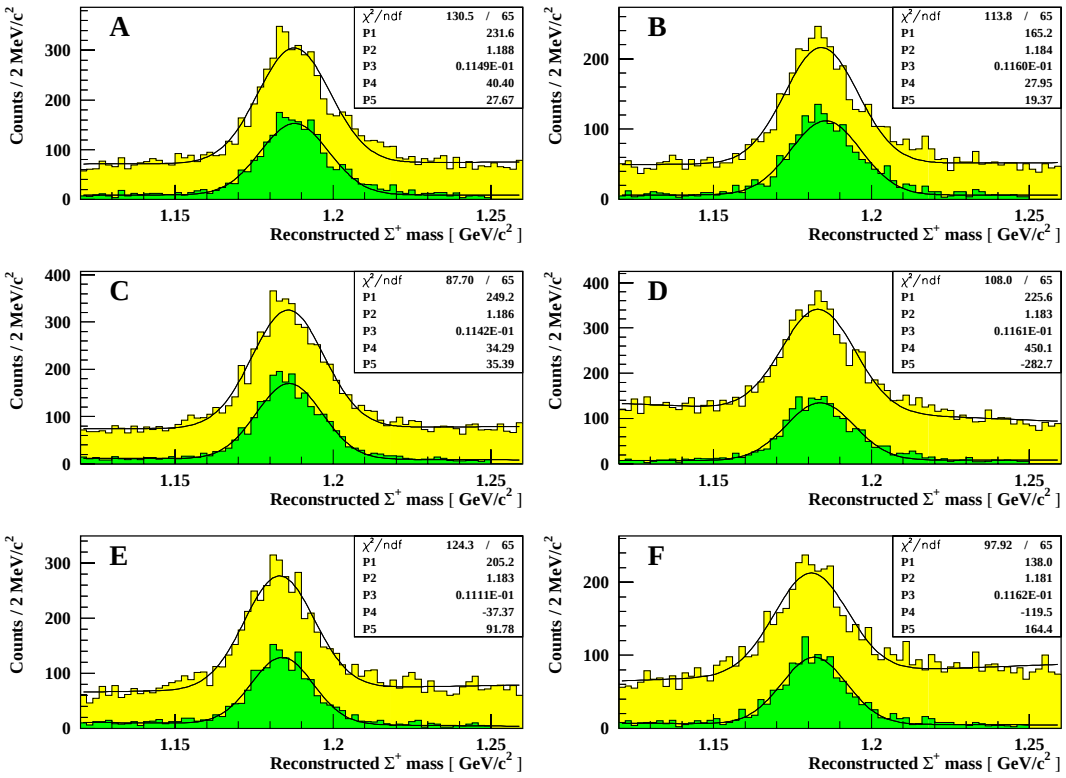

Figure 49: Σ^+ mass distributions calculated from the $\Sigma^+ \rightarrow p\pi^0$ decay (upper histograms). The lower histograms corresponds to the same mass distributions, but after selection cuts were imposed. Fit parameters P2 and P3 represent the center and the width of the Gaussian fit to the Σ^+ mass distribution, respectively. Plots (A), (C), and (E) correspond to Be production target, Plots (B), (D), and (F) correspond to Cu target. Plots (A) and (B) correspond to 572GeV/c hyperons, Plots (C) and (D) correspond to 500GeV/c hyperons, and Plots (E) and (F) correspond to 375GeV/c hyperons.

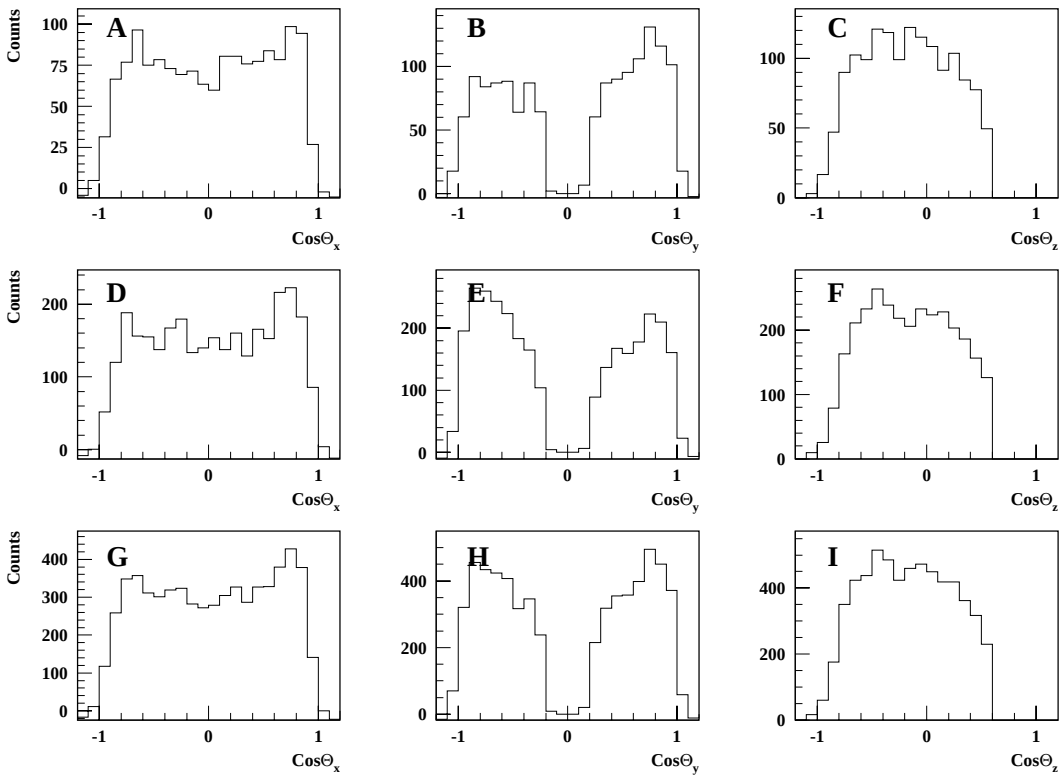

Figure 50: Distribution of the cosines of the X, Y, and Z components of the Σ^+ decay angle (proton angle) $\cos\Theta$. The distribution was calculated in the center of mass of the decay system for 572 GeV/c hyperons produced on Cu target. Plots (A)-(C) correspond to the +4mrad targeting angle, Plots (D)-(F) to the −4mrad targeting angle, and Plots (G)-(I) to the sum of both the +4mrad and −4mrad components.

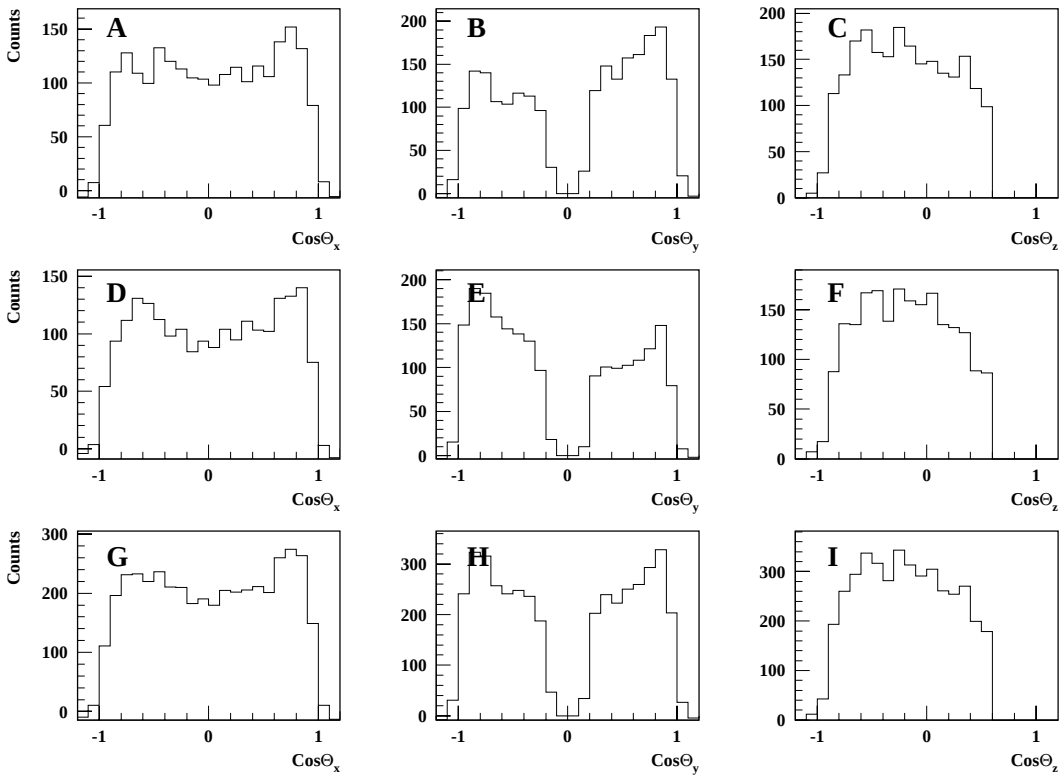

Figure 51: Distribution of the cosines of the X, Y, and Z components of the Σ^+ decay angle (proton angle) $\cos\Theta$. The distribution was calculated in the center of mass of the decay system for 500 GeV/c hyperons produced on Be target. Plots (A)-(C) correspond to the +4mrad targeting angle, Plots (D)-(F) to the −4mrad targeting angle, and Plots (G)-(I) to the sum of both the +4mrad and −4mrad components.

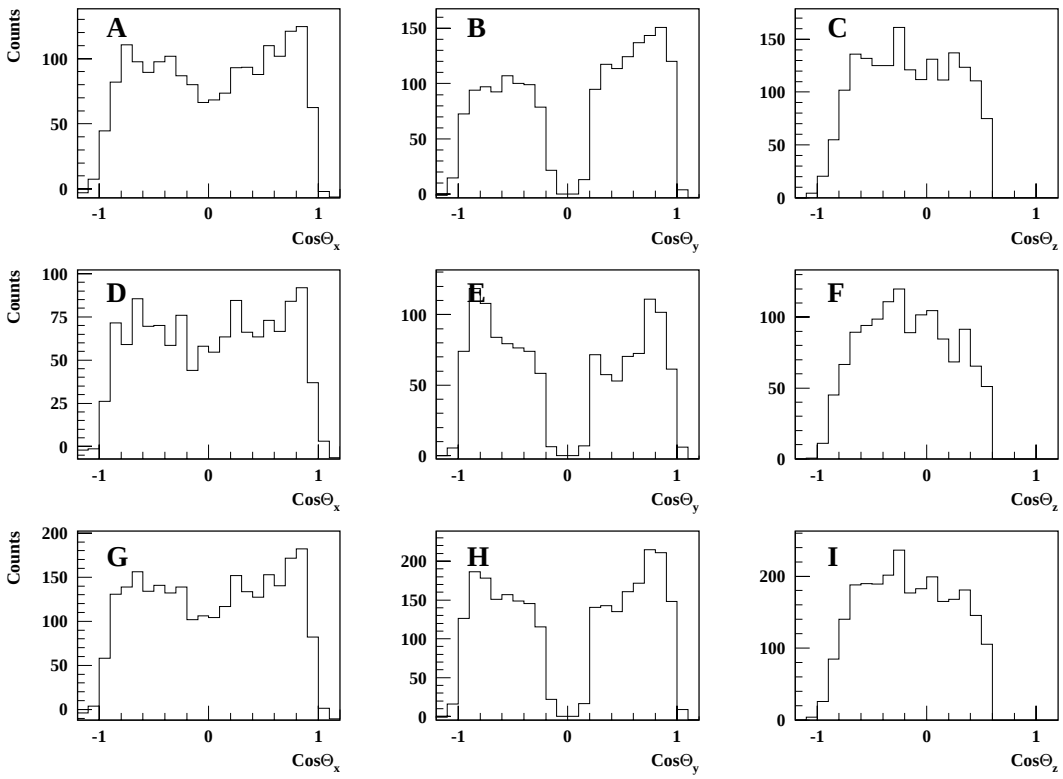

Figure 52: Distribution of the cosines of the X, Y, and Z components of the Σ^+ decay angle (proton angle) $\cos\Theta$. The distribution was calculated in the center of mass of the decay system for 500 GeV/c hyperons produced on Cu target. Plots (A)-(C) correspond to the +4mrad targeting angle, Plots (D)-(F) to the −4mrad targeting angle, and Plots (G)-(I) to the sum of both the +4mrad and −4mrad components.

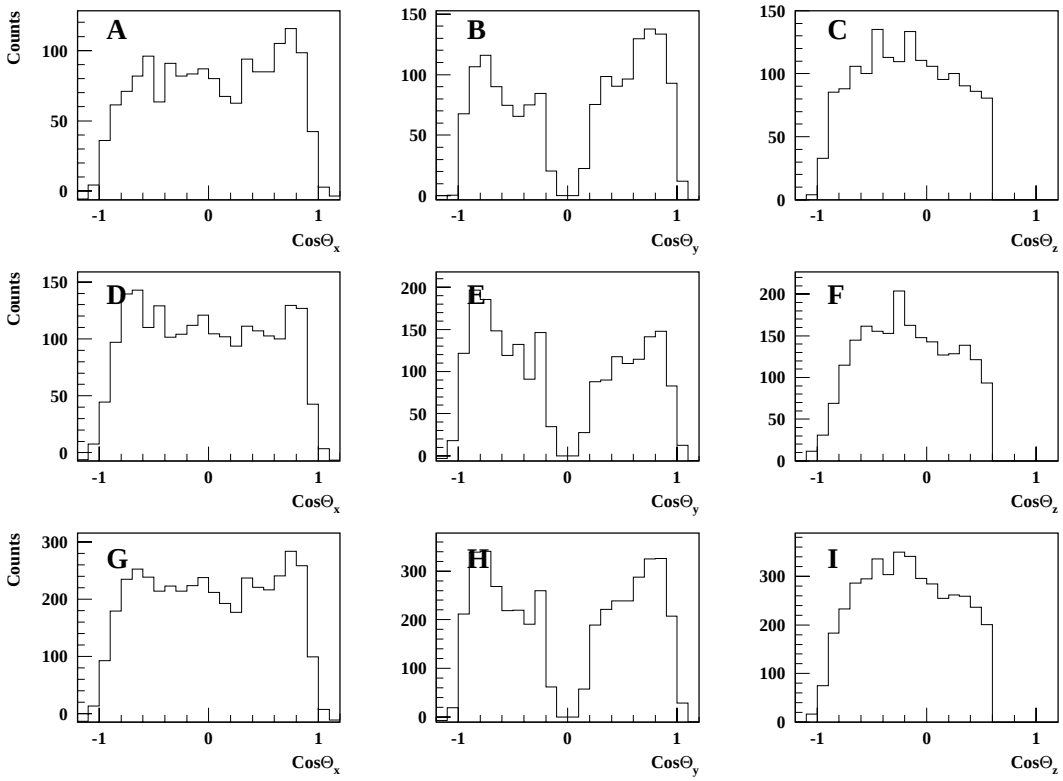

Figure 53: Distribution of the cosines of the X, Y, and Z components of the Σ^+ decay angle (proton angle) $\cos\Theta$. The distribution was calculated in the center of mass of the decay system for 375 GeV/c hyperons produced on Be target. Plots (A)-(C) correspond to the +4mrad targeting angle, Plots (D)-(F) to the −4mrad targeting angle, and Plots (G)-(I) to the sum of both the +4mrad and −4mrad components.

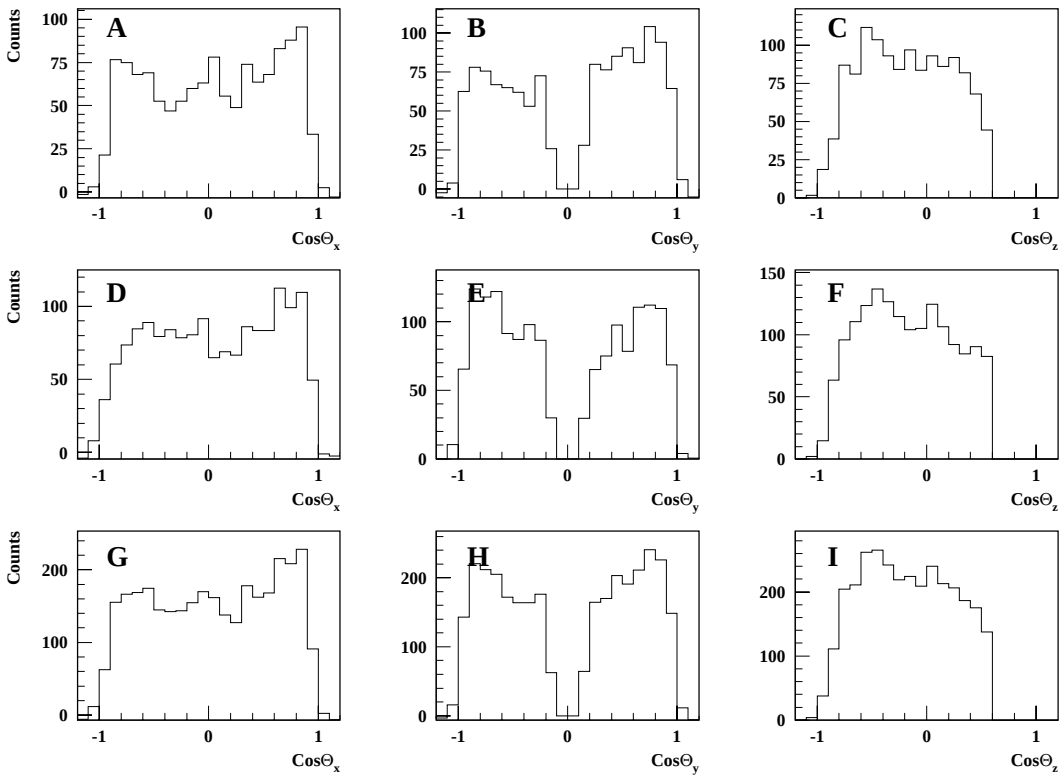

Figure 54: Distribution of the cosines of the X, Y, and Z components of the Σ^+ decay angle (proton angle) $\cos\Theta$. The distribution was calculated in the center of mass of the decay system for 375 GeV/c hyperons produced on Cu target. Plots (A)-(C) correspond to the +4mrad targeting angle, Plots (D)-(F) to the −4mrad targeting angle, and Plots (G)-(I) to the sum of both the +4mrad and −4mrad components.

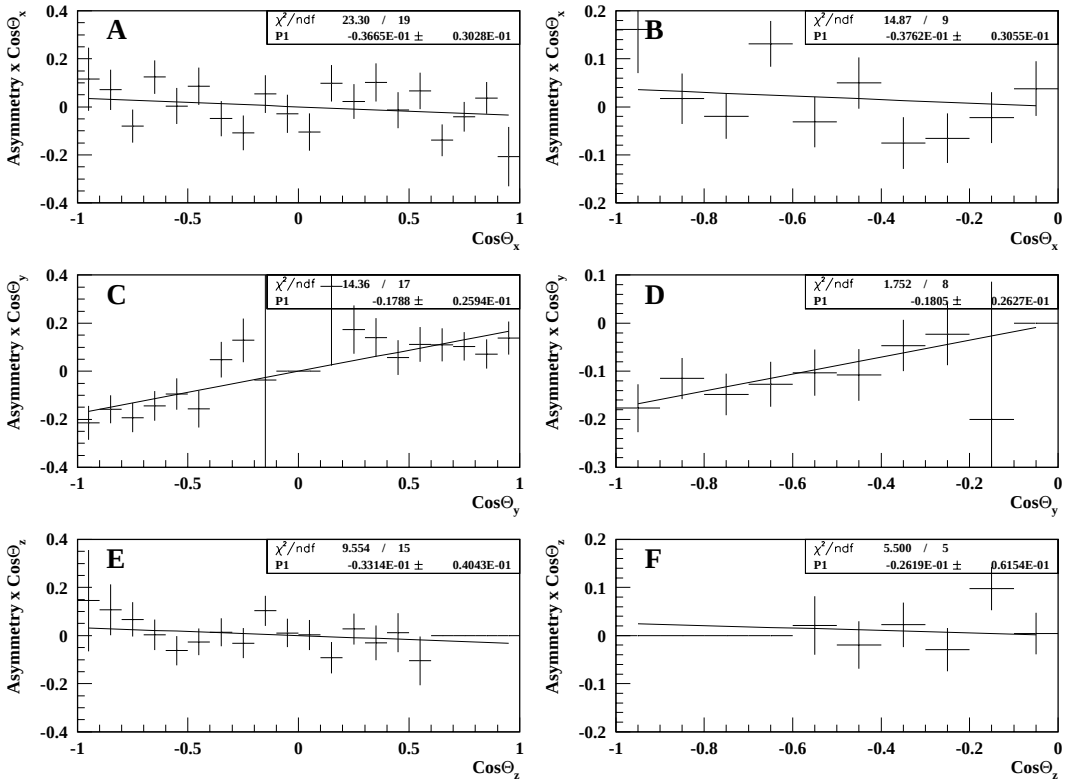

Figure 55: Asymmetries with respect to the cosines of the Σ^+ decay angles (proton angle) $\cos\Theta_x$, $\cos\Theta_y$, and $\cos\Theta_z$ in the center of mass frame of the decaying hyperon. Shown distributions correspond to Σ^+ hyperons with momentum 572 GeV/c produced on Cu target. Plots (A), (C) and (E) show the asymmetries calculated using method of arithmetic mean. Plots (B), (D) and (F) show the corresponding asymmetries calculated using method of geometric mean.

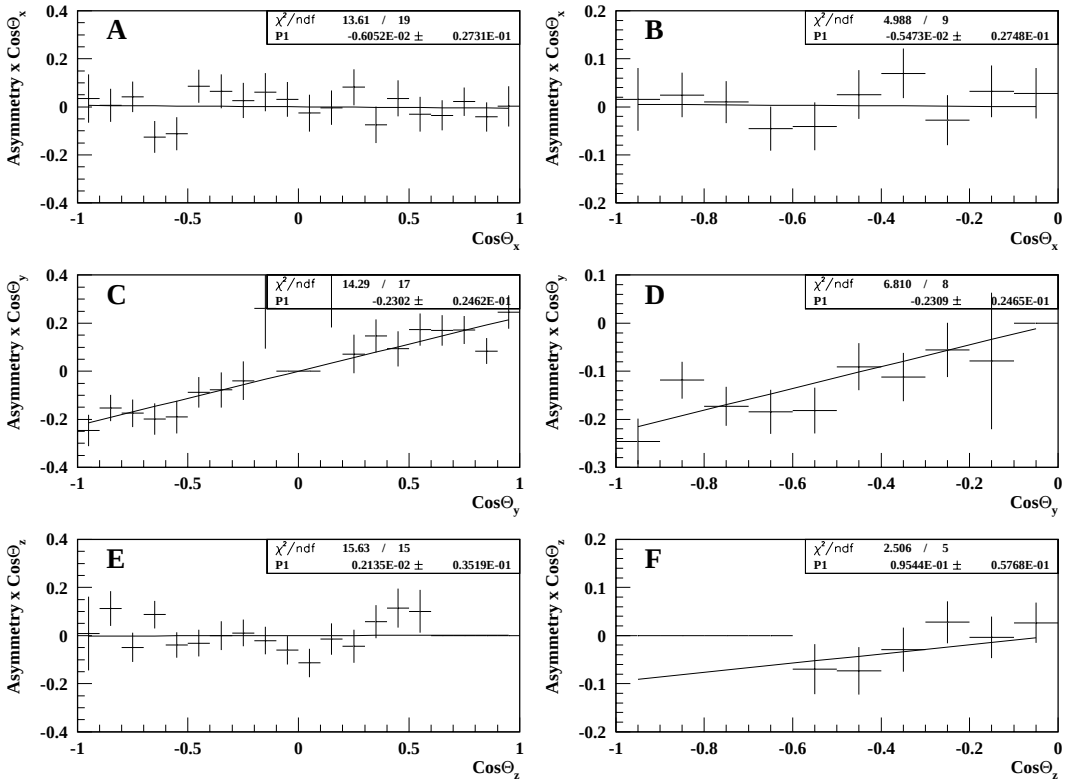

Figure 56: Asymmetries with respect to the cosines of the Σ^+ decay angles (proton angle) $\cos\Theta_x$, $\cos\Theta_y$, and $\cos\Theta_z$ in the center of mass frame of the decaying hyperon. Shown distributions correspond to Σ^+ hyperons with momentum 500 GeV/c produced on Be target. Plots (A), (C) and (E) show the asymmetries calculated using method of arithmetic mean. Plots (B), (D) and (F) show the corresponding asymmetries calculated using method of geometric mean.

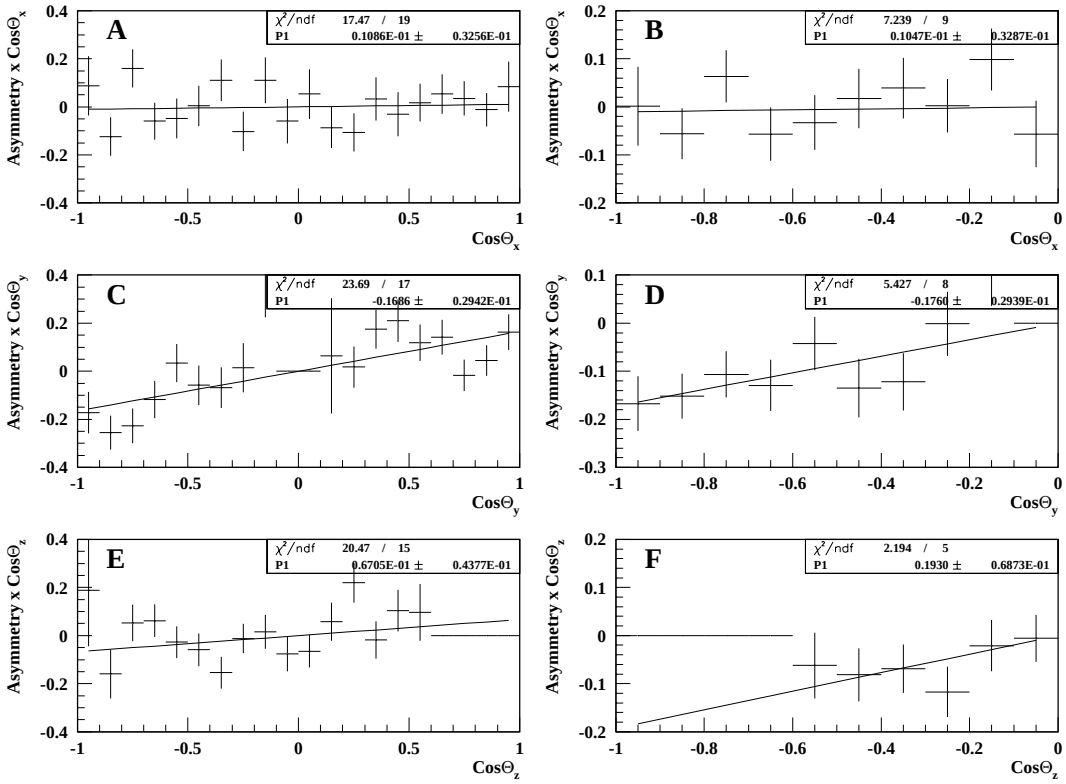

Figure 57: Asymmetries with respect to the cosines of the Σ^+ decay angles (proton angle) $\cos\Theta_x$, $\cos\Theta_y$, and $\cos\Theta_z$ in the center of mass frame of the decaying hyperon. Shown distributions correspond to Σ^+ hyperons with momentum 500 GeV/c produced on Cu target. Plots (A), (C) and (E) show the asymmetries calculated using method of arithmetic mean. Plots (B), (D) and (F) show the corresponding asymmetries calculated using method of geometric mean.

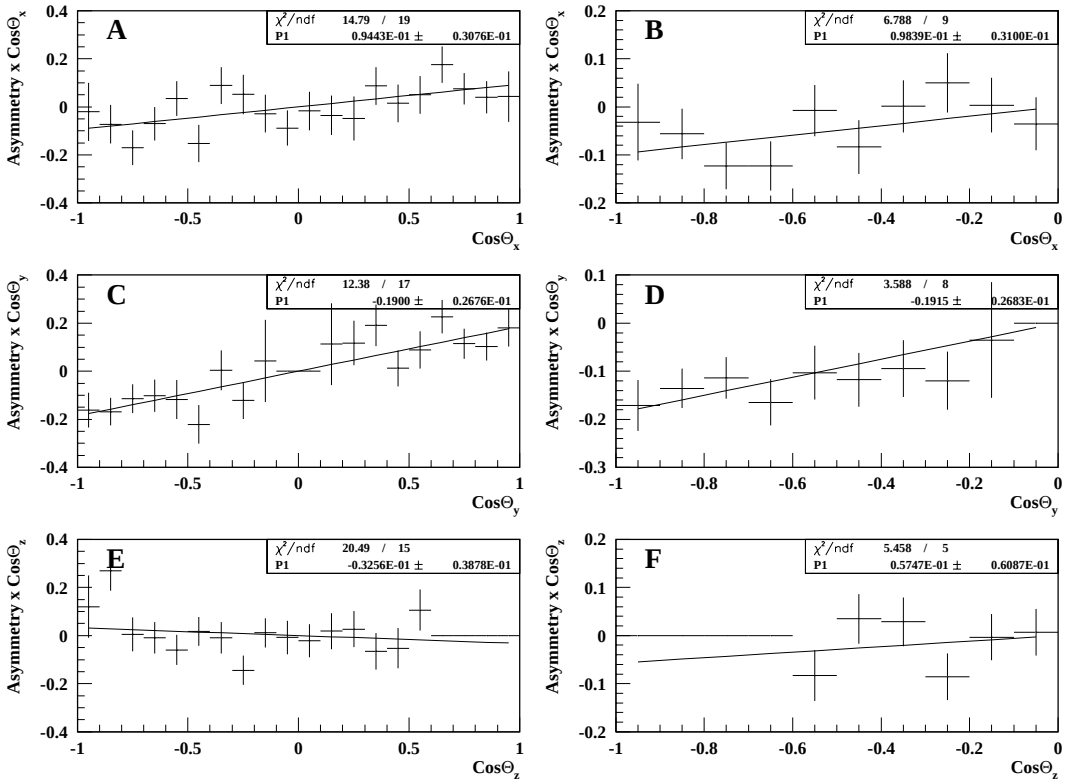

Figure 58: Asymmetries with respect to the cosines of the Σ^+ decay angles (proton angle) $\cos\Theta_x$, $\cos\Theta_y$, and $\cos\Theta_z$ in the center of mass frame of the decaying hyperon. Shown distributions correspond to Σ^+ hyperons with momentum 375 GeV/c produced on Be target. Plots (A), (C) and (E) show the asymmetries calculated using method of arithmetic mean. Plots (B), (D) and (F) show the corresponding asymmetries calculated using method of geometric mean.

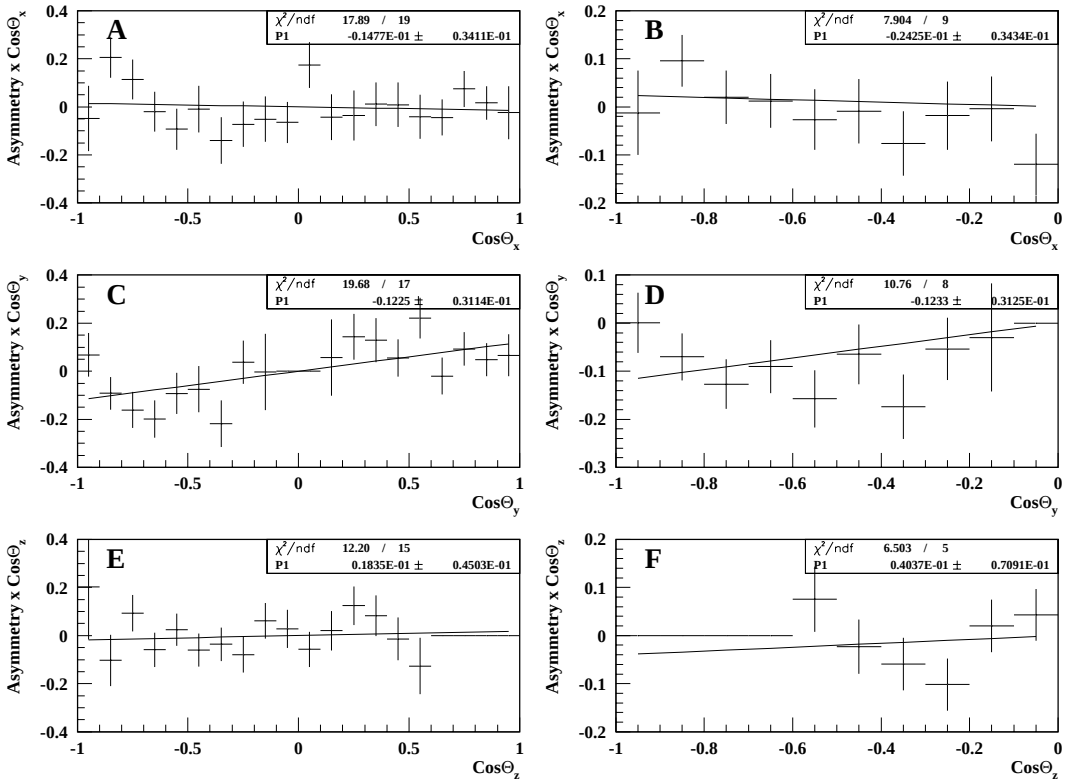

Figure 59: Asymmetries with respect to the cosines of the Σ^+ decay angles (proton angle) $\cos\Theta_x$, $\cos\Theta_y$, and $\cos\Theta_z$ in the center of mass frame of the decaying hyperon. Shown distributions correspond to Σ^+ hyperons with momentum 375 GeV/c produced on Cu target. Plots (A), (C) and (E) show the asymmetries calculated using method of arithmetic mean. Plots (B), (D) and (F) show the corresponding asymmetries calculated using method of geometric mean.

CHAPTER *

References

[1] A. Morelos *et al.*, Phys. Rev. Lett. **71**, 2172 (1993).

[2] A. Morelos *et al.*, Phys. Rev. D **52**, 3777 (1995).

[3] K. Heller *et al.*, Phys. Rev. Lett. **51**, 2025 (1983).

[4] L. Pondrom, Phys. Rep. **122**, 57 (1985).

[5] W.G.D.Dharmaratna, et al. *Gluon fusion as a source for massive-quark polarization*, Phys. Rev. D **41**, 1731 (1990).

[6] A. Andersson, et al. , Phys. Lett. **85B**, 417 (1979).

[7] T.A. De Grand, et al. , Phys. Rev. D **24**, 2419 (1981).

[8] W.G.D.Dharmaratna, et al. *Single quark polarization in quantum chromodynamics subprocesses*, Phys. Rev. D **53**, 1073 (1996).

[9] S.M. Troshin, et al. *Hyperon polarization in the constituent quark model*, Phys. Rev. D **55**, 1265 (1997).

[10] Y. Yamamoto, et al. *Quark Recombination Model for Spin Polarization in High Energy Inclusive Hadron Reactions*, Prog. Theor. Phys. **98**, 95 (1997).

[11] J. Russ, et al. *Proposal to construct Segmented Large Barion Spectrometer*, unpublished.

[12] D. Mao, *Fastbus ADCs and TDCs*, HNOTE **777** (1996).

[13] J. Lach, *E781 Hyperon Spectrometer Constants*, HNOTE **808** (1999).

[14] M. Clemen, D. Potter, *ZIPTRACK magnet mapping of E781 Magnets AN1, AN2 AND AN3*, HNOTE **590** (1992).

[15] P. Cooper, *SELEX TRACKING*, unpublished.

[16] J. Lach, *Hyperons: Insights into the Barion Structure.*

[17] A. Morelos, *Measurement of the polarization and magnetic moment of* Σ^+ *and* $\overline{\Sigma}^-$ *hyperons*, PhD thesis.

[18] G. Bunce, et al. Λ^0 *Hyperon Polarization in Inclusive Production by 300-GeV/c Protons on Beryllium*, Phys. Rev. Lett. **36**, 2172 (1976).

[19] Particle Data Group, C. Caso *et al.*, Eur. Phys. J. C **3**, 1 (1998).

[20] S. Timm *et al.*, Phys. Rev. D **51**, 4650 (1995).

[21] J. Langland, Hyperon Beam Flux Parametrization for E781, Based on E497 Data, HNOTE **693** (June 1994).

[22] C. Wilkinson *et al.*, Phys. Rev. Lett. **46** 803 (1985).

[23] L. Deck *et al.*, Phys. Rev. D **28** 1 (1983).

[24] R. Rameika, Ph.D. Thesis, Rutgers University, 1981 (unpublished).